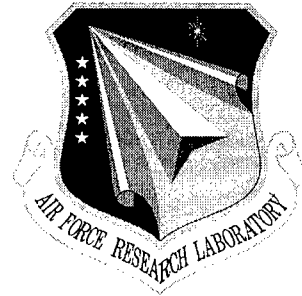


AFRL-IF-RS-TR-2000-13
Final Technical Report
February 2000



AN INTEGRATED CAD TOOL FOR THERMO- FLUIDIC-MECHANICAL-ELECTROSTATIC DESIGN OF MEMS DEVICES

CFD Research Corporation

Sponsored by
Defense Advanced Research Projects Agency
DARPA Order No. E117

APPROVED FOR PUBLIC RELEASE; DISTRIBUTION UNLIMITED.

The views and conclusions contained in this document are those of the authors and should not be interpreted as necessarily representing the official policies, either expressed or implied, of the Defense Advanced Research Projects Agency or the U.S. Government.

AIR FORCE RESEARCH LABORATORY
DTIC QUALITY INSPECTED 3 **INFORMATION DIRECTORATE**
ROME RESEARCH SITE
ROME, NEW YORK

20000328 011

This report has been reviewed by the Air Force Research Laboratory, Information Directorate, Public Affairs Office (IFOIPA) and is releasable to the National Technical Information Service (NTIS). At NTIS it will be releasable to the general public, including foreign nations.

AFRL-IF-RS-TR-2000-13 has been reviewed and is approved for publication.

APPROVED:



CLARE THIEM
Project Engineer

FOR THE DIRECTOR:



NORTHROP FOWLER
Technical Advisor
Information Technology Division

If your address has changed or if you wish to be removed from the Air Force Research Laboratory Rome Research Site mailing list, or if the addressee is no longer employed by your organization, please notify AFRL/IFTC, 26 Electronic Pky, Rome, NY 13441-4514. This will assist us in maintaining a current mailing list.

Do not return copies of this report unless contractual obligations or notices on a specific document require that it be returned.

AN INTEGRATED CAD TOOL FOR THERMO-FLUIDIC-MECHANICAL-
ELECTROSTATIC DESIGN OF MEMS DEVICES

Phillip Stout, Paul Dionne, Andy Leonard, Zhiqiang Tan, Anantha Krishnan, and
Andrzej Przekwas

Contractor: CFD Research Corporation
Contract Number: F30602-97-2-0196
Effective Date of Contract: 01 April 1997
Contract Expiration Date: 30 June 1999
Short Title of Work: An Integrated CAD Tool for Thermo-
Fluidic-Mechanical-Electrostatic
Design of MEMS Devices
Period of Work Covered: Apr 97 – Jun 99

Principal Investigator: Phillip Stout
Phone: (256) 726-4800
AFRL Project Engineer: Clare Thiem
Phone: (315) 330-4893

APPROVED FOR PUBLIC RELEASE; DISTRIBUTION UNLIMITED.

This research was supported by the Defense Advanced Research
Projects Agency of the Department of Defense and was monitored
by Clare Thiem, AFRL/IFTC, 26 Electronic Pky, Rome, NY.

REPORT DOCUMENTATION PAGE			Form Approved OMB No. 0704-0188	
Public reporting burden for this collection of information is estimated to average 1 hour per response, including the time for reviewing instructions, searching existing data sources, gathering and maintaining the data needed, and completing and reviewing the collection of information. Send comments regarding this burden estimate or any other aspect of this collection of information, including suggestions for reducing this burden, to Washington Headquarters Services, Directorate for Information Operations and Reports, 1215 Jefferson Davis Highway, Suite 1204, Arlington, VA 22202-4302, and to the Office of Management and Budget, Paperwork Reduction Project (0704-0188), Washington, DC 20503.				
1. AGENCY USE ONLY (Leave blank)		2. REPORT DATE FEBRUARY 2000		3. REPORT TYPE AND DATES COVERED Final Apr 97 - Jun 99
4. TITLE AND SUBTITLE AN INTEGRATED CAD TOOL FOR THERMO-FLUIDIC-MECHANICAL-ELECTROSTATIC DESIGN OF MEMS DEVICES			5. FUNDING NUMBERS C - F30602-97-2-0196 PE - 63739E PR - E117 TA - 00 WU - 18	
6. AUTHOR(S) Phillip Stout, Paul Dionne, Andy Leonard, Zhiqiang Tan, Anantha Krishnan, and Andrzej Przekwas				
7. PERFORMING ORGANIZATION NAME(S) AND ADDRESS(ES) CFD Research Corporation 215 Wynn Dr., 5th Floor Huntsville AL 35805			8. PERFORMING ORGANIZATION REPORT NUMBER 4894/9	
9. SPONSORING/MONITORING AGENCY NAME(S) AND ADDRESS(ES) Defense Advanced Research Projects Agency Air Force Research Laboratory/IFTC 3701 N Fairfax Drive 26 Electronic Pky Arlington VA 22203 Rome NY 13441-4514			10. SPONSORING/MONITORING AGENCY REPORT NUMBER AFRL-IF-RS-TR-2000-13	
11. SUPPLEMENTARY NOTES Air Force Research Laboratory Project Engineer: Clare Thiem/IFTC/(315) 330-4893				
12a. DISTRIBUTION AVAILABILITY STATEMENT APPROVED FOR PUBLIC RELEASE; DISTRIBUTION UNLIMITED.			12b. DISTRIBUTION CODE	
13. ABSTRACT (Maximum 200 words) The objective of this effort was to develop advanced, multi-disciplinary Computer-Aided Design (CAD) tools to prototype design Micro-Electro-Mechanical Systems (MEMS). The approach was to develop/validate electrostatics model (based on Finite Volume Method/Boundary Element Method), implement electrostatic model in thermo-fluidic-mechanical software, develop communication protocol between model and microtomography imaging data, and apply it to industrial MEMS. Thus, the work described in this report focuses on the development of a CAD tool, CFD-ACE +MEMS, for simulating microsystem operation. CFD-ACE+MEMS is based on a flow, thermal, mechanical CAD tool, CFD-ACE+ which has been modified to include electric and magnetic physical models. CFD Research Corporation used the results of this effort to perform modeling studies of industrial microdevices for MEMS companies using the CFD-ACE+MEMS coupled simulation capability. In addition to demonstrating the CAD tools simulation capability on several tests cases, validation was also pursued using experimentally measured flow fields and displacements obtained through a subcontract with Sarnoff Corporation. The results of this effort have been incorporated into CFD Research Corporation's commercial software and is being used by companies working with MEMS and microelectronics.				
14. SUBJECT TERMS Micro-Electro-Mechanical Systems (MEMS), Microsystem, Finite Element Method (FEM), Finite Volume Method (FVM), Boundary Element Method (BEM), Microtomography, Computer-Aided Design (CAD)			15. NUMBER OF PAGES 162	
			16. PRICE CODE	
17. SECURITY CLASSIFICATION OF REPORT UNCLASSIFIED	18. SECURITY CLASSIFICATION OF THIS PAGE UNCLASSIFIED	19. SECURITY CLASSIFICATION OF ABSTRACT UNCLASSIFIED	20. LIMITATION OF ABSTRACT UL	

TABLE OF CONTENTS

	<u>Page</u>
1. INTRODUCTION	1
1.1 Microsystems or MEMS (Micro-Electro-Mechanical Systems)	1
1.2 Importance of a MEMS CAD Tool	2
1.3 Focus of Proposed Work	3
1.4 Project Tasks and Accomplishments	4
1.5 Outline of the Report	6
2. DESCRIPTION OF PHYSICAL MODELS	7
2.1 Electric Model	7
2.1.1 Capacitance	8
2.1.2 Electrostatic Pressure Force (Electric/Structural)	8
2.1.3 Virtual Force (Electric/Volume of Fluids)	9
2.1.4 Electric Current Density (Electric/Magnetic, Electric/Heat)	10
2.1.5 Boundary Element Method (BEM) and Finite Volume Method (FVM)	10
2.2 Magnetic Model	10
2.2.1 Magnetic Force on Current Carrying Wire (Magnetic/Structure)	11
2.2.2 Force on a High Permeability Material (Magnetic/Structure)	11
2.2.3 Force on a Conductive Flow (Magnetic/Flow)	12
2.2.4 Joule Heating by Induction (Magnetic/Heat)	12
2.3 Flow Model	13
2.4 Heat Model	14
2.5 Mechanical Model	14
2.5.1 Strain-Displacement Relations	14
2.5.2 Stress-Strain Relations	15
2.5.3 Governing Equation of Mechanics	17
2.5.4 Multidisciplinary Coupling	18
3. BOUNDARY ELEMENT AND FINITE VOLUME METHODS	20
3.1 Boundary Element Method (BEM)	20
3.1.1 Overview	21
3.1.2 Space Charge Approximation	21
3.1.3 Kernel Expansion and Fast Integration	22
3.1.4 FastBEM Implementation	23
3.1.5 FastBEM Grid Adaptation	24
3.2 Finite Volume Method (FVM)	24
3.3 BEM vs. FVM	24
4. INTEGRATION OF PHYSICAL MODELS INTO COMMERCIAL CAD TOOL	25
4.1 CFD-ACE+MEMS CAD System	25
4.2 Electric Model in CFD-ACE+MEMS CAD System	26
4.2.1 Electrostatic Boundary Conditions	27

TABLE OF CONTENTS

	<u>Page</u>
4.2.2 Electrostatic Volume Conditions	29
4.2.3 FVM Control Parameters	30
4.2.4 BEM Control Parameters	32
4.2.5 Electric Model DTF Output	34
4.3 Prototype for Web Based Interface	35
 5. VALIDATION STUDIES AND STUDIES OF INDUSTRIAL MICROSYSTEMS	 40
5.1 Benchmarks of BEM	40
5.2 Benchmarks of FVM and BEM Applied to Electrostatics	42
5.2.1 Parallel Plates	43
5.2.2 Concentric Spheres	44
5.2.3 Sphere of Space Charge	45
5.3 Electrostatic Loading of Mechanical Structures	46
5.3.1 Doubly Clamped Beam	46
5.3.2 Accelerometer	47
5.3.3 High Frequency Resonator	48
5.3.4 Electrostatic Torsional Micromirror	48
5.3.5 Micromotor Torque Curve Extraction	49
5.3.6 Linear Lateral Resonator Comb Drive	50
5.4 Fluid Damped Beam Under an Electrostatic Load	52
5.5 Electrostatic/VOF Test: Electrostatic Extraction of Conductive Fluid from Bath	54
5.6 Magnetic Test Cases	56
5.6.1 Magnetic Field Due to a Circular Current Carrying Wire	56
5.6.2 Magnetic Field Due to Current Carrying Bus Bar at a High/Low Permeability Interface	57
5.7 Magnetic Field Using a Source Calculated from Electric Model	58
5.7.1 Magnetic Field for Spiral Conductor	58
5.7.2 Magnetic Field Due to Planar Coil	59
5.8 Magnetic Actuation of a Beam	60
5.9 Buoyancy-Driven Flow of a Conductive Fluid	61
5.10 Electroosmosis	61
 6. ANALYSIS ON INDUSTRIAL DEVICES	 63
6.1 Xerox Flap Valve	63
6.2 Honeywell Mesopump	63
6.3 Honeywell Cantilever Beam	65
 7. IMPLICIT COUPLING VIA MULTI-NEWTON METHOD	 68
7.1 Multi-Newton Method	68
7.2 Demonstration of Multi-Newton Method on Electric/Structural Problems	70

TABLE OF CONTENTS

	<u>Page</u>
8. IMAGING, VISUALIZATION AND VALIDATION OF MICROSYSTEMS	71
8.1 Imaging and Visualization	71
8.2 Three-dimensional Geometry Extraction	72
8.3 Two-dimensional Flow Field Extraction	77
8.4 Comparison of Measured and Calculated Flow Data	77
8.5 Comparison of Measured and Calculated Electrostatic Deformation	83
9. CONCLUSIONS AND PLANS FOR FUTURE WORK	88
9.1 Summary of Accomplishments	88
9.2 Industrial Collaborations and Software License	88
9.3 Future Work	89
10. REFERENCES	90

LIST OF FIGURES

<u>Figure</u>	<u>Page</u>
3-1 Grid Adaptation in FastBEM	24
4-1 The CFD-ACE+MEMS CAD System	25
4-2 Dialog Where Electric Model is Chosen and Either FVM or BEM Solver is Selected	27
4-3 Electrostatic Boundary Conditions Window at Model. "Bond.Cond.". "Surface BC". Values	28
4-4 Electrostatic Volume Conditions Window at Model.Prop.Solid.Electrostatics or Model.Prop.Gas.Electrostatics	29
4-5 An Overview of the FVM Controls	31
4-6 BEM Control Parameters Window at Solve.Control.Electrostatics	32
4-7 Snapshot of Upper Portion of GUI for CFD-FastBEM	36
4-8 Snapshot of Lower Portion of GUI for CFD-FastBEM	37
4-9 Results from On-line Execution of FastBEM	38
4-10 Visualization of FastBEM Results Using VRML	39
5-1 Temperature Distribution on a Sphere Subjected to Surface Irradiation and Convection	40
5-2 Displacement of a Cylinder Under Surface Pressure	41
5-3 Test Cases Used by TEAM	42
5-4 Parallel Plate Geometry	43
5-5 Concentric Sphere Geometry	44
5-6 Sphere of Space Charge of Radius R in an Optional Box with Aides of Length $a > R$	46
5-7 Doubly Clamped Beam Under an Electrostatic Load, with an Applied Voltage $\phi_0 = 10$ or 20 V	47
5-8 Accelerometer Under an Electrostatic Load	47
5-9 Displacement Field Contours on a High Frequency Resonator	48
5-10 Computational Results for an Electrostatic Micromirror	49
5-11 Geometry and Computational Grid for an Electric Micromotor	50
5-12 Computed Torque-Angle Relationship for the Micromotor	50
5-13 Linear Lateral Resonator Comb Drive with an Applied Sinusoidal Drive Voltage at Two Instances in Time	52
5-14 Doubly Clamped Fluid Damped Beam Under a Sinusoidal Electrostatic Load	53
5-15 Displacement and Voltage Plots for a Doubly Clamped Fluid Damped Beam Under a Sinusoidal Electrostatic Load	54
5-16 Time Evolution of the Electrostatic Extraction of a Conductive Fluid from a Bath	55
5-17 Magnetic Field Vectors Around Wire with Uniform Current	56
5-18 Comparison of Calculated (Red) and Analytical (Black) Solutions of Magnetic Field Due to an Infinitely Long Current Carrying Wire	56
5-19 Bus Bar Test Case Specification	57
5-20 Calculated Vector Magnetic Potential Around a Bus Bar Between Materials of Different Permeability	58
5-21 Magnetic Field Due to Current in Circular Coil	59
5-22 Problem of Plate Movement Due to a Magnetic Field	60

LIST OF FIGURES (CON'T)

<u>Figure</u>	<u>Page</u>
5-23 Displacement Field Contours, Magnetic Field Lines, and Force Vectors on a Magnetically Actuated Beam	60
5-24 (a) Temperature and (b) Vertical Velocity Contours for Coupled Flow/Magnetics Solution	61
5-25 Electric Potential in Flow Velocities for a Cross Channel Device	62
6-1 Flow Across a Flap with Different Applied Voltages	63
6-2 Solids Model of a Mesopump Cell with Boundary and Physical Conditions	64
6-3 Comparison of Calculated and Measured Actuation Times of Pump for Different Driving Voltages	64
6-4 Electrostatic Field Distribution in Pump	65
6-5 Schematic of Electrostatic Actuator	66
6-6 Computational Results for $h = 20\mu$ and $h = 60\mu$	66
6-7 Pressure vs. Height Curves for 0 and 80 Volts	67
8-1 Extracted Geometry Algorithm: Isosurfacing via Marching Cubes	73
8-2 Comparison of Old and New Marching Cubes Algorithm on the Redwood Systems Normally Open Microvalve	73
8-3 Extracted Geometry Using an Active Contours Algorithm	74
8-4 Extracted Geometry Using an Object Segmentation Algorithm	75
8-5 Comparison of the Geometry Extracted from the Synthetic Tomography (Blue) versus the Original CAD Model (Yellow)	76
8-6 Schematics of the Flow Channels Received from Sarnoff	78
8-7 Visualization of the STL Files of the Flow Channels Received from Sarnoff	79
8-8 Computational Grids for the Channel Geometries	80
8-9 Numerical and Experimental Velocity Fields for Channel 12	81
8-10 Numerical and Experimental Velocity Fields for Channel 14	81
8-11 Numerical and Experimental Velocity Fields for Channel 21	81
8-12 Predicted Velocity Field for Channel 26	82
8-13 CFD-CARTESIAN Calculated Conversion of STL Format Files into Computational Grids for Channel 12 and 14	82
8-14 Resulting CFD Calculation on Channel 14 Using the Computational Grid Generated by CFD-CARTESIAN from the STL Formatted File	83
8-15 Representative Visualization Images of Two Electrostatically Actuated Comb Drives	84
8-16 Visualization of CIF File specifying MUMPS (Multi-User MEMS Processes) Manufacturing Process for Construction of Angular Resonator	85
8-17 Angular Resonator Grid Used for Simulation	85
8-18 Calculated Deformation of the Angular Resonator at Two Different Times	86

LIST OF TABLES

<u>Table</u>	<u>Page</u>
5-1 Benchmark Results for Heat Conduction Inside a Sphere	41
5-2 Benchmark Results for Deformation of a Cylinder Under Surface Pressure	41
5-3 Benchmark Comparisons with TEAM	42
7-1 Comparison of Sequential Relaxation and Multi-Newton Coupling Algorithms	70

EXECUTIVE SUMMARY

Microsystems or micro-electro-mechanical systems (MEMS) are an emerging technology having potential applications in military, environmental, medical and industrial applications. Though the concept of MEMS has been known for more than 20 years, the commercialization of MEMS technology has not progressed as fast as IC chip technology. The lack of understanding of physical phenomena and their interactions in microsystems has been a major technical barrier in the use of MEMS devices. Most microdevices rely on thermal, mechanical, fluid, electric, and magnetic interactions for performing the intended function. Recent advances have been made in understanding each of these effects individually. However, for most devices, the coupled effects of these phenomena are not well understood.

Although the viability of MEMS devices for various applications has been demonstrated in research laboratories, many of these devices have yet to become commercial products. The current procedure of trial-and-error testing and fabrication of devices makes them very expensive to design. In many instances the performance and reliability are far from optimal. The availability of advanced CAD tools which could aid microsystem designers and manufacturers in analyzing/designing microsystems would result in a significant reduction in the extent of physical testing that needs to be done in order to prototype a device. Advanced CAD tools are a key to higher performance/reliability, reduced costs, shorter prototyping cycles and improved time-to-market.

The study described in this report focuses on the development of a CAD tool, CFD-ACE+MEMS, for simulating microsystem operation. CFD-ACE+MEMS has models to simulate coupled effects of flow, thermal, mechanical, electric, and magnetic phenomena. The models are accessible through geometry, visualization, and problem set-up software. The simulation abilities of the CAD tool have been demonstrated on many well-characterized microsystems and test cases. Also, through experimental measurements conducted at Sarnoff Corporation (under a sub-contract), the CAD tool has been verified using measured flow field and mechanical displacements.

CFD-ACE+MEMS is based on a flow, thermal, mechanical CAD tool, CFD-ACE+ which has been modified to include electric and magnetic physical models. The structural mechanics model is now supplied with additional forces such as the electrostatic pressure forces, magnetic moment forces, and the Lorentz force on a conducting body. The heat model now has additional heat sources due to joule heating both from conduction currents in resistive materials and inductive heating due to time varying magnetic/ electric fields. The flow module has an additional Lorentz force on flows of (electrically) conducting fluids. The volume of fluids (VOF) model is supplied with an electrostatic force that opposes the surface tension on the free surface. The electric model also calculates source currents for use by the magnetic model.

The electric model solves Poisson's equation or a conduction equation for the electric potential. From the electric potential the electric field, capacitance, electrostatic pressure forces, and the conduction currents are calculated. There are two computational methods available for solving the electric equations. One is the finite volume method (FVM) and the other is the boundary element method (BEM). The FVM uses finite difference and the Divergence Theorem to

discretize the solution space. The resulting difference equation is solved using a linear solver such as an iterative conjugate gradient solver (CGS). The BEM solves the integral form of the electric equations at boundary surfaces. The boundary surface integrals are approximated using techniques similar to the multipole method. The solution to the resulting linear set of equations is obtained using a solver based on the generalized minimal residual (GMRES) method.

The FVM requires a volume mesh and calculates the electric potential (and the electric field) at every cell (volume) in the mesh. The BEM requires only a surface mesh (although volume information is required in defining the different "domains") and calculates the electric potential (and the electric field) only at boundary and interface faces. The BEM is very naturally applied to unbounded problems unlike the FVM method. The BEM method has higher computational cost (speed, memory) per boundary element than FVM does per volume element. This does not mean BEM is slower since many problems require much fewer BEM face elements than FVM volume elements, where the BEM is faster than the FVM.

The magnetic model solves a vector laplacian equation for the magnetic vector potential either in time or assuming sinusoidal steady state (frequency domain). From the magnetic vector potential, the magnetic field, electric field, Lorentz force, torques on magnetic moments, and eddy currents are calculated. The magnetic model equations are solved using only the FVM.

All of the physical models (fluid, heat, structural, electric, magnetic) are coupled either (i) loosely, or (ii) implicitly. The loose coupling is through boundary and volume conditions being passed between models during sequential execution. Each physical model is solved separately from the others using only boundary conditions and volume conditions the other models calculated during their previous solution. When passing the information between models, linear relaxation may be applied to the relevant parameters to improve convergence. While this linking is efficient for many systems, it will fail when the coupling becomes too stiff. This occurs quite often in solid/fluid systems with small clearances, i.e., elastohydrodynamics. Coupled electric/structural systems with small clearances will also exhibit tight coupling. In these instances, a certain degree of implicit coupling between the models is necessary to obtain a stable, converged solution.

One advanced implicit coupling methodology the "multi-level Newton method" being developed by Jacob White's research group at MIT (Aluru and White, 1997) has been implemented to ensure stable and robust convergence. The method is general enough so that it is applicable to any physical model (structures, fluids, heat, electromagnetics) and any solution method (FVM, BEM, FEM). The technique is a black box approach in that the models to be linked need only have a clear set of input and output values upon which they mutually depend. No complicated links need to be established between the models. The multi-level Newton method implementation in CFD-ACE+MEMS has been demonstrated for an electric/structural coupled problem.

Fundamental validation of the models was carried out by comparing the CAD tool calculations with analytical solutions for simple benchmark cases and published data of operating microsystems in the literature. Also, a series of parametric studies have been performed to evaluate the model characteristics (numerical stability and physical accuracy) over a range of

conditions. The types of studies carried out using the developed CAD tool were diverse. Some of these are listed below:

- ❑ The BEM was tested for heat conduction inside a sphere, cylindrical vessel deformation under surface pressure, and compared against NASTRAN's boundary element method package.
- ❑ Parallel plates, concentric spheres, and sphere of space charge benchmarks were used to compare FVM and BEM performance.
- ❑ Electrostatic loading of mechanical structures was modeled for microsystems such as a doubly clamped beam, an accelerometer, a high frequency resonator, an electrostatic torsional micromirror, a micromotor, a linear lateral resonator comb drive, an angular resonator comb drive, and a fluid damped beam.
- ❑ Electrostatic extraction of a conductive fluid from bath was calculated.
- ❑ The magnetic field due to a circular current carrying wire was modeled. Shielding of magnetic field generated from a bus bar due to a high permeability material was modeled. The magnetic field due to circular and square planar coils was calculated using source currents from the electric model. The magnetic actuation of a beam with an attached piece of high permeability material was calculated. The effect of a magnetic field on the damping of a buoyancy-driven flow of a conductive fluid was analyzed.

A communication protocol to use microtomography experimental data was developed. This protocol developed in collaboration with Sarnoff Corporation facilitates the transfer/conversion of data files containing geometry and flow field information. The imaged geometry information can now be directly accessed by CFD Research Corporation's (CFDRC's) models for performing the simulations. The protocol also facilitates the transfer of information on velocity fields which were used in a validation study. The significant outcomes of Sarnoff's efforts include: (i) a progressively refined methodology for accurate extraction of device structure from microtomography data; and (ii) a tool to perform good quality surface triangulation of the device.

A validation study was carried out using flow data, mechanical motion, and geometry drawings supplied by Sarnoff Corporation. The measured flow fields for three flow channels were used to verify CFD-ACE calculation of the flow fields. Also, previously imaged mechanical motion of moving parts in a comb drive in conjunction with a "CIF" file was used to verify the electric/mechanical model.

This project has also enabled CFDRC to perform several recent modeling studies (of industrial microdevices) for MEMS companies using the coupled simulation capability. These are summarized below:

- ❑ **Micropump for Honeywell:** CFDRC performed 3-D simulations of coupled fluid-structural-electrostatic phenomena in a micropump currently being prototyped by Honeywell. These simulations were successful in highlighting some of the complexities of the interaction between the above phenomena and enabled Honeywell designers to improve the performance of the micropump.

- **Electrostatically Activated Beam for Honeywell:** Simulations were performed for Honeywell to analyze the deflection of a cantilever beam for different actuation voltages. Non-linear effects were also simulated. Mechanical forces (as a function of gap height) for different voltages were computed.
- **Microvalve for Xerox:** CFDRC performed simulations of coupled fluid-structural-electrostatic interactions in Xerox's microvalve. The simulations clearly showed the highly non-linear nature of the valve operation and also gave insights as to the extent of voltage drop necessary for optimal performance of the valve.
- **Electrophoresis Applications:** CFDRC is currently working with Oak Ridge National Lab., Caliper Technologies, Aclara Biosciences, etc. to demonstrate CFDRC's electrophoresis model that accounts for interactions between charged species transport and the applied electrostatic field.

CFDRC software is also in use by many MEMS groups such as Redwood Microsystems, Lucas Nova Sensor, Motorola, Honeywell, Mesoscale Systems, YSI, Stanford University, University of California (Berkeley), University of Washington, Oak Ridge National Laboratory, etc.

The thermo-fluidic-mechanical-electromagnetic model developed and validated in this project has been incorporated into a software environment (consisting of geometry modelers, grid generators, advanced visualization software, Graphical User Interfaces, etc.) and is being commercialized as a design tool. In addition to MEMS companies, several microelectronics companies such as Wacker-Siltronic, Aixtron, Motorola, Applied Materials and Novellus have purchased software licenses from CFDRC for the coupled fluid-thermal-structural-electric-magnetic software. Their applications include electromagnetic induction heating, Lorentz force stabilization of melt flow in crystal growth, low-pressure plasma transport and electroplating. CFDRC expects a large market for this coupled simulation capability. CFDRC's software is one-of-a-kind in its ability to closely integrate these models.

ACKNOWLEDGEMENTS

This project was funded by DARPA/MTO and monitored by Air Force Research Laboratory/IFTE. The authors would like to thank DARPA program managers Dr. Randy Harr, Dr. Heather Dussault and Dr. Noel MacDonald for their enthusiastic support of this work. The authors are also extremely thankful to Mr. Clare Thiem of AFRL/IFTC for his feedback/review of project progress and useful suggestions/recommendations.

Dr. N. Vaidya of CFDRC played a key role in implementing the electromagnetic models in CFD-ACE+MEMS. Dr. H. Q. Yang and Dr. Mahesh Athavale provided valuable feedback on the performance of the models and assisted in model verification. Mr. Milind Talpallikar, Director/Software at CFDRC, worked tirelessly to integrate the models into the commercial software. Dr. Winston Jiang and Mr. Lyle Johnson provided considerable help in the implementation of Graphical User Interfaces (GUIs) for the new capabilities.

The efforts of Mr. Mike Amabile and Dr. Ann-Marie Lanzillotto (from Sarnoff Corporation) were invaluable in the successful development of the communication protocol between microtomography measurements and the multi-disciplinary simulation tool, CFD-ACE+MEMS.

And last, but not least, the authors would like to thank Mrs. Stephanie Cameron for her painstaking preparation of all progress reports as well as this final report.

1. INTRODUCTION

This is the final report documenting the work performed during a two year DARPA/AFRL Project (Contract # F30602-97-2-0196) entitled "An Integrated CAD Tool for Thermo-Fluidic-Mechanical-Electrostatic Design of MEMS Devices". The overall objective is to develop a state-of-the-art integrated Computer-Aided-Design (CAD) tool for the analysis and design of MicroElectroMechanical Systems (MEMS). Coupled flow, thermal, mechanical, electric, and magnetic models have been developed. The coupled models have been integrated with geometric and visualization tools, design database tools, and a graphical user interface (GUI) for ease-of-use of the software which is being supplied to MEMS vendors. The CAD tool development has been completed and modeling studies have been performed on benchmark cases for testing and validation as well as on commercial MEMS devices. The advanced 3-D imaging and visualization capabilities of Sarnoff Corporation were used to validate the software. The CAD package has been evaluated on a range of microdevices for use as a design and prototyping tool. The CAD tool is currently being commercialized to MEMS manufacturers and vendors and research groups in national laboratories and academia.

1.1 Microsystems or MEMS (Micro-Electro-Mechanical Systems)

MEMS is an emerging technology having potential applications in military, environmental, medical and industrial applications. Recent advances in the development of micromachined components such as sensors, flow channels, valves and diaphragm pumps have created opportunities for application of MEMS technology in diverse areas. Using a combination of these components, applications in drug delivery systems, chemical process control, environmental detection and industrial feed-back control systems are becoming possible. Though the concept of MEMS has been known for more than 20 years, the commercialization of MEMS technology has not progressed as fast as IC chip technology. The lack of understanding of physical phenomena and their interactions in microsystems has been a major technical barrier in the use of MEMS devices. For example, a thorough understanding of fluid dynamical behavior and static and dynamic interaction of various components in complex systems is lacking. Though there are similarities between MEMS components and their macroscopic counterparts, there are several peculiarities that need to be identified and understood. For example, in recent experiments, it has been observed that the viscosity of liquid in micro-channels is a function of channel size. Also, increased flow rates and decreased pressure drops have been reported which are attributed to "slip walls" at low Knudsen number flows. Most microdevices rely on thermal, mechanical, electrostatic and fluidic interactions for performing the intended function. Recent advances have been made in understanding each of these effects individually. However, for most devices, the coupled effects of these phenomena are not well understood.

Although the viability of MEMS devices for various applications has been demonstrated in research laboratories, many of these devices have yet to become commercial products. In order for MEMS devices to be mass-produced commercially, the technology has to progress to a stage where the following criteria are satisfied:

1. The device should be efficient, i.e., it should consume minimum power to perform the desired operation.

2. The device should have good performance characteristics over a range of operating conditions.
3. The reliability of the device, i.e., it has to perform the desired operation without the occurrence of mechanical/structural failure over the designed lifetime of the device.
4. The device design should be reasonably simple to facilitate mass production. This will lower the costs of incorporating MEMS technology to various systems and thus widen the range of its applicability.

The current procedure of trial-and-error testing and fabrication of devices makes them very expensive. In many instances the performance and reliability are far from optimal. The use of advanced CAD tools will result in significant reduction in the extent (and hence the cost) of physical testing that needs to be done in order to prototype a device. Advanced CAD tools will be the key to higher performance/reliability, reduced costs, shorter prototyping cycles and improved time-to-market.

1.2 Importance of a MEMS CAD Tool

Although the viability of MEMS devices for various applications has been demonstrated in research laboratories, many of these devices have yet to become commercial products. Many design issues relating to device performance/reliability, mass production, packaging, etc., have not yet been addressed satisfactorily for many of the MEMS devices currently being explored in research laboratories. To achieve these objectives, innovative design ideas need to be tested in a short period of time. Physical testing and prototyping of these devices tends to increase the design cycle time and costs associated with transitioning the technology to the commercial sector. In this regard, advanced CAD tools will play a significant role in complementing physical testing and will aid in the experimentation and development of new designs to ensure performance and reliability.

As mentioned before, most microdevices rely on thermal, fluidic, mechanical and electrostatic interactions for performing their intended function. Although advanced models are available to analyze and simulate each of these interactions, no tool is currently available to model the coupled effects of these phenomena. Most existing models are able to assess individual effects of the above phenomena. For example, MEMCAD is able to perform advanced electrostatic analysis of MEMS devices. Codes such as FIDAP and CFD-ACE are able to analyze the fluidic and thermal effects in such systems. Software such as NASTRAN is able to do a thorough structural analysis of the system. ANSYS now has a multi-physics capability. However, a model that is able to analyze the coupled effects of these phenomena (flow, thermal, structural, electric, and magnetic) does not exist.

Many MEMS groups have used modeling studies to support the design of various devices. Some of these studies are summarized below. Zengerle and Richter (1994) and Gravesen (1993) have discussed several aspects of flow simulation in micro-fluidic components. Most of the simulations reported in the literature utilized very simple 0-D or 1-D semi-empirical models. More recent fundamental Navier-Stokes based studies were performed by Vollmer (1994) on

2-D fluidic amplifiers, by Arkilic (1994) (MIT) on 1-D gas flow in channels and by Mehregany (1993) on 2-D flow in micro-motors. A review of the state-of-the-art in computational microfluid dynamics has been performed by Przekwas (1995).

Early model development efforts for MEMS include initiatives such as MEMCAD, at MIT (Senturia et al., 1992), CAEMEMS at the University of Michigan (Zhang et al., 1990), PUSI, MEMS design automation at CalTech. Recent development efforts (under the DARPA sponsored Composite CAD program) include organizations such as CFDRC, Microcosm, Coyote Systems, Tanner Research, Analogy, etc. Most efforts have integrated different analysis tools (from different disciplines) into design environments. Appropriate information on boundary conditions is communicated between the models and the solution is obtained by iterating between the various models. However, depending on the complexity and non-linearity of coupling between the various phenomena, this coupling approach may not result in a converged solution for the overall system. In cases where the coupling is highly non-linear and stiff (of varying time scales), an explicit linking of the models will not yield a stable and converged solution. For example, the deflection of a structure in a MEMS device will depend on the thermal, fluid pressure and electrostatic loads on the structure. However, as the structure begins to deflect, each of the loads will change as a result of the deflection. In order to reach the stable equilibrium position of the structure under the action of all the loads, each of the models have to be coupled in an implicit manner. Otherwise, convergence will not be achieved regardless of the number of iterations used between the models.

Implicit coupling of models implies the solution of one model depends directly on the solution of the other models. That is, the solution is a function of the solution of the other methods at solution points within the discretized computational grid. Some examples of implicit coupling are solving the models simultaneously in one large matrix or in some way having the predictor values a function of the coupled models.

1.3 Focus of Proposed Work

Ongoing modeling activities (such as development of MEMCAD) have sought to integrate specialized software from several disciplines through appropriate exchange of information (on boundary conditions). However, this approach has major technical and commercial drawbacks. MEMS processes are highly non-linear and the semi-explicit coupling between the disciplines will not yield a converged solution. For these systems, it is necessary to solve all of the relevant processes in a highly coupled implicit manner in order to obtain a stable, converged solution. Such a capability is not currently available and is a must for prototyping MEMS devices. Also, the use of a design environment with loosely coupled software is not economically feasible. The user will have to pay the costs associated with license fees for each of the software packages (such as FIDAP, NASTRAN, PATRAN, etc.) and still will not get adequate technical support for the integrated capability.

The goal of the proposed work was to develop a comprehensive multi-disciplinary simulation capability within a single environment. Depending on the problem being solved, this environment will provide options for either loose coupling or tight (implicit) coupling between the different modules. The advantage of this approach is that it enables the developer (i.e.,

CFDRC) to provide the software at low cost to the designer. Additionally, the support of the software will be done by a single entity.

The starting point for this development effort was CFD-ACE+, a commercial multi-disciplinary software developed by CFDRC. CFD-ACE+ has capabilities to simulate coupled effects of fluid flow, heat/mass transfer and chemistry in conjunction with stress analysis and structural deformation. Under this project, physical models for electrostatics, magnetostatics and electromagnetics were developed and coupled into CFD-ACE+. The software has been tested and verified on several MEMS applications involving coupling between the modules. Specific examples include :

- Electrostatic-mechanical coupling in accelerometers, comb drives, etc.
- Electrostatic-mechanical-fluidic coupling in microvalves.
- Electrostatic-fluidic coupling in electrophoresis, electrostatic extraction of droplets from a fluid bath, etc.
- Magnetostatic-fluidic coupling in magnetic stabilization of fluid flow.
- Electrostatic-thermal-fluidic-mechanical interactions in a cantilever beam.
- Magnetic-mechanical interactions in a beam

The completion of this project has resulted in a new software environment, CFD-ACE+MEMS, that is capable of simulating highly complex physical interactions in microsystems. CFD-ACE+MEMS has set the stage for further development in the areas of reduced models and parametric models that will enable complete system analysis. Those efforts are DARPA BAA 97-17: "Generation of Reduced Parametric Models of Microdevices from High Fidelity Tools for System Level Composite CAD" and DARPA BAA 97-39: "Mixed-Dimensionality VLSI-Type Configurable Simulation Tools for Virtual Prototyping of Biomicrofluidic Devices and Integrated Systems."

1.4 Project Tasks and Accomplishments

This section describes the tasks that were proposed under this project along with the corresponding accomplishments for each task. The two phases of work which have been completed in this project include:

PHASE 1: DEVELOPMENT OF A THERMO-FLUIDIC-MECHANICAL-ELECTRO-MAGNETIC MODEL FOR MEMS DEVICE OPERATION

Task 1. Developed and Adapted Electromagnetic Solvers (Electric and Magnetic) for MEMS Applications: There is now electric (FVM and BEM methods) and magnetic solvers (FVM method only) available in the CAD environment (CFD-ACE+MEMS) which are coupled to the flow, heat, and structural physical models. The electromagnetic solvers have been tested and refined to commercial grade.

Task 2. Adapted the Thermo-Fluidic-Mechanical Code to Include the Electromagnetic Models: The existing CAD tool CFD-ACE+ has been modified to interface with the electrostatic and magnetic models. The structural mechanics model is now supplied with additional forces

such as the electrostatic pressure forces, magnetic moment forces, and the Lorentz force on a conducting body. The heat model now has additional heat sources due to joule heating both from conduction currents in resistive materials and inductive heating due to time varying magnetic/electric fields. The flow module has an additional Lorentz force on conductive flows. The volume of fluids (VOF) model is supplied with an electrostatic force which opposes the surface tension on the free surface. The electrostatic model can calculate source currents for use by the magnetic model. The thermo-fluidic-mechanical-electromagnetic model developed and validated in this project has been incorporated into a software environment (consisting of geometry modelers, grid generators, advanced visualization software, Graphical User Interfaces, etc.) and is being commercialized as a design tool.

Task 3. Implemented Implicit Coupling Between the Models: A general implicit coupling scheme, referred to as the multi-level Newton method (Aluru and White, 1997), has been implemented in the CAD tool and demonstrated for mechanical-electrostatic coupling. The method is general enough so that it is applicable to any physical model (structures, fluids, heat, electromagnetics) and any solution method (BEM,FVM,FEM).

Task 4. Developed a Communication Protocol with Microtomography Experiments: This protocol developed in collaboration with Sarnoff Corporation facilitates the transfer/conversion of data files containing geometry information. The imaged geometry information can now be directly accessed by CFDRC models for performing the simulations. The protocol also facilitates the transfer of information on velocity fields which were used in the validation study. The significant outcomes of Sarnoff's efforts are: (i) a progressively refined methodology for accurate extraction of device structure from microtomography data; and (ii) a tool to perform good quality surface triangulation of the device.

Task 5. Carried Out Validation and Parametric Studies: Fundamental validation of the models was carried out comparing the predictions (for simple systems) with published data in the literature. A series of parametric studies has been performed to evaluate the model characteristics (numerical stability and physical accuracy) over a range of conditions.

PHASE 2: APPLICATION/VERIFICATION OF PHYSICAL MODELS ON INDUSTRIAL DEVICES

Task 1. Selected Microsystems to be Modeled: Selected microsystems to be modeled based on the following criteria: (i) the device operation should rely on physical phenomena that can be simulated by the model, (ii) the device should be sufficiently experimentally characterized to enable modeling.

Task 2. Performed Verification Simulations of Selected Microsystems: The microfluidic simulations of Sarnoff devices have been completed. Electrostatic model verification of an angular resonator comb drive has been completed. The parameters that were tested are (i) geometry of the device, (ii) the materials used in the device, (iii) flow conditions, and (iv) magnitude of structural deflection of microsystems.

Task 3. Visualization of Device Performance: The operation of microsystems were imaged and visualized at Sarnoff Corporation. Specifically, the flow channel geometries have been imaged and the velocity fields of flows in these channels have been measured. Previously imaged mechanical motion of moving parts in a comb drive was used to verify the electric/mechanical model.

1.5 Outline of the Report

Chapter 2 describes the fundamental formulation and governing equation for each of the physical models developed and adapted during the course of this project. Chapter 3 describes the application of the finite volume method (FVM) and the boundary element method (BEM) for computing electrostatic fields. The integration of the physical models into a commercial CAD environment, CFD-ACE+MEMS, is described in Chapter 4. Detailed validation and model verification studies are presented in Chapter 5. Chapter 6 describes the application of CFD-ACE+MEMS for simulating coupled multi-disciplinary phenomena in industrial microsystems. The implicit coupling procedure between the individual modules is presented in Chapter 7. Chapter 8 describes the imaging and visualization activity performed at Sarnoff Corporation. Chapter 9 concludes with a summary of work accomplished, commercialization efforts and plans for future development.

2. DESCRIPTION OF PHYSICAL MODELS

This chapter describes the physical models in the CAD tool. First, the electromagnetic models (electric and magnetic models) developed under this project will be described. During the discussion, emphasis will be placed on how the electromagnetic models have been coupled to existing flow, heat, and structural models. The structural mechanics model is now supplied additional forces such as the electrostatic pressure forces, magnetic moment forces, and the Lorentz force on a conducting body. The heat model now has additional heat sources due to joule heating both from conduction currents in resistive materials and inductive heating due to time varying magnetic/electric fields. The flow module has an additional Lorentz force in the momentum equation for conductive flows. The electric model can calculate source currents for use by the magnetic model.

2.1 Electric Model

The electric model involves the solution of the electric potential. The model solves two basic equations, either Poisson's equation (Eq. (2.1)) or a conduction current (Eq. (2.2)) equation.

$$\nabla \cdot \epsilon_r \nabla \phi = -\frac{\tilde{n}}{\epsilon_0} \quad (2.1)$$

$$\nabla \cdot \sigma \nabla \phi = 0 \quad (2.2)$$

where ϕ is the electric potential, ϵ_r is the electric relative permittivity, ϵ_0 is the permittivity of free space, ρ is the space charge, and σ is the electric conductivity. From the electric potential the electric field \mathbf{E} , the pressure force, and the capacitance of the geometry are calculated. If the conduction problem is solved the current density \mathbf{J} , virtual force, and joule heating source are also calculated.

Poisson's equation comes from Gauss' law for the electric field ($\nabla \cdot \mathbf{D} = \rho$), the constitutive relation $\mathbf{D} = \epsilon_0 \epsilon_r \mathbf{E}$, and the definition of the static electric field in terms of the electric potential (i.e., $\mathbf{E} = -\nabla \phi$ since $\nabla \times \mathbf{E} = 0$). The electric field which satisfies Poisson's equation is used to calculate pressure forces and capacitances when an electrostatic assumption is valid (no movement of charge).

The conduction problem is primarily used to calculate source currents for the magnetic model, joule heating sources for the heat module, and pressure forces for the volume of fluids model. The conduction or current continuity equation (Eq. (2.2)) is a reduced form of the continuity equation (Eq. (2.3)). The conduction equation used here assumes movement of charge is occurring at a much faster rate than the time steps taken (no time varying magnetic fields, electric fields, or space charge), and that the movement of charge is due only to conduction current (no convection current). Also, implicit in the conduction equation here is that the electrons have had enough time to move through the material(s) to a relaxed state (i.e., steady state).

$$\nabla \cdot \mathbf{J} = -\frac{\partial \tilde{n}}{\partial t} \quad (2.3)$$

2.1.1 Capacitance

Capacitance is a ratio of separated charge to electric potential. In the electric model a total charge Q_{ϕ_o} is calculated for every set of boundaries with a unique fixed electric potential ϕ_o . To determine the Q at a fixed potential boundary, one starts with the electric field boundary conditions

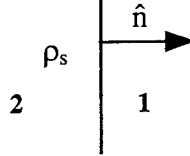


Figure 2-1. Defining Region Numbers and Direction of Normal for Eq. (2.4)

$$\hat{n} \cdot (\hat{a}_1 \mathbf{E}_1 - \hat{a}_2 \mathbf{E}_2) = \tilde{n}_s \quad (2.4a)$$

$$\hat{n} \times (\mathbf{E}_1 - \mathbf{E}_2) = 0 \quad (2.4b)$$

Eq. (2.4a) states that the discontinuity at an interface in the normal component of the displacement flux is equal to the surface charge at the interface. Assume one region (2) is metallic so that the electric field goes to zero there. The total charge on a contact is then given by Eq. (2.5). The total charge is the sum at each face with a fixed potential (ϕ_o) of the incident displacement flux normal to the fixed electric potential boundary ($\epsilon \phi_i E_{ni}$) times the area of the face (A_i).

$$Q_{\phi_o} = \sum_{i=1}^{\text{faces with bc } \phi_o} \hat{a}_i E_{ni} A_i \quad (2.5)$$

A capacitance is calculated for each set of faces with a unique potential boundary condition. First the total charge on each collection of faces with a unique fixed potential boundary condition given by Eq. (2.5) is calculated. Then for those face sets with $\phi_o \neq 0.0$ the ratio $C = \frac{Q_{\phi_o}}{\phi_o}$ is calculated.

2.1.2 Electrostatic Pressure Force (Electric/Structural)

The coupling between the electrostatic model and the structural mechanics model is through the pressure forces. The electric model solves Poisson's equation and uses the electric fields to calculate the pressure force. The stress model uses the pressure forces as boundary conditions.

The force \mathbf{F} exerted by the total electric field \mathbf{E}_{tot} on a surface S with a surface charge ρ_s is given by

$$\mathbf{F} = \int_S \tilde{n}_s \mathbf{E}_{\text{tot}} da \quad \text{or} \quad d\mathbf{F} = \tilde{n}_s \mathbf{E}_{\text{tot}} da \quad (2.6)$$

The electric field at the surface is discontinuous across the surface interface as given by the electric field boundary conditions stated in Eq. (2.4).

A good approximation for the total electric field in Eq. (2.6) is to take the average of the electric field on either side of the interface.

$$\mathbf{E}_{\text{tot}} \approx \frac{1}{2} (\mathbf{E}_1 + \mathbf{E}_2) \quad (2.7)$$

Substituting Eq. (2.4a) and Eq. (2.7) into Eq. (2.6) yields

$$d\mathbf{F} = \tilde{n}_s \mathbf{E}_{\text{tot}} da = \tilde{n}_s \frac{1}{2} (\mathbf{E}_1 + \mathbf{E}_2) da = \hat{n} \cdot (\hat{a}_1 \mathbf{E}_1 - \hat{a}_2 \mathbf{E}_2) \frac{1}{2} (\mathbf{E}_1 + \mathbf{E}_2) da \quad (2.8)$$

So, the pressure force $d\mathbf{F}/da$ exerted by the total electric field \mathbf{E}_{tot} (approximated as an electric field average) on an area element da with a surface charge ρ_s separating two regions (1 and 2) is

$$\mathbf{P} = \frac{d\mathbf{F}}{da} = \hat{n} \cdot (\hat{a}_1 \mathbf{E}_1 - \hat{a}_2 \mathbf{E}_2) \frac{1}{2} (\mathbf{E}_1 + \mathbf{E}_2) \quad (2.9)$$

where the normal is directed toward region 1 and ϵ is the electric permittivity.

Eq. (2.9) can be simplified if one of the two regions is a metal. For instance, if region 2 is a metal, no electric field exists in the region ($\mathbf{E}_2 = 0$), and since the tangential component of the electric field is continuous across the interface (Eq. (2.4b)), the tangential component of the electric field in region 1 is also zero ($\mathbf{E}_{1t} = 0$). So, if region 2 is a metal then Eq. (2.9) reduces to

$$\mathbf{P} = \frac{d\mathbf{F}}{da} = \frac{1}{2} \epsilon_1 E_{1n}^2 \hat{n} \quad \text{if metal in region 2} \quad (2.10)$$

where E_{1n} is the normal component of the electric field in region 1, ϵ_1 is the permittivity in region 1, and the normal is directed toward region 1 as shown in Figure 2.1.

2.1.3 Virtual Force (Electric/Volume of Fluids)

A virtual force calculation was added to ease the coupling with a volume of fluids (VOF) model which is a technique for resolving free surfaces. Since boundary conditions at the free surface are no longer directly associated with a mesh face a force calculation that did not rely on an available list of boundaries was needed. The solution was to calculate the virtual force at a volume due to the varying electric energy in the region. The electrostatic potential is used to calculate a force at the surface of the liquid due to electrostatic pressure by solving

$$\mathbf{F}_{\text{virt}} = \nabla \left[\frac{1}{2} \epsilon |\nabla \phi|^2 \right] \quad (2.11)$$

where ϵ is the electric permittivity. The virtual force per unit volume \mathbf{F}_{virt} is obtained by taking the gradient of the energy per unit volume stored in the electric field. To couple electrostatics with VOF method, VOF is given access to electrostatic material properties and recalculates them as a function of fluid fraction. The conduction problem is then solved and the electrostatic virtual forces at every cell center is calculated by taking the gradient of the energy stored in the electric field. For coupling to the VOF method, the virtual force is applied only to cells which have a fractional content of the liquid. Elsewhere in the domain the force is assumed zero. These virtual forces are passed as body force to fluid model.

2.1.4 Electric Current Density (Electric/Magnetic, Electric/Heat)

The solution of the conduction equation (Eq. (2.2)) supplies links to magnetics, heat, and VOF models. The electric potential solution from the conduction problem is used to calculate source currents for the magnetics model, joule heating sources for the heat module, and body forces for the volume of fluids (VOF) model.

The conduction equation provides source currents (Eq. (2.12)) for the magnetics model. This is a useful method for describing source currents in that the user does not have to specify a direction of the current, it enables the use of source currents of arbitrary geometry, and it allows the current density direction to reflect any changes due to a moving grid.

$$\mathbf{J} = \sigma \mathbf{E} \quad (2.12)$$

When the conduction problem is solved a source term is also added to the heat equation ($\mathbf{J} \cdot \mathbf{E}$) due to current flow through conductive materials.

2.1.5 Boundary Element Method (BEM) and Finite Volume Method (FVM)

Two different techniques are available for solving the electric equations (Poisson or conduction equations). One is the finite volume method (FVM) and the other is the boundary element method (BEM). The FVM requires a volume mesh and calculates the electric potential (and the electric field) at every cell (volume) in the mesh. The BEM requires only a surface mesh (although volume information is required in defining the different “domains”) and calculates the electric potential (and the electric field) only at boundary and interface faces. A detailed discussion of BEM and FVM is given in the next chapter

2.2 Magnetic Model

A magnetic model was developed to compute forces on conductive flows and model microsystems which rely in part on magnetic actuation for operation. The magnetic model solves a reduced set of Maxwell's equations for a magnetic vector potential. The magnetic vector potential is used to calculate the magnetic field, forces on high permeability materials, and Lorentz forces on current carrying wires and conductive flows. The magnetics model has been implemented in 2-D, 2-D axisymmetric, and 3-D using the FVM.

The magnetic model solves Maxwell's equations for the magnetic vector potential \mathbf{A}

$$\nabla^2 \frac{\mathbf{A}}{\mu} = -\mathbf{J}_s - \sigma \mathbf{E} + \sigma \frac{\partial \mathbf{A}}{\partial t} \quad (2.13)$$

assuming negligible displacement current $\frac{\partial \mathbf{D}}{\partial t} = 0$, isotropic permeability μ , and the Coulomb gauge $\nabla \cdot \mathbf{A} = 0$. The current sources can be user specified (\mathbf{J}_s), calculated from the solution of a conduction problem ($\sigma \mathbf{E}$), or eddy ($-\frac{\partial \mathbf{A}}{\partial t}$) currents. Eq. (2.13) is solved on a 2-D (cartesian, cylindrical) or 3-D unstructured mesh using the FVM. In 2-D the source currents are scalars with assumed direction, $\tilde{\mathbf{J}}_s = \tilde{J}_z \hat{z}$ (cartesian), or $\tilde{\mathbf{J}}_s = \tilde{J}_\phi \hat{\phi}$ (cylindrical). From the magnetic vector potential the magnetic field \mathbf{B} can be calculated ($\mathbf{B} = \nabla \times \mathbf{A}$).

For sinusoidal current sources (ac case) the equation can be solved in phasor form to obtain the sinusoidal steady state solution

$$\nabla^2 \frac{\tilde{\mathbf{A}}}{\mu} = -\tilde{\mathbf{J}}_s + j\sigma\omega\tilde{\mathbf{A}} \quad (2.14)$$

The coupling between the magnetic model and the structural mechanics model is through volume forces. The magnetic model solves Eq. (2.13) or Eq. (2.14) for the magnetic vector potential \mathbf{A} which is used to calculate the magnetic field ($\mathbf{B} = \nabla \times \mathbf{A}$). The magnetic field is used to calculate a volume force. The stress model uses the volume forces as body force conditions. Different regions such as current carrying solids/fluids and high permeability solids require different force calculations.

2.2.1 Magnetic Force on Current Carrying Wire (Magnetic/Structure)

For regions where current sources exist the incremental force $d\mathbf{F}$ due to a magnetic field \mathbf{B} on an incremental volume element dv with a current density \mathbf{J} is calculated using

$$d\mathbf{F} = \mathbf{J} dv \times \mathbf{B} \quad (2.15)$$

2.2.2 Force on a High Permeability Material (Magnetic/Structure)

For regions where magnetized material exist either the virtual force per unit volume or the torque on a magnetic moment can be calculated.

Virtual Force

For regions where magnetized material exist the virtual force per unit volume on the volume element is calculated by taking the gradient of the magnetic energy density of the volume element, $\mathbf{F}_{\text{virt}} = \nabla U_{\text{mag}}$. If electric fields also exist in the region the energy density of the electric field is included in the gradient calculation. The instantaneous energy density of a magnetic field

is $U_{\text{mag}} = \frac{1}{2} \mathbf{B} \cdot \mathbf{H}$. When the fields are in phasor form $U_{\text{mag}} = \frac{1}{4} \text{Re}[\underline{\mathbf{B}} \cdot \underline{\mathbf{H}}^*]$ where the energy represents the average over one cycle, and the symbol “*” represents the complex conjugate.

Force Due to a Magnetic Moment

A magnetic moment force calculation has been added in addition to the virtual force calculation. A material with a magnetic moment \mathbf{M} placed in a magnetic field \mathbf{H} will experience a force \mathbf{F} given by

$$\mathbf{F} = \mu_0 (\mathbf{M} \cdot \nabla) \mathbf{H} \quad (2.16)$$

The magnetic moment \mathbf{M} is currently assumed proportional to the applied magnetic field ($\mathbf{M} = \chi_m \mathbf{H}$). So using the definition of a magnetic moment in terms of \mathbf{B} and \mathbf{H} , $\mathbf{M} = \mathbf{B}/\mu_0 - \mathbf{H}$ and the definition of relative permeability, $\mu_r = (1 + \chi_m)$ Eq. (2.16) becomes

$$\mathbf{F} = \left[\mathbf{B} \left(1 - \frac{1}{\mu_r} \right) \cdot \nabla \right] \frac{\mathbf{B}}{\mu_0 \mu_r} \quad (2.17)$$

which gives the force on a magnetizable material in terms of the applied magnetic field.

2.2.3 Force on a Conductive Flow (Magnetic/Flow)

The Lorentz force, $\mathbf{J} \times \mathbf{B}$ is included in the momentum equation for the flow of an electrically conductive fluid in a magnetic field. The current density \mathbf{J} is given by

$$\mathbf{J} = \sigma(\mathbf{E} + \mathbf{u} \times \mathbf{B}) \quad (2.18)$$

The Lorentz force can be expanded as

$$\mathbf{F} = \sigma(-\nabla\phi + \mathbf{u} \times \mathbf{B}) \times \mathbf{B} = -\sigma \nabla\phi \times \mathbf{B} + \sigma(\mathbf{u} \cdot \mathbf{B})\mathbf{B} - \sigma(\mathbf{B} \cdot \mathbf{B})\mathbf{u} \quad (2.19)$$

The last two terms damp the flow when the magnetic field \mathbf{B} and velocity \mathbf{u} are not aligned.

The current in the fluid is calculated from the conservation of charge. The divergence of the current density is zero, giving

$$\nabla \cdot \mathbf{J} = \nabla \cdot \sigma(-\nabla\phi + \mathbf{u} \times \mathbf{B}) = 0 \quad (2.20)$$

This equation is solved for the electric potential, ϕ . The electrostatic model was modified to include the term $\nabla \cdot \sigma(\mathbf{u} \times \mathbf{B})$. The boundary conditions for the electrostatic module have been modified to allow for insulated boundaries where the normal component of the current density vector is zero.

2.2.4 Joule Heating by Induction (Magnetic/Heat)

A time varying magnetic field generates a time varying electric field which generates eddy current in conductive materials. The flow of current through the conductor generates heat and is

called inductive heating. The inductive heating can be thought of as joule heating ($\mathbf{J} \cdot \mathbf{E}$) with the conductive currents ($\mathbf{J} = \sigma \mathbf{E}$) generated by the time varying field ($\mathbf{E} = -\nabla\phi - \partial\mathbf{A}/\partial t$). So assuming the electric field is due only to the time vary magnetic field ($\tilde{\mathbf{E}} = j\omega\tilde{\mathbf{A}}$) and the current is only a conduction current ($\tilde{\mathbf{J}} = \tilde{\sigma}\tilde{\mathbf{A}}$) the time averaged expression for joule heating becomes

$$\frac{1}{2} \text{Re}\{\tilde{\mathbf{J}} \cdot \tilde{\mathbf{A}}\} = \frac{1}{2} \sigma_r \omega^2 |\tilde{\mathbf{A}}|^2 \quad (2.21)$$

where σ_r is the real component of conductivity and ω is the radian frequency ($2\pi f$).

2.3 Flow Model

The fluid flow model solves the continuity equation and the pressure based Navier-Stokes equations (Patankar, 1980) assuming that the fluid is a continuum.

$$\frac{\partial \rho}{\partial t} + \frac{\partial}{\partial x_j} (\rho u_j) = \dot{m} \quad (2.22)$$

$$\frac{\partial}{\partial t} (\rho u_i) + \frac{\partial}{\partial x_j} (\rho u_i u_j) = - \frac{\partial p}{\partial x_i} + \frac{\partial \tau_{ij}}{\partial x_j} + \rho f_i \quad (2.23)$$

where ρ is the fluid density, u_j is the j^{th} Cartesian component of the instantaneous velocity, \dot{m} is the rate of mass generation in the system (typical examples of mass generation include surface reaction, spray vaporization etc.), p is the static pressure, τ_{ij} is the viscous stress tensor, and f_i is the body force (e.g., gravity, surface tension, etc.).

For very small flow dimensions and/or very low pressure gas flows, the mean-free path of the molecules λ becomes comparable to the characteristic flow dimensions L and the no-slip wall conditions associated with continuum assumption are no longer valid. For instance, low pressure gas flows in micro-fluidics. Use of no-slip walls under these conditions usually generates wall shear that is overestimated. If the operating conditions are such that the Knudsen number ($\text{Kn} = \lambda/L$) falls in the “transitional” regime ($0.01 < \text{Kn} < 3.0$), a slip-wall boundary condition is used. The slip-wall formulation includes effects of local temperature and diffusive creep in velocity slip. A formulation neglecting thermal effects can also be used (Rohsenow and Choi, 1961). Under low absolute pressures and gaseous mixtures the gas transport properties are not known and the Lennard Jones potential model can be used to calculate the transport properties of rarefied gas/gas mixtures at low absolute pressure. A detailed description is given in Bird et al., 1960.

The salient features of the fluid model are:

- pressure-based, implicit Navier-Stokes code
- incompressible and compressible flows
- turbulence models including standard k-e
- steady-state or transient problems
- multi-component diffusion
- multi-species transport
- multi-step gas phase chemical reactions
- surface reactions
- slip-wall boundary conditions

2.4 Heat Model

The thermal model solves the total enthalpy form of the energy equation

$$\frac{\partial}{\partial t}(\rho H) + \frac{\partial}{\partial x_j}(\rho u_j H) = \frac{\partial}{\partial x_j}(-q_j) + \frac{\partial p}{\partial t} + \frac{\partial}{\partial x_i}(\tau_{ij} u_j) - \frac{\partial}{\partial x_j}(J_{ij} h_i) + S_a + \rho f_i u_i \quad (2.24)$$

where J_{ij} is the total (concentration-driven + temperature-driven) diffusive mass flux for species i , h_i represents the enthalpy for species i , S_a represents additional sources due to surface reaction, radiation, joule heating, and liquid spray, and q_j is the j -component of the heat flux. Fourier's Law is employed to model the heat flux

$$q_j = -K \frac{\partial T}{\partial x_j} \quad (2.25)$$

where K is the thermal conductivity and T is the temperature. The total enthalpy H is defined as

$$H = h + \frac{u_j u_j}{2} \quad (2.26)$$

where h is the static enthalpy.

The energy equation includes unsteady, convective, conductive, species energy, viscous dissipation, work, joule heating and radiation terms. The conductive term uses conjugate heat transfer. The radiation source term in the energy equation is a solution of a radiative heat transfer equation for emitting, absorbing, scattering, gray medium using either a discrete ordinate method (Fiveland, 1984) or a surface-surface exchange method.

2.5 Mechanical Model

The mechanics equations describe the deformation of a solid body, and the resulting strains and stresses, under applied loads. These applied loads may be surface forces (e.g. pressure) and/or body forces (e.g. gravity).

2.5.1 Strain-Displacement Relations

In fluid mechanics, we are typically interested in measuring the velocity of fluid particles as they pass through a fixed point in space, and thus an Eulerian formulation is used. In solid mechanics, on the other hand, we use a Lagrangian formulation where a continuum undergoes a deformation with the motion expressed as:

$$\mathbf{R} = \mathbf{R}(\mathbf{r}, t) \quad (2.27)$$

which gives the current location \mathbf{R} of the particle that occupied the position \mathbf{r} at time $t = 0$. This may be thought of as a mapping of the initial configuration onto the current configuration. Thus, we may write

$$\mathbf{r} = x_i \hat{\mathbf{i}}_i \quad (2.28)$$

$$\mathbf{R} = \mathbf{r} + \mathbf{u} \quad (2.29)$$

Where \mathbf{u} is the displacement vector of the particle.

Consider an infinitesimal line segment on the undeformed and deformed bodies. The square of the lengths of this line segment are given by:

$$ds_0^2 = d\mathbf{r} \cdot d\mathbf{r} = dx_i dx_i \quad (2.30)$$

$$ds^2 = d\mathbf{R} \cdot d\mathbf{R} = \frac{\partial \mathbf{R}}{\partial x_i} \cdot \frac{\partial \mathbf{R}}{\partial x_j} dx_i dx_j \quad (2.31)$$

The difference between ds^2 and ds_0^2 is a measure of strain in the body, defined as

$$ds^2 - ds_0^2 = 2\gamma_{ij} dx_i dx_j \quad (2.32)$$

where γ_{ij} is called the Green-Saint-Venant strain tensor. Using Eqs. (2.28) through (2.31), the strain tensor is written as

$$\gamma_{ij} = \frac{1}{2} (u_{i,j} + u_{j,i} + u_{m,i} u_{m,j}) \quad (2.33)$$

This representation is referred to as the Lagrangian strain tensor since the initial coordinates were used as the basis.

If the displacement gradients $u_{j,i}$ are small in comparison to unity, the product term in Eq. (2.33) is negligible and the strain is represented by its linear portion.

$$\gamma_{ij} = \frac{1}{2} (u_{i,j} + u_{j,i}) \quad (2.34)$$

Such problems are referred to as geometrically linear.

2.5.2 Stress-Strain Relations

A body which has undergone deformation as a result of applied loads will transmit forces throughout its interior to balance the applied loads. As a result of forces being transmitted from one portion of the continuum to another, an element with area ΔA_n on or within the body and oriented with normal \mathbf{n} , will be subjected to a resultant force $\Delta \mathbf{F}_n$ and moment $\Delta \mathbf{M}_n$. The vector force and moment will not, in general, be parallel to \mathbf{n} .

The Cauchy Stress Principle states that the ratio $\Delta \mathbf{F}_n / \Delta A_n$ tends to be a definite limit as ΔA_n approaches zero, and also that the moment vanishes in the limiting process. The stress vector or traction is defined as

$$\mathbf{T}_n = \lim_{\Delta A_n \rightarrow 0} \frac{\Delta \mathbf{F}_n}{\Delta A_n} = \frac{d\mathbf{F}_n}{dA_n} \quad (2.35)$$

The traction \mathbf{T}_i , acting on a face normal to the Cartesian unit vector $\hat{\mathbf{i}}_i$, may be expressed in terms of the Cartesian stress tensor σ_{ij} as

$$\mathbf{T}_i = \sigma_{ij} \hat{\mathbf{i}}_j \quad (2.36)$$

The coefficients σ_{ij} represent components of the stress tensor. The subscript and sign conventions are as follows:

- The first subscript i refers to the normal $\hat{\mathbf{i}}_i$ denoting the face on which \mathbf{T}_i acts.
- The second subscript j refers to the direction $\hat{\mathbf{i}}_j$ in which the stress acts.
- The normal components (σ_{11} , σ_{22} , σ_{33}) are positive in tension and negative in compression.
- The shearing components σ_{ij} ($i \neq j$) are positive if directed in the positive x_j direction while acting on the face with the unit normal $+\hat{\mathbf{i}}_i$, or if directed in the negative x_j direction while acting on the face with unit normal $-\hat{\mathbf{i}}_i$.

If the Cartesian stress tensor σ_{ij} is known, this completely defines the state of stress at a point (Gould, 1983).

A relationship between the stress tensor σ_{ij} and strain tensor γ_{ij} may be derived as follows.

A generalized Hooke's Law formulation may be derived by assuming the existence of an elastic potential W which is invariant with coordinate transformations of the strain tensor γ_{ij} :

$$W = W(\gamma_{ij}) \quad (2.37)$$

Expanding this in a Taylor Series about $\gamma_{ij} = 0$ gives

$$W = W_0 + E_{ij} \gamma_{ij} + \frac{1}{2} E_{ijkl} \gamma_{ij} \gamma_{kl} + \frac{1}{6} E_{ijklmnp} \gamma_{ij} \gamma_{kl} \gamma_{mn} + \dots \quad (2.38)$$

where W_0 is a constant and

$$E_{ij} = \frac{\partial W}{\partial \gamma_{ij}}, E_{ijkl} = \frac{\partial^2 W}{\partial \gamma_{ij} \partial \gamma_{kl}}, E_{ijklmnp} = \frac{\partial^3 W}{\partial \gamma_{ij} \partial \gamma_{kl} \partial \gamma_{mn}}, \text{etc.} \quad (2.39)$$

Consider δW , a small change in energy due to $\delta\gamma_{ij}$,

$$\delta W = \sigma_{ij} \delta\gamma_{ij} \quad (2.40)$$

From Eq. (2.37), we can write

$$\delta W = \frac{\partial W}{\partial \gamma_{ij}} \delta\gamma_{ij} \quad (2.41)$$

We see from Eqs. (2.40) and (2.41) that the stress tensor and elastic potential are related by

$$\sigma_{ij} = \frac{\partial W}{\partial \gamma_{ij}} \quad (2.42)$$

Substituting Eq. (2.38) into Eq. (2.42) gives the stress-strain relationship

$$\begin{aligned} \sigma_{rs} &= \frac{\partial}{\partial \gamma_{rs}} \left(E_{ij} \gamma_{ij} + \frac{1}{2} E_{ijk} \gamma_{ij} \gamma_{km} + \dots \right) \\ &= E_{ij} \delta_{ir} \delta_{js} + \frac{1}{2} E_{ijk} (\gamma_{ij} \delta_{rk} \delta_{sm} + \gamma_{km} \delta_{ir} \delta_{js}) + \dots \\ &= E_{rs} + \frac{1}{2} (E_{ijrs} \gamma_{ij} + E_{rskm} \gamma_{km}) \\ &= E_{rs} + E_{rsij} \gamma_{ij} \end{aligned} \quad (2.43)$$

where the last step in Eq. (2.43) results from the symmetry relationship $E_{ijrs} = E_{rsij}$, as seen from the definition in Eq. (2.39). The term E_{rs} is the initial stress state, which may be taken as zero in the unconstrained state. Thus, the generalized Hooke's law for small strain elasticity is given by

$$\sigma_{ij} = E_{ijkl} \gamma_{kl} \quad (2.44)$$

The 81 coefficients E_{ijkl} are called elastic constants. With application of stress and strain tensor symmetry, the number of independent equations reduces from nine to six, and the number of elastic constants reduces to 21 (using symmetry of the E_{ijkl} tensor). Further reductions are possible for materials with one or more axes of symmetry.

Note that small strain does not necessarily imply small displacement gradients (and thus, a linear strain-displacement relationship). It is possible to have a large deformation, small strain problem.

2.5.3 Governing Equation of Mechanics

The governing equation of the mechanics module is written in terms of stress, which may then be related to displacement via the stress-strain and strain-displacement equations. The equation is derived using a balance of linear momentum as follows.

Consider a volume V with surface area A . The principle of linear momentum states

$$\int_V \mathbf{f} dV + \int_A \mathbf{T} dA = \int_V \rho \ddot{\mathbf{u}} dV \quad (2.45)$$

where \mathbf{f} is the body force, \mathbf{T} is the surface traction, ρ is the mass density, and \mathbf{u} is the displacement vector.

We write this in tensor form using

$$\mathbf{f} = f_i \hat{\mathbf{i}}_i \quad (2.46a)$$

$$\mathbf{T} = T_i \hat{\mathbf{i}}_i = \sigma_{ji} n_j \hat{\mathbf{i}}_i \quad (2.46b)$$

$$\mathbf{u} = u_i \hat{\mathbf{i}}_i \quad (2.46c)$$

The Green-Gauss theorem is used to convert the area integral of Eq. (2.45) into a volume integral:

$$\int_A \sigma_{ij} n_j \hat{\mathbf{i}}_i dA = \int_V \sigma_{ji,j} \hat{\mathbf{i}}_i dV \quad (2.47)$$

Equations (2.45) and (2.47) give

$$\int_V (\sigma_{ji,j} + f_i - \rho \ddot{u}_i) \hat{\mathbf{i}}_i dV = 0 \quad (2.48)$$

For this integral to vanish for all arbitrary volumes the integrand must vanish, which yields

$$\sigma_{ji,j} + f_i - \rho \ddot{u}_i = 0 \quad (2.49)$$

This is the equation of motion describing the distribution of stress in the body.

The balance of angular momentum shows that the stress tensor is symmetric (Chung, 1996), i.e.

$$\sigma_{ij} = \sigma_{ji} \quad (2.50)$$

Thus, Eq. (2.49) is often written as

$$\sigma_{ij,j} + f_i - \rho \ddot{u}_i = 0 \quad (2.51)$$

2.5.4 Multidisciplinary Coupling

The mechanics module is coupled to other modules of CFD-ACE+ through boundary conditions and source terms. These are described briefly below.

Coupling with Thermal Module Thermoelasticity

Temperature changes can be an important contributor to stress in elastic bodies. We assume a linear relationship between the temperature difference from a datum value and the corresponding strain:

$$\gamma_{(ii)}(T) = \alpha_{(i)}[T - T_0] \quad (2.52)$$

where the parentheses in the subscript implies no summation. Here $\gamma_{(ii)}(T)$ is the linear strain in coordinate direction i corresponding to the temperature difference $T - T_0$, and $\alpha_{(i)}$ is the coefficient of thermal expansion corresponding to that coordinate direction.

With Eq. (2.52), we generalize the stress-strain relations to

$$\sigma_{ij} = E_{ijkl}(\gamma_{kl} + \delta_{kl}\alpha_{(k)}[T - T_0]) \quad (2.53)$$

Coupling with Electrostatics and Fluids

The fluid and electrostatic modules are each coupled to the mechanics module via surface pressure terms. These enter the system as boundary conditions to Eq. (2.51), where the stress at the boundary is given by the expression

$$\sigma_{ij}n_j = pn_i \quad (2.54)$$

at a boundary with unit normal n . Here, p is the pressure from the fluids or electrostatics module.

Coupling with Magnetics

The magnetic model is coupled to the mechanics model via a body force. The magnetic body force can occur in current carrying wires where the moving charge experiences a force as it travels through a magnetic field (Eq. (2.15)). A magnetic force can also occur on magnetized material (Eq. (2.17)) as the magnetic field attempts to align the magnetic moment.

The body force vector \mathbf{f} is then given directly to Eq. (2.51) as a source term.

3. BOUNDARY ELEMENT AND FINITE VOLUME METHODS

Two different techniques are available for solving the electric equations (Poisson or conduction equations). One is the finite volume method (FVM) and the other is the boundary element method (BEM). The FVM requires a volume mesh and calculates the electric potential (and the electric field) at every cell (volume) in the mesh. The BEM requires only a surface mesh (although volume information is required in defining the different "domains") and calculates the electric potential (and the electric field) only at boundary and interface faces. The two methods will be discussed, followed by a brief discussion comparing the methods. The benchmarks comparing the two methods are provided in Chapter 5.

3.1 Boundary Element Method (BEM)

BEMs deal with "boundary elements" which separate "domains". The boundary elements are defined by a surface grid S . A domain is a region in space with a unique ϵ_r or where no solution is being computed (an empty domain). BEM can solve both bounded and unbounded problems. For unbounded problems the potential at infinity is assumed zero (i.e., $\phi(\infty) = 0$).

Significant enhancements were made to the CFDRC BEM solver to obtain $O(N)$ computation times for both the Laplacian and the Navier equations. The first phase of development involved the implementation of a stable fast boundary element solver/ library for Laplace/Poisson, Stokes, and Navier equations using low order interpolation and multipole-like expansions.

The BEM solver is capable of solving different equation types including Laplace/ Poisson, Navier, Stokes, and Helmholtz at low frequency. Boundary conditions BEM supports include Dirichlet, Neumann, and third kind (convective for Laplace and spring support for Navier). Multi-domains, each with different set of properties, are supported. Continuity of the primary variable (temperature, electric potential, displacement) as well as the secondary variable (fluxes and tractions) are automatically handled across the interface. A new method (developed within CFDRC) is used to evaluate the boundary integrals. The method is similar to the multipole method, but is applicable to any boundary integral equation, including the 3-D Navier equation. Sources terms (terms typically placed on the right-hand side of the equations and are not a function of the primary variable solved) are approximated by particles. Fast summations of the sources terms are used. The time complexity is $O(\log M)$ for each summation of the contribution of M particles. A "matrixless" generalized minimal residual (GMRES) method is used to solve the linear equation systems iteratively. A diagonal preconditioner is used everywhere except on the interfaces, where a 2×2 submatrix preconditioner is used. The overall time complexity is $O(N)$ without sources and $O(N \log M)$ with sources for each iteration. The total time also depends on the number of iterations of the GMRES method. This number is in turn problem dependent and preconditioner dependent. In general, about $N^{0.05 \sim 0.25}$ iterations are needed. Therefore, the time dependence is roughly $O(N^{1.05 \sim 1.25})$ or $O(N^{1.05 \sim 1.25} \log M)$. The spatial dependence is $O(N+M)$. For small problems (with up to a few hundred elements), conventional $O(N^2)$ BEM can be faster than accelerated BEM. The conventional BEM solver can be activated by a simple parameter setting. The BEM libraries are accessible through C function calls. The user can print the results in CFD-VIEW format or VRML.

3.1.1 Overview

The BEM for the electric problem uses the “FastBEM” solver. The FastBEM solver is a general purpose BEM solver developed at CFDRC and capable of solving Navier-Stokes and Laplace-like equations. In general, FastBEM can be used to solve any equations of the form

$$\int_S [H(\mathbf{r}' - \mathbf{r})u(\mathbf{r}') - G(\mathbf{r}' - \mathbf{r})q(\mathbf{r}')] dS\mathbf{r}' = \int_V [K(\mathbf{r}' - \mathbf{r})s(\mathbf{r}')] dV(\mathbf{r}'), \mathbf{r} \in \Omega \quad (3.1)$$

where H , G , and K are kernel functions, s is a source term, u is the primary variable, q is the “flux” variable, and the integrals are over a closed surface S containing a volume V . The electrostatic module will use the Laplace-like form of Eq. 3.1 which is

$$\int_S \left[\left(-\frac{1}{\epsilon} \frac{\partial}{\partial n} \left(\frac{1}{4\pi r} \right) \right) \phi(\mathbf{r}') - \frac{1}{4\pi r} \left(-\epsilon \frac{\partial}{\partial n} \phi(\mathbf{r}') \right) \right] dS(\mathbf{r}') = - \int_{S_v} \frac{1}{4\pi r} \rho(\mathbf{r}') dV(\mathbf{r}'), \mathbf{r} \in \Omega \quad (3.2)$$

where $r = |\mathbf{r}' - \mathbf{r}|$, n is the normal to the surface S , ϕ is the electric potential, ϵ is the electric permittivity, and ρ is the space charge.

The surface(s) S is(are) divided into boundary elements, and hierarchically arranged. For example, the elements in S can be divided into subgroups $S1$ and $S2$ such that $S = S1 + S2$. Similarly, $S1 = S11 + S12$, $S2 = S21 + S22$, and so on. Any tree structure can be used for the hierarchical arrangement, an octree is used in many multipole methods. FastBEM uses a balanced axis aligned binary tree.

In general FastBEM is flexible and able to solve different equation types. The penalty for this flexibility is more memory and CPU time. Therefore, a technique called “code specialization” was introduced. A specialized version of FastBEM has been created to handle only a single type of equation, with corresponding gains in memory and time efficiency (by more than 100%). If needed, the original general version can be also compiled, with a simple compiling option.

3.1.2 Space Charge Approximation

The space charge source term is approximated as a summation of point charges in FastBEM. That is,

$$\rho(\mathbf{r}) \approx \sum_{i=1}^{n_{\text{sources}}} Q_i \delta(\mathbf{r} - \mathbf{r}_i) \quad (3.3)$$

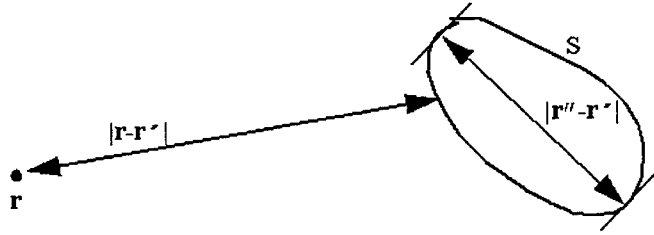
$$Q_i = \int_{v_i} \rho(\mathbf{r}) dv_i \quad (3.4)$$

where \mathbf{r}_i and Q_i are the location and the strength of the point charge i respectively, n_{sources} is the number of point charges, δ is the direct delta function, and v_i is the volume over which a point charge i has been approximated.

3.1.3 Kernel Expansion and Fast Integration

When the minimum distance between a position \mathbf{r} and a surface S is large compared to the distance between the furthest two points on a surface S the kernel functions become smooth and can be approximated by low order expansion. That is for a scaling parameter $0 < \theta < 1$. In the extreme case $\theta \ll 1$,

When the minimum distance between a position \mathbf{r} and a surface S is large compared to the distance between the furthest two points on a surface S the kernel functions in 8.1 become smooth and can be approximated by low order expansion. That is for a scaling parameter $0 < \theta < 1$.



$$\theta \left[\min_{\mathbf{r}' \in S} \|\mathbf{r} - \mathbf{r}'\| \right] = \max_{\mathbf{r}', \mathbf{r}'' \in S} \|\mathbf{r}'' - \mathbf{r}'\| \quad (3.5)$$

In the extreme case $\theta \ll 1$, a kernel can be approximated by a single term approximation. For a kernel $K(\mathbf{r}' - \mathbf{r})$ the approximation is a single value of K at the center $\mathbf{r}_{\text{center}}$ of a surface S , that is $K(\mathbf{r}' - \mathbf{r}) \approx K(\mathbf{r}_{\text{center}} - \mathbf{r})$. For $\theta = 0$ no (\mathbf{r}, S) pair can satisfy Eq. (8.5), so all calculations have to be performed with no optimization. In this case, the conventional BEM is recovered. Currently in FastBEM the kernels are expanded using the Taylor series expansion if they meet the criteria for expansion.

For quadpole expansions in their optimal performance range, the solution error in primary variables (temperature, electric potential and displacement) is typically 5% to 10%. The error in secondary variables (heat flux, electric field, and traction) is even larger. Higher order expansions are available. The expansions have been implemented in a hierarchy of C++ classes. Two general expansion schemes of any user specified order are available.

Once a position \mathbf{r} and a surface S in Eq. (3.2) satisfies the distance condition in Eq. (3.5), the kernel can be approximated by a few terms of its expansion (such as Taylor series), and the integral can be quickly evaluated. If a position \mathbf{r} relative to a surface S does not satisfy the distance condition in Eq. (3.5) one moves down the sort "tree" to subsets of the surface S (S_1 , S_2 , etc.) to see if (\mathbf{r}, S_1) , (\mathbf{r}, S_2) , etc. pairs satisfy the distance condition. If any pairs satisfy the distance condition then the integral is approximated by a set amount of terms of a series expansion (such as a Taylor series expansion), otherwise the surface is broken down further and the condition is tested for again.

Even more efficiency is gained when \mathbf{r} is also arranged into hierarchies. So, the criteria for the expansion of a kernel is not only between a position in space \mathbf{r} and a surface S (\mathbf{r}, S) but (S, T) pairs between two surface groups one in $\mathbf{r} \in T$ and the other in $\mathbf{r}' \in S$. Whether $(T, S) = (T_1, S) +$

(T_2, S) or $(T, S) = (T, S_1) + (T, S_2)$ is used depends on which grouping increases the efficiency of the calculation.

For piecewise constant interpolations, semi-analytical integration methods are usually used for all kernels. For higher order interpolations, pure numerical integration was used. The latter is very slow, and consumes considerable CPU time. During testing it was found that for some problems in elastostatics at least linear interpolation is needed. Therefore, a similar semi-analytical integration method has been implemented for the higher order interpolations (linear to cubic) for quadrilateral and triangle boundary elements. For other polygon elements, piecewise constant interpolation is retained. Semi-analytical integration schemes were introduced in the BEM model for the singular integrals and integrals in which the source point and the integration domain are co-planar. This capability is now available for the Laplacian/Poisson and Navier kernels with constant and linear interpolations. The analytical integrals reduce the computational time significantly, e.g., for a capacitance extraction problem (for a unit cube with 2400 faces), the analytical integrals reduce computation time by a factor of 3, i.e., 2.87 s from 9.08 s with numerical integration.

3.1.4 FastBEM Implementation

FastBEM is written in C++ and is accessed by ACE+ through C subroutine calls. FastBEM deals with “boundary elements” which separate “domains”. A domain is a region in space with a unique ϵ_r or where no solution is being computed (an empty domain). FastBEM requires a list of nodes which make up the boundary elements, the nodes physical position, the node to boundary element connectivity, a list of domains, the domain present on either side of a boundary element, the boundary condition on a side opposite the end of an empty domain if present, and the location and strength of the point source terms. The node order which specifies a boundary element follows the right-hand rule for face normal definition. A boundary element face “side” uses the normal from the face to distinguish between sides.

The problem specification (grid, boundary conditions, material properties, space charge volume conditions, and solution method) is inputted into the electrostatic module using a DTF file format. If the solution method is the BEM then the problem specification data is reorganized for submittal to FastBEM subroutines.

Rules were established for “faces” which will **not** be submitted to FastBEM as boundary elements: (i) faces between two non -1 domains with a boundary condition other than dielectric/dielectric, (ii) faces between two $\epsilon_r = 0$ (i.e. “empty”, or metal) domains, (iii) faces between two similar domains (ϵ_r and `mat_type` the same), and (iv) faces with “ignore” boundary condition.

The FastBEM libraries for solution of Laplace-like equations are used within the CFD-ACE+ environment. A connection of the FastBEM Laplace-like equation solver to the GUI was implemented through C subroutine interface calls supplied by the FastBEM libraries. Problem specification data such as boundary conditions, domain information, and permittivity values, and charge distributions are processed into a form recognized by FastBEM. A special permittivity value is used to flag to FastBEM the presence of a closed domain.

3.1.5 FastBEM Grid Adaptation

Grid adaptation capability (for BEM) has been added as an independent module. It reads in the original grid file and the initial solution by FastBEM, and generates a new grid adapted to the solution. Figure 3.1 demonstrates grid adaptation in a BEM solution.

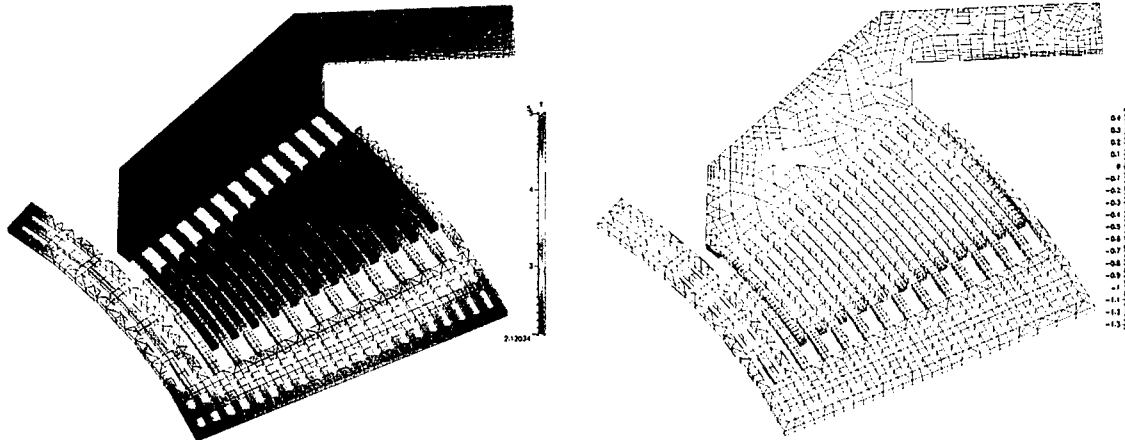


Figure 3-1. Grid Adaptation in FastBEM

3.2 Finite Volume Method (FVM)

The FVM for the electric problem uses finite differencing and the Divergence Theorem to discretize the solution space

$$\int_V \nabla \cdot \mathbf{f} dV = \oint_S (\mathbf{f} \cdot \hat{\mathbf{n}}) dS \quad (3.6)$$

$$\nabla \cdot \mathbf{f}_{\text{cell}} = \frac{\sum_{i=1}^{\text{cellfaces}} A_j f_j}{V} \quad (3.7)$$

The normal diffusive fluxes ($\mathbf{f} \cdot \hat{\mathbf{n}}$) are approximated as the ratio of the difference of cell center values and cell to face distances. The resulting difference equation is solved using an iterative conjugate gradient solver (CGS).

3.3 BEM vs. FVM

The cpu “price” per element (cell) is much greater for BEM than for FVM. A typical question then is, “when is one method “better” or “worse” to use than the other?” In most cases, FVM is the “better” method. There are two instances when BEM is the better or only choice. One is if the “volume cell” to “boundary + interface face” ratio is on the order of 100 or 1000. In this case the higher cpu cost per element of BEM is offset by the fewer number of elements in the BEM computation (boundary + interface faces) compared to the number FVM will use (volume cells). Another instance when BEM may be chosen over FVM is for unbounded problems, that is problems with an infinite domain. The FVM requires extra cells to extend the boundary to a region where the solution no longer varies, approximating the infinity point. With BEM no extra meshing is required to extend the domain.

4. INTEGRATION OF PHYSICAL MODELS INTO COMMERCIAL CAD TOOL

4.1 CFD-ACE+MEMS CAD System

The main objective of the proposed study is to develop an integrated commercial CAD tool for MEMS applications. It is therefore important to link the physical models with other peripheral software (such as grid generators, geometry modelers, visualization software, Graphical User Interfaces, interfaces to other CAD packages, etc.) to enhance the value of the physical models as a design tool. The thermo-fluidic-mechanical-electric-magnetic model developed during this project has been incorporated into a design software environment, the CFD-ACE+MEMS CAD system shown in Figure 4-1. The design environment for MEMS which has been developed includes grid generation (CFD-GEOM), data visualization (CFD-VIEW), graphical problem setup (CFD-GUI), and coupled fluidic, thermal, mechanical, electric, and magnetic physical model solvers (CFD-ACE, CFD-ACE(U)).

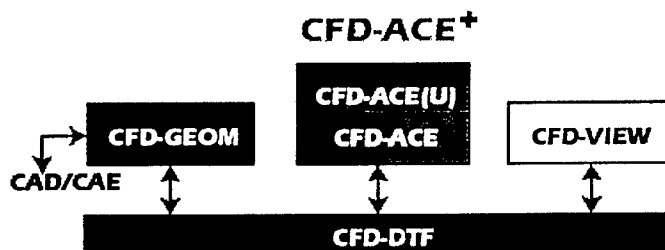


Figure 4-1. The CFD-ACE+MEMS CAD System

Geometry Modeling and Grid Generation Tool: The CFD-GEOM software developed by CFDRC is used to define the geometric details of MEMS devices. CFD-GEOM is a NURBS based 3-D geometric modeler. It has points, lines, curves and surfaces as the basic geometric entities from which complex geometries can be defined. It is possible to import geometric definitions from other CAD tools (Pro/ENGINEER, MICROSTATION, ICEM, and AutoCAD) through IGES files. GEOM can also import ECAD formats such as CIF and GDSII. Additionally, GEOM has interfaces to facilitate geometry and data transfer from other commercial CAD packages such as Pro/ENGINEER, AutoCAD.

CFD-GEOM can be used to create both structured and unstructured meshes for the simulations. The basic entities for creating meshes include edges, faces, loops, surfaces, blocks, and domains. It is also possible to form prisms (triangles extruded in the third dimension) which are useful for device geometries which have most of the spatial variation in two dimension.

Visualization Tool: CFD-VIEW, developed by CFDRC, is used to visualize the results of simulations. The input formats recognized by this package include FAST-U, hybrid, mixed-u, polyhedral, PLOT3-D data sets (NASA Standard) or the DTF format developed by CFDRC.

Visual Environment: The Visual Computing Environment (VCE) capability being developed at CFDRC for parallel execution of multi-disciplinary analysis codes will also be available in the

CAD tool environment. VCE is an object-oriented environment for running multiple software modules on a network of heterogeneous workstations.

Graphical User Interfaces (GUIs): Complete access to the CAD tool is provided through a master GUI. This GUI facilitates access to any of the individual modules such as CFD-ACE, CFD-GEOM, CFD-VIEW, etc.

Physics Solvers: CFD-ACE and CFD-ACE(U) are modules of the CFD-ACE+MEMS analysis package. They provide the tools to specify, and iteratively solve, the equations that describe the physical processes for fluidic, thermal, mechanical, electric, and magnetic problems. The physical models are solved on a 2-D, cylindrical, or 3-D multi-domain grid. The grid can be structured, unstructured, hybrid, or adaptive Cartesian. There is also a moving grid capability to track moving and deforming bodies and surfaces. Strong links exist with data transfer facilities (DTF), parallel execution on multiple machines using the message passing interface (MPI), and a link with ADAPTER for solution based grid refinement/adaptation. The physical models are implemented in a highly modularized code architecture which facilitates the addition of future physical models.

In addition to the above mentioned existing software modules, a virtual component library and a MEMS knowledge base (to be developed under an ongoing project) will be integrated with the software environment. The component library will contain a set of predefined, parameterized components which can be used to design a complicated system. The knowledge base will contain flow and process parameters and their relationships for these components. It will also contain design rules and guidelines for integration with other components.

4.2 Electric Model in CFD-ACE+MEMS CAD System

The electric model physics solver was discussed in the previous chapters. In this section the electric problem specification capabilities in CFD-ACE+MEMS will be discussed. First, the problem specifications that are common to both FVM and BEM solution methods of the electric model are given. The common problem specification options are the boundary conditions, relative permittivity material property, and the space charge volume condition. This is followed by a discussion of additional problem set-up specific to FVM and BEM solution methods. Finally, the variables deposited to the DTF formatted input/output file will be discussed.

A user can choose between FVM and BEM using the dialog shown in Figure 4-2.

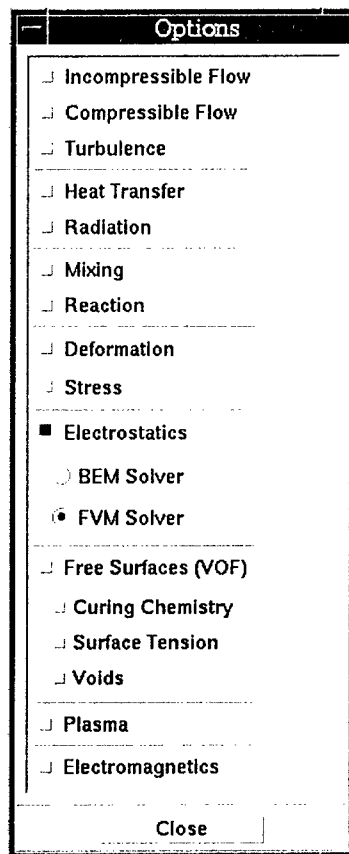


Figure 4-2. Dialog Where Electric Model is Chosen and Either FVM or BEM Solver is Selected

4.2.1 **Electrostatic Boundary Conditions**

The five boundary conditions available in the module and shown in Figure 4-3 are specifying the value of the potential at a cell face (Eq. (4.1)), specifying the negative normal potential gradient (electric field normal) at a cell face (Eq. (4.2)), specifying a mixture of fixed potential and electric field normal (Eq. (4.3)), indicating a cell face is at a dielectric interface which is useful when specifying an unbounded problem, and an ignore boundary condition which is useful when multi-disciplinary problems are specified.

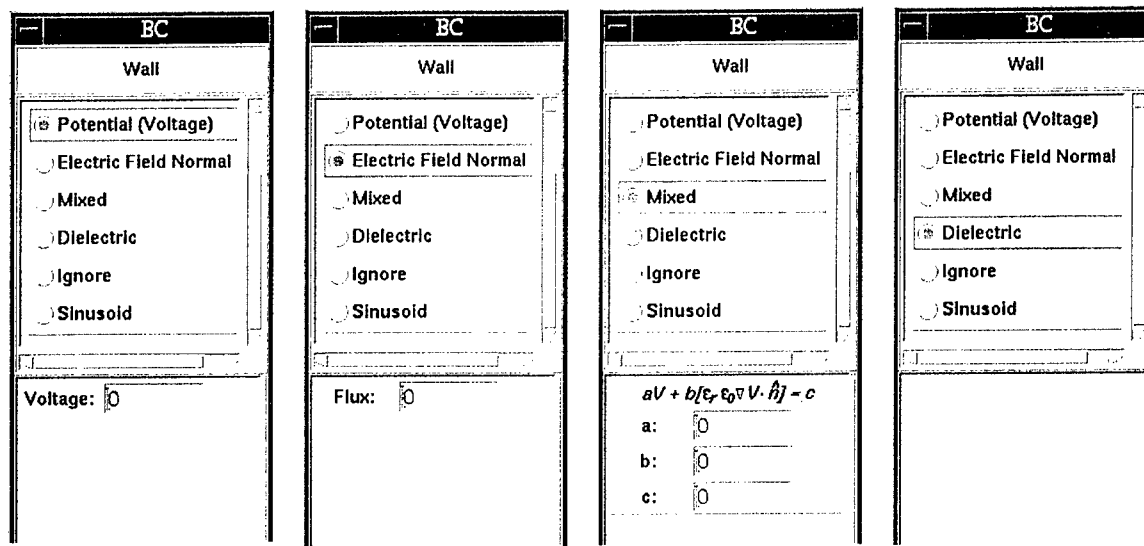


Figure 4-3. Electrostatic Boundary Conditions Window at Model."Bond.Cond.": "Surface BC".Values

4.2.1.1 Fixed Potential or "Potential (Voltage)". The "Potential (Voltage)" boundary condition in the GUI allows the specification of a fixed potential at a cell face. Clicking on "Potential (Voltage)" causes a "Voltage:" labeled box to appear. One then specifies the voltage in units of volts that the selected face(s) should be fixed at.

$$\phi = \phi_0 = \text{Voltage} \quad (4.1)$$

4.2.1.2 Fixed Flux or "Electric Field Normal". The "Electric Field Normal" boundary condition in the GUI allows the specification of a fixed electric field normal at a cell face weighted by a relative permittivity. Clicking on "Electric Field Normal" causes a "Flux:" labeled box to appear. One then specifies the electric field normal or flux in units of volts/meter that the selected face(s) should be fixed at.

$$-\epsilon_r \nabla \phi \cdot \hat{n} = \text{Flux} \quad (4.2)$$

The normal direction is away from the mesh at mesh end, toward the solid at a solid/fluid interface, and dependent on the node order of the face at a solid/solid interface.

4.2.1.3 Mixture of Fixed Potential and Flux or "Mixed". The "Mixed" boundary condition in the GUI allows the specification of a mixture of fixed potential and fixed electric field normal at a cell face. Clicking on "Mixed" causes three boxes labeled "a:", "b:", and "c:" to appear. One then specifies the values for the constants a, b, and c which fit the following equation.

$$a\phi - b\epsilon_r \nabla \phi \cdot \hat{n} = c \quad (4.3)$$

4.2.1.4 Dielectric/Dielectric Interface or "Dielectric". The "Dielectric" boundary condition in the GUI is used to indicate that a dielectric/dielectric interface exists. Interfaces which separate

regions of different permittivity within the grid are dealt with automatically in the code so there is no need to apply the “Dielectric” boundary condition at these interfaces. The boundary condition is used for electrostatic problems when the BEM solver is used. The boundary condition allows the user to include faces in the calculation where the voltage value is desired but no knowledge of the potential or its gradient is known. Clicking on “Dielectric” causes no labeled boxes to appear. This boundary condition does not require any constants to be specified.

4.2.1.5 No Electrostatic Boundary Condition Exists or “Ignore”. The “Ignore” boundary condition in the GUI is used to indicate that a set of faces has no electrostatic boundary conditions. This boundary condition is useful when multi-disciplinary problems are being specified. A set of faces may require a boundary condition to be specified in one problem type but have no boundary conditions applicable for another problem type. The “Ignore” boundary condition allows one to specify that a set of faces has no electrostatic boundary condition although it may have a boundary condition for another problem type. Clicking on “Ignore” causes no labeled boxes to appear. This boundary condition does not require any constants to be specified.

4.2.1.6 Symmetry. The symmetry boundary condition in the GUI is used to specify areas of symmetry in the grid. That is, specify symmetry planes. Mathematically it is equivalent to $-\epsilon_r \nabla \phi \cdot \hat{n} = 0$ or the field normal at a face is equal to zero. This boundary condition does not require any constants to be specified. It should be noted that for unbounded problems solved with BEM there is no possibility of specifying a symmetry plane. An infinite plane would need to be specified with a zero normal field.

4.2.2 Electrostatic Volume Conditions

The two electrostatic volume conditions that can be specified are the relative electric permittivity ϵ_r , and space charge ρ , as defined in Eq. (2.1).

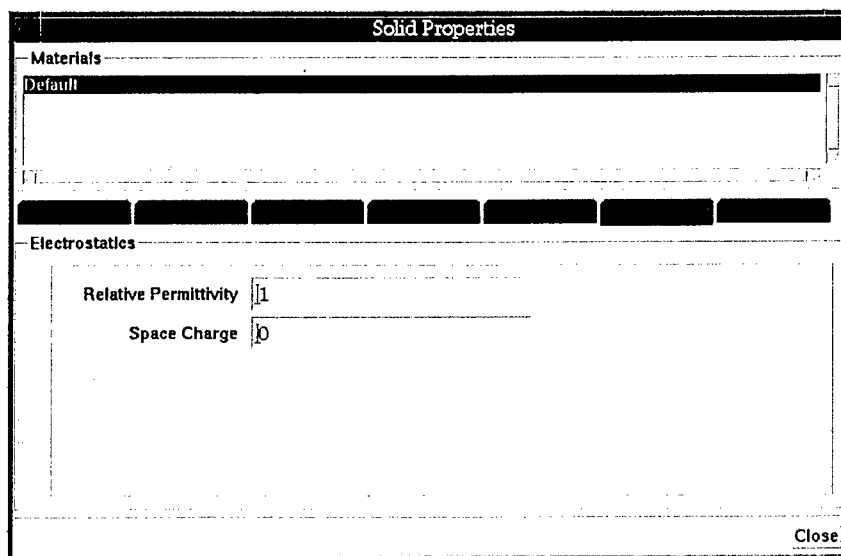


Figure 4-4. Electrostatic Volume Conditions Window at Model.Prop.Solid.Electrostatics or Model.Prop.Gas.Electrostatics

4.2.2.1 Electric Permittivity. Only the relative permittivity ϵ_r of the total electric permittivity $\epsilon_r \epsilon_0$ is set in the GUI. The value used for the permittivity of free space is $\epsilon_0 = 8.854187 \times 10^{-12}$ F/m or C²/Nm². The relative permittivity defaults to 1.0 for all cells in the grid.

To specify a metal (or an empty domain in FastBEM) the relative electric permittivity for the group of cells should be set to zero. No electric field exists in a metal and a relative electric permittivity of zero is used in the code as a flag to indicate that a group of cells should not be included in the solution to Poisson's equation. In the FVM the cells are "blocked" so that the electric potential and field are not solved for those cells. In the BEM, setting a group of cells to zero relative electric permittivity is equivalent to establishing an empty domain. If fixed potential, fixed flux, or mixed boundary conditions are set on a face one of the two domains the face separates must be an empty domain.

4.2.2.2 Space Charge. The space charge ρ of a group of cells can be specified in the GUI in units of C/m³. The space charge defaults to 0.0 for all cells in the grid.

4.2.3 FVM Control Parameters

The FVM control parameters for the electrostatic problem are accessed at different places in the GUI. The iteration number and final residual are accessed at Solve.Control.Electrostatics. The solver, relaxation, and limits are accessed at Solve.Control. The FVM control parameters windows are shown in Figure 4-5.

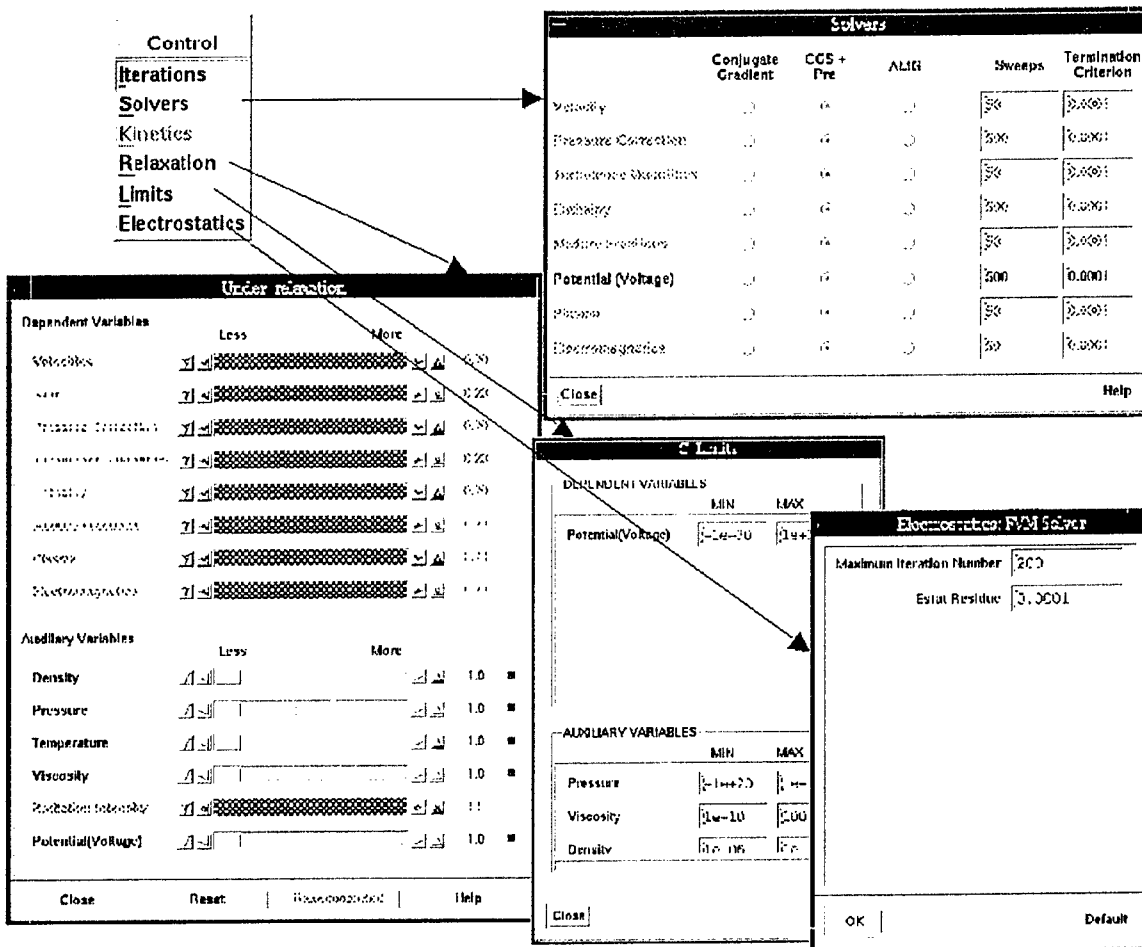


Figure 4-5. An Overview of the FVM Controls. The control menu (upper left) is used to reach the solver, relaxation, limits, iteration, and residue controls.

4.2.3.1 Maximum Iteration Number

> 0

The “Maximum Iteration Number” controls the maximum number of iterations to be made by the FastBEM algorithm before exiting. The default value is 200.

4.2.3.2 Residue

> 0

The “Residue” is the desired residue reduction factor for the electric potential. The residue is normalized to one at the beginning of the calculation. The calculation will stop when either the desired electric potential residue has been achieved or the maximum iterations have been exceeded. The default value is 1.0×10^{-4} .

4.2.3.3 Electric Potential Limits. A maximum and minimum value can be set on the value of the electric potential as it is being solved.

4.2.3.4 Under Relaxation. Under relaxation can be used when solving the electric potential using FVM which weights the current solved value with the previous solution.

4.2.3.4 Linear Solver. The type of linear solver can be chosen (conjugate gradient, arithmetic multi-grid), as well as the maximum number of sweeps to take in the solver and the residual reduction criteria for exiting the solver.

4.2.4 BEM Control Parameters

The BEM control parameters for the electrostatic problem are accessed at Solve.Control.Electrostatics. The Electrostatic option is not available in the Control.Solve menu unless the Model.Problem_Type.Options.Electrostatics.BEM Solver option has been selected. The BEM control parameters window is shown in Figure 4-6.

Electrostatics: BEM Solver	
Interpolation Order	0
Maximum Iteration Number	200
Gmres Restart Steps	10
Expansion Mode	1
Expansion Order	2
Distribution Criteria	0.5
Estat Residue	0.0001
<input type="checkbox"/> Unbounded	
<input type="button" value="OK"/> <input type="button" value="Default"/>	

Electrostatics: BEM Solver	
Interpolation Order	0
Maximum Iteration Number	200
Gmres Restart Steps	10
Expansion Mode	1
Expansion Order	2
Distribution Criteria	0.5
Estat Residue	0.0001
<input checked="" type="checkbox"/> Unbounded ϵ_r 1	
<input type="button" value="OK"/> <input type="button" value="Default"/>	

Figure 4-6. BEM Control Parameters Window at Solve.Control.Electrostatics

4.2.4.1 Interpolation Order

- 0 - uniform (anything larger than 0 is very computational expensive)
- 1 - linear

The “Interpolation Order” controls the interpolation level on a face where the potential and/or gradient will be solved. Higher interpolation order leads to better accuracy in results but increases the computational expense of the calculation drastically. Only zeroth (uniform) and

first order (linear) interpolation are currently available. In addition first order interpolation is only available for n-polygon faces of $n = 3$ or 4 (i.e., triangles and quadrilaterals) faces. If first order interpolation is specified any n-sided polygon faces greater than four will use zeroth order interpolation. Zeroth order introduces only one node/face at face center. First order interpolation introduces n nodes for an n-sided polygon face. Inputted values less than zero are changed to zero. Inputted values greater than 1 are changed to 1. The default value is 0.

4.2.4.2 Maximum Iteration Number

> 0

The “Maximum Iteration Number” controls the maximum number of iterations to be made by the FastBEM algorithm before exiting. The default value is 200.

4.2.4.3 Gmres Restart Steps

> 0

A matrix-less GMRES method is used to solve the equation systems iteratively. A diagonal preconditioner is used everywhere except on the interfaces, where a 2×2 submatrix preconditioner is used. The “Gmres Restart Steps” parameter controls the number of sweeps within the linear solver for each iteration. The default value is 10.

4.2.4.4 Expansion Mode

1

The “Expansion Mode” controls the method of approximating the kernel function as a series expansion. Currently only Taylor series expansion of the kernel function is available. Multipole expansion itself is not implemented due to its lack of generality. In the future other expansion modes may become available. The default and only possible value is 1 so any changes made here will not effect the solution.

4.2.4.5 Expansion Order

0-4

The “Expansion Order” is the order of the kernel series expansions (currently only the Taylor series expansion is available). The default value is 2.

4.2.4.6 Distribution Criteria

$0.0 \leq x \leq 1.0$

The “Distribution Criteria” is the multipole accuracy parameter. Loosely put the parameter controls the level of “fast” in the FastBEM algorithm that is used. The “Distribution Criteria” is

connected to the θ of Eq. (3.3). A value of zero is conventional BEM with no attempts made to speed up the algorithm. The solution will have a high level of accuracy but the solution speed will be very slow. As the parameter is increased from zero the level of optimization increases as attempts are made to speed the level of convergence. Mechanisms such as clumping together boundary elements into an equivalent boundary element are used. The benefits of optimization (larger Distribution Criteria values) are faster solutions. The drawbacks are a lower level of accuracy of the solutions and an increase in the memory requirements to achieve a solution. The suggested value is around 0.5. Inputted values greater than one or less than zero are changed to 0.5. The default value is 0.5.

4.2.4.7 BEM Residue

> 0

The “BEM Residue” is the desired residue reduction factor for the electric potential. The residue is normalized to one at the beginning of the calculation. The calculation will stop when either the desired electric potential residue has been achieved or the maximum iterations has been exceeded. The default value is 1.0×10^{-4} .

4.2.4.8 Unbounded. The “Unbounded” toggle specifies if the problem is bounded or unbounded. A bounded problem assumes the boundary elements bound the solution space. An unbounded problem assumes a solution is unbounded with the electric potential $\phi(\infty) = 0$. “Unbounded” is true (toggle on) if the problem is an unbounded problem, false (toggle off) if the problem is bounded.

4.2.4.9 Relative Permittivity ϵ_r

> 0.0

The relative permittivity in the unbounded region. The relative permittivity in the unbounded region can not be specified unless the unbounded option has been selected. The default value is 1.0.

4.2.5 Electric Model DTF Output

The values deposited by the electrostatic module into the DTF file are different depending on the method used (BEM or FVM) to solve Poisson’s equation.

4.2.5.1 BEM Electrostatic Output

cfv-view	description	symbol	units
elpot	electrostatic potential	ϕ	V
epsr_e_En	electric field normal	$-\epsilon_r \nabla \phi \cdot \hat{n}$	V/m
pestat	electrostatic pressure	P	N/m ²

All three values are calculated only on boundary or interface faces and averaged onto the vertices using $1/r$ weighting. As a result values at vertices at the corner of the grid may differ significantly from their original face values. The electric field normal weighted by the relative permittivity uses the normal local to the face. The electrostatic pressure force is the normal force directed toward an empty domain. Thus a positive pressure pushes the face "toward" the empty domain and a negative pressure force would pull a face "away" from the empty domain

4.2.5.2 FVM Electrostatic Output

cfv-view	description	symbol	units
elpot	electrostatic potential	ϕ	V
efieldx	electric field x component	E_x	V/m
efieldy	electric field y component	E_y	V/m
efieldz	electric field z component	E_z	V/m
pestat	electrostatic pressure	P	N/m^2

All values are calculated at cell centers and averaged onto the vertices using $1/r$ weighting. As a result values at vertices at the corner of the grid may differ significantly from their original cell values. The three components of the electric field $\mathbf{E} = E_x \hat{x} + E_y \hat{y} + E_z \hat{z}$ are given as the three components of the cartesian coordinate system. At material interfaces (faces where the electric permittivity changes) the electric field is discontinuous. This is not seen in CFD-VIEW where the cell center values have been averaged onto cell vertices before output to the DTF file. Currently there is no way to assign two different values to the same vertex. The electrostatic pressure force is the normal force directed toward an empty domain. Thus a positive pressure pushes the face "toward" the empty domain and a negative pressure force would pull a face "away" from the empty domain

4.3 Prototype for Web Based Interface

An HTML-VRML based interface was developed to allow job submission to FastBEM via the Web. The user specifies as input a simple CSG model, as well as parameters relating to mesh size, problem type, and boundary conditions. The server then generates the grid, solves the problem, and returns the results to the user's browser, along with a link to the 3-D plot in VRML format. Sample results are shown in Figure 4-7 to Figure 4-10.

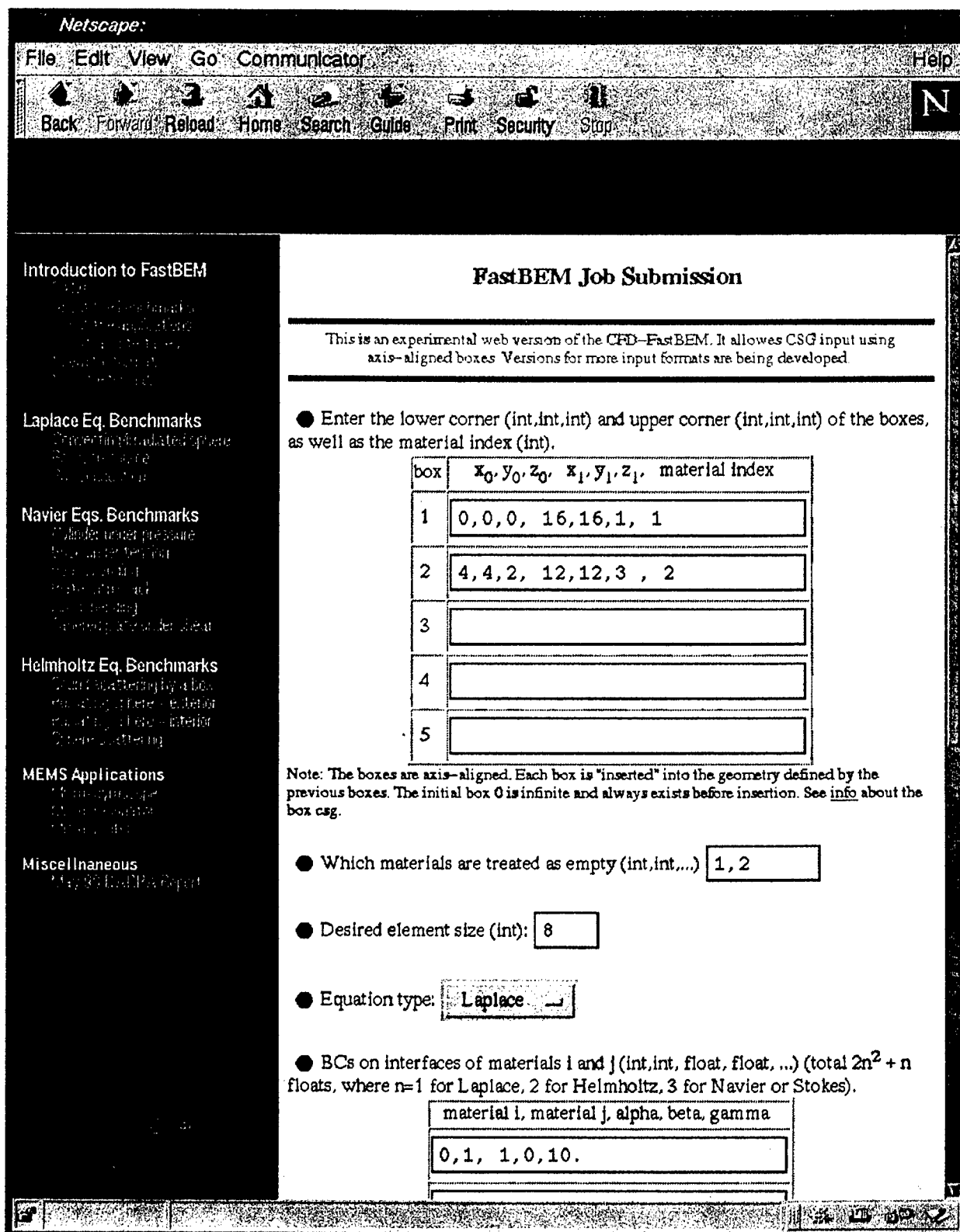


Figure 4-7. Snapshot of Upper Portion of GUI for CFD-FastBEM

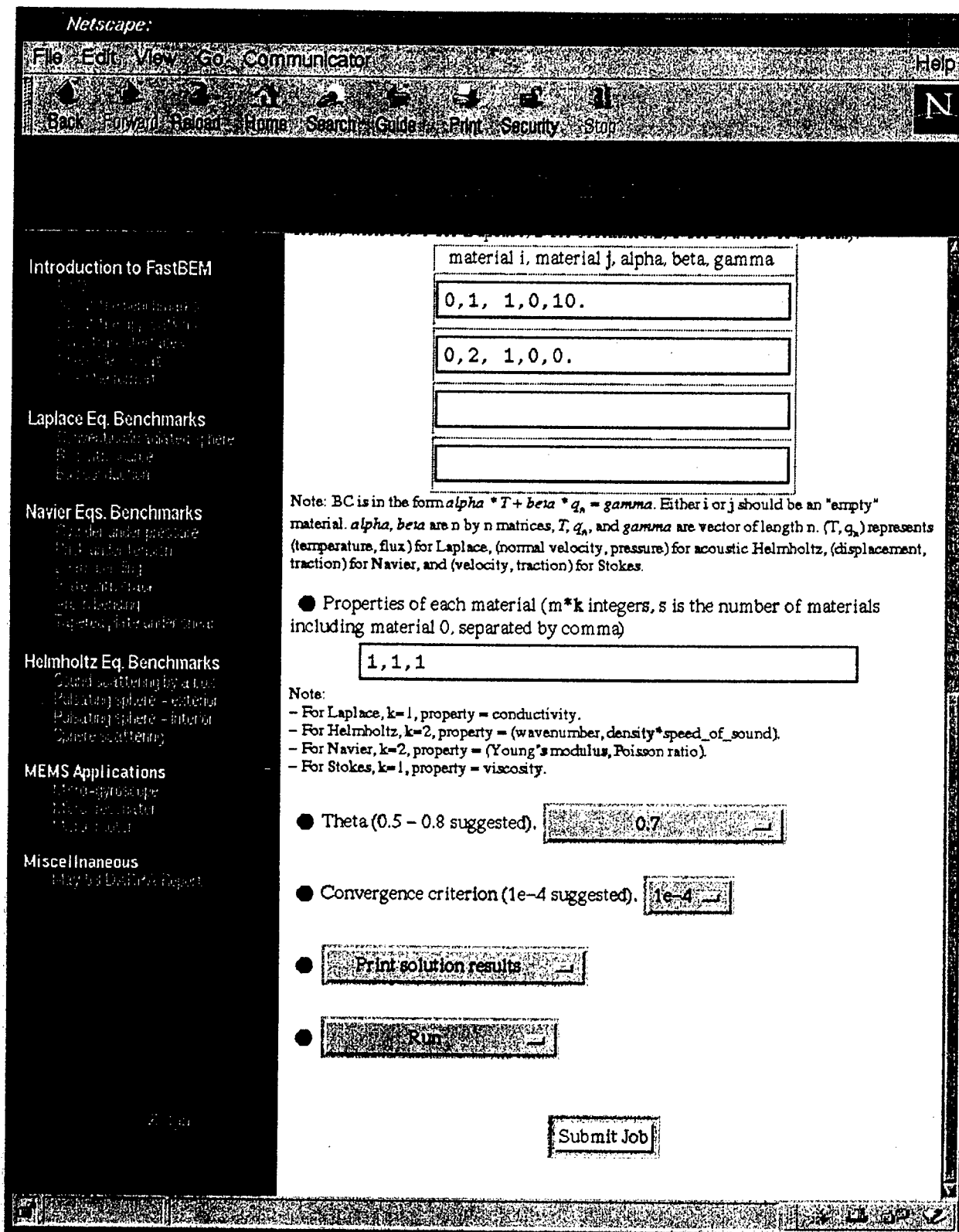


Figure 4-8. Snapshot of Lower Portion of GUI for CFD-FastBEM

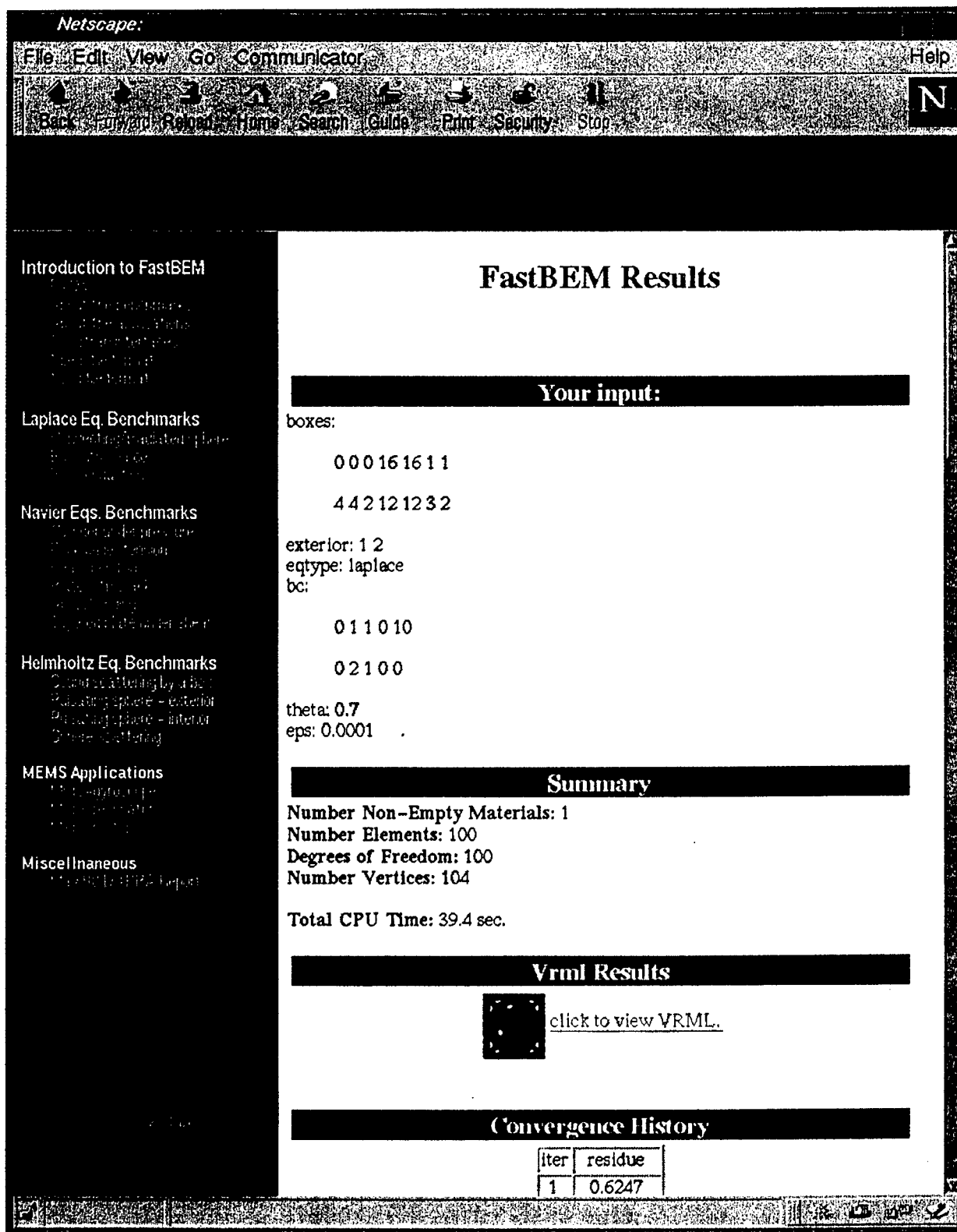


Figure 4-9. Results from On-line Execution of FastBEM

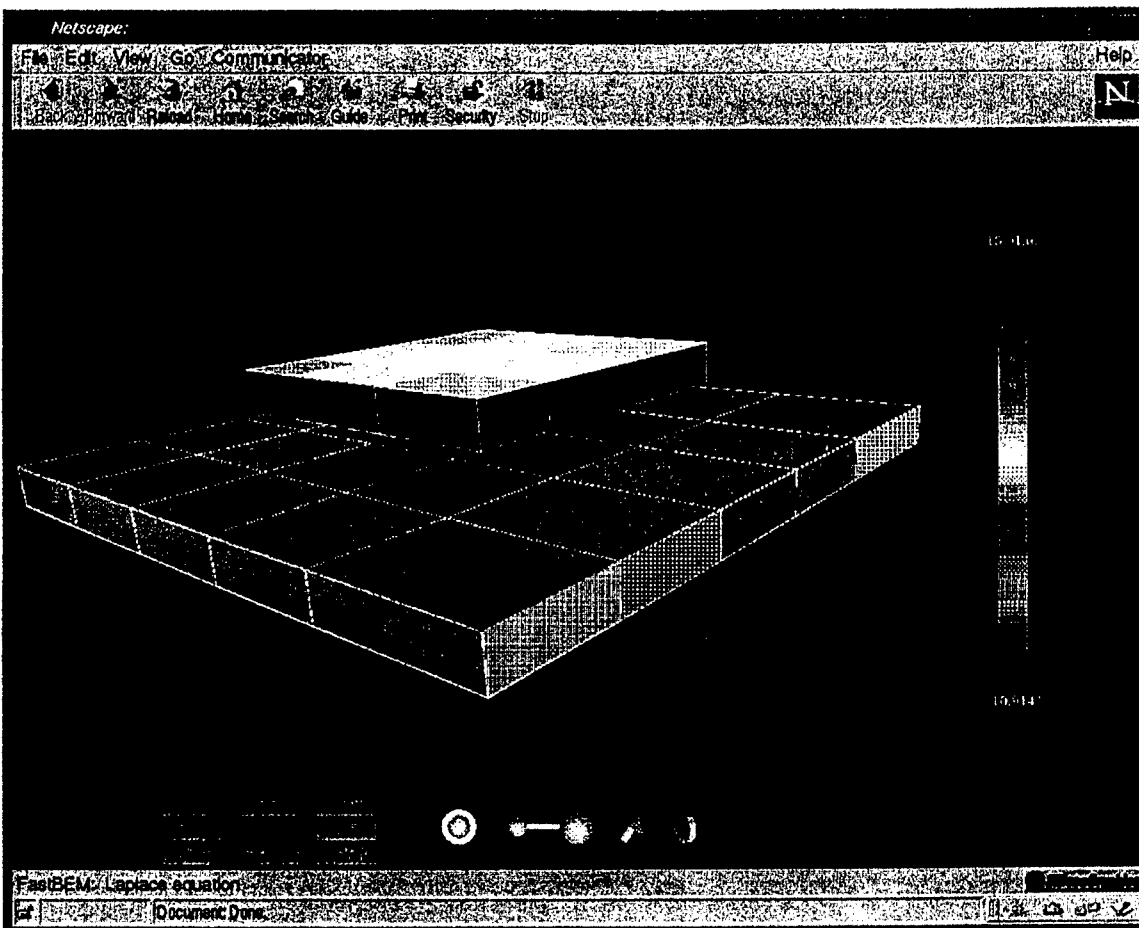


Figure 4-10. Visualization of FastBEM Results Using VRML

5. VALIDATION STUDIES AND STUDIES OF INDUSTRIAL MICROSYSTEMS

5.1 Benchmarks of BEM

In order to verify the $O(N)$ performance of the developed BEM solver several benchmarking tests were carried out for some standard problems for which analytical solutions exist.

The first problem is that of heat conduction inside a sphere which is subjected to convection and irradiation on the surface. The temperature distribution is shown in Figure 5-1. The second problem is that of a cylindrical vessel deformation under surface pressure. The displacement is shown in Figure 5-2.

Tables 5-1 and 5-2 summarize the time and memory required by BEM as a function of the number of elements, N , for the above two problems. For comparison, the performance of the conventional BEM (i.e., $\theta = 0.0$) is also included.

As the numbers in the tables show, the actual performance of the BEM solver is indeed very close to $O(N)$ for each iteration. The overall time performance is worse for the second problem ($O(N^{1.16})$ to $O(N^{1.32})$, because the number of GMRES iterations grows as N increases, but this should be expected for all linear solvers of the CG class.

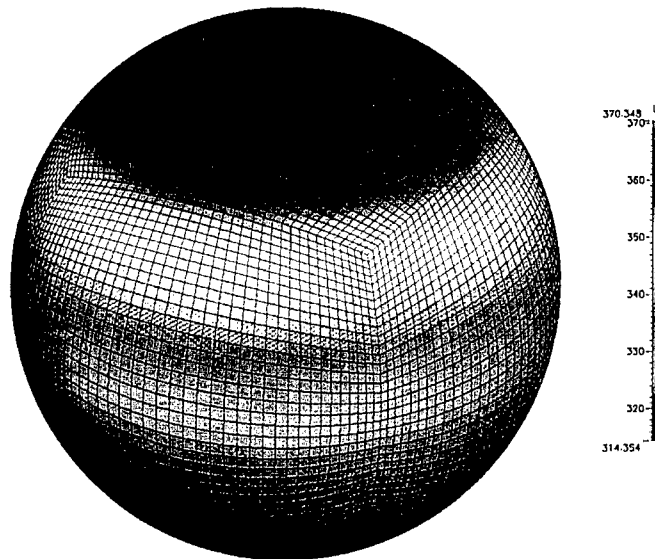


Figure 5-1. Temperature Distribution on a Sphere Subjected to Surface Irradiation and Convection

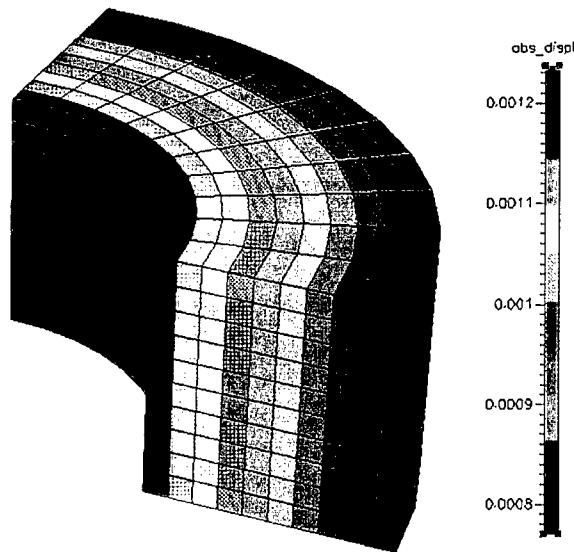


Figure 5-2. Displacement of a Cylinder Under Surface Pressure

Table 5-1. Benchmark Results for Heat Conduction Inside a Sphere

Number of faces	Conventional BEM					
	time	iter	space	time	iter	space
150	8.9s	31	1.37 MB	6.6s	3	1.5 MB
600	136s	3	12.8 MB	3.1s	3	3.20 MB
2,400	2221s	3	193 MB	133s	3	11.7 MB
9,600	9.2 hrs	(-3)	(~3000 MB)	0.153 hr	3	46.5 MB
38,400	155 hrs	(-3)	(~9000 MB)	0.642 hr	3	187 MB
Performance	O(N ²)	-	O(N ²)	O(N ²)	-	O(N ²)

Table 5-2. Benchmark Results for Deformation of a Cylinder Under Surface Pressure

Number of faces	Conventional BEM			FastBEM		
	time	iter	space	time	iter	space
150	27s	19	2.40 MB	43s	18	1.51 MB
600	466s	27	18.67 MB	757s	28	5.03 MB
2,400	6.3 hrs	43	(~550 MB)	1.37 hrs	43	17.68 MB
9,600	6.7 hrs	63	(~8700 MB)	8.20 hrs	67	67.23 MB
Performance	O(N ²)	-	O(N ²)	O(N ²)	-	O(N ²)
Performance per iteration	O(N)	-	O(N)	O(N)	-	O(N)

Additional validation of the FastBEM model was carried out on benchmark problems calculated by NASTRAN's boundary element method package, TEAM. Figure 5-3 shows a sample list of

the benchmark problems and Table 5-3 shows the comparisons of the results/performance of FastBEM and those of TEAM.

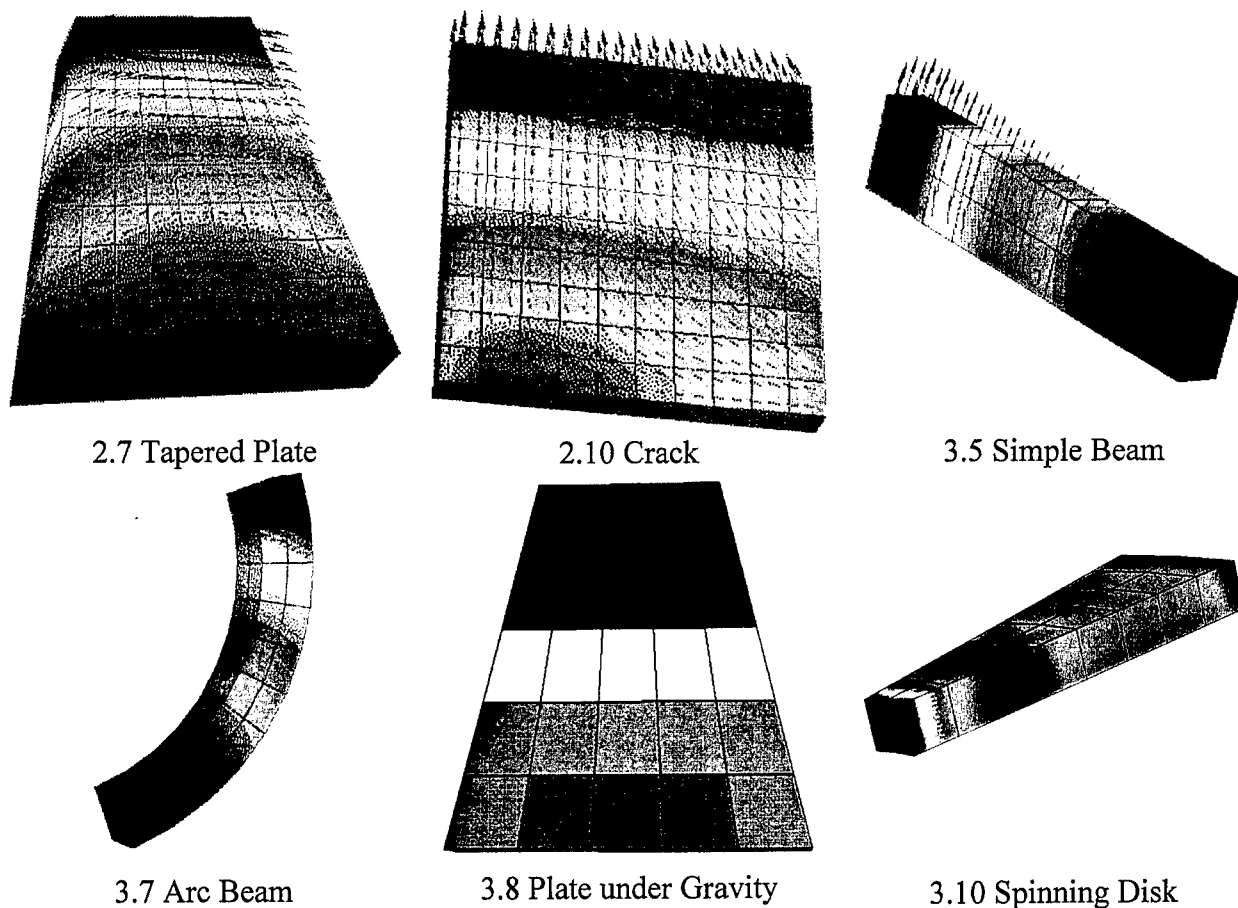


Figure 5-3. Test Cases Used by TEAM

Table 5-3. Benchmark Comparisons with TEAM

Case No.	Description	Target	TEAM	FastBEM	No. of Faces in FastBEM	Interpolation
2.7	Tapered Plate under Edge Shear	26.9 MPa	27.1 MPa	24.94 MPa	198	bilinear
2.10	Plate with a Central Crack	6.0066e-6 in	4.13e-6 in	6.2704e-6 in	240	bilinear
3.5	Simple Cantilever Beam	-0.33333e-3 in	-0.3510e-3 in	-0.32535e-3 in	64	bilinear
3.7	90° Arc Beam Bending	1.442e-3 in	1.768e-3 in 1.584e-3 in	1.927e-3 in 1.689e-3 in	48 192	bilinear
3.8	Tapered Cantilever under Gravity	-0.200 MPa	-0.200 MPa	-0.193 MPa	70	bilinear
3.10	Flat Spinning Disk	1.064e-3 in	1.066e-3 in	1.05e-3 in	208	constant

5.2 Benchmarks of FVM and BEM Applied to Electrostatics

The performance of FVM and BEM were compared when solving Poisson's equation on standard test problems. Initial testing shows FVM faster than BEM (for simple problems such as

a parallel plate capacitor) and more accurate. BEM is better at unbounded problems and problems where the cells/boundaries ratio is on the order of 1000.

5.2.1 Parallel Plates

The first benchmark is a rectangle with two different electric permittivity materials sandwiched between square parallel contacts as shown in Figure 5-4. It is a bounded problem with applied potentials of $\phi(x = d) = \phi_0$ V, $\phi(x = 0) = 0$ V. All other surfaces have zero normal potential gradient (i.e., $-\epsilon_r \nabla \phi \cdot \hat{n} = 0$).

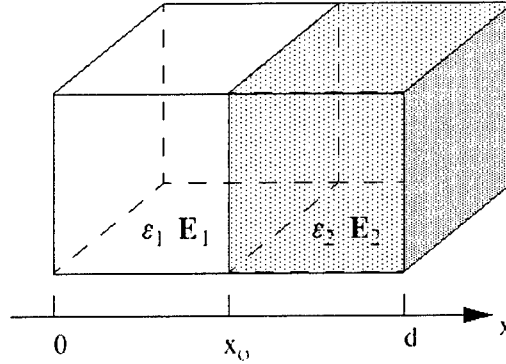


Figure 5-4. Parallel Plate Geometry

The electric potential at $x = x_0$ is

$$\phi(x_0) = \frac{\epsilon_2 x_0}{\epsilon_1 (d - x_0) + \epsilon_2 x_0} \phi_0 \quad (5.1)$$

The uniform electric fields at either side of the $x = x_0$ interface are

$$\mathbf{E}_1 = \frac{-\epsilon_2}{\epsilon_1 (d - x_0) + \epsilon_2 x_0} \phi_0 \hat{x} \quad (5.2)$$

$$\mathbf{E}_2 = \frac{-\epsilon_1}{\epsilon_1 (d - x_0) + \epsilon_2 x_0} \phi_0 \hat{x} \quad (5.3)$$

The capacitance is

$$C = \frac{A \epsilon_1 \epsilon_2}{\epsilon_1 (d - x_0) + \epsilon_2 x_0} \quad (5.4)$$

This benchmark was done on a DEC 500 with $d = 10$, $A = 25$, and $\phi_0 = 50$ V for two different cases where the permittivity of the two regions is varied. In the first case they both equal the permittivity of free space, in the second one of the regions has a permittivity four times that of free space. The electric potential at the interface, the electric field in each region, the

capacitance, memory requirements, and solution time were compared for BEM and FVM. As expected, the FVM performs much better than BEM for this case in accuracy, speed, and memory requirements. It is expected that BEM will be more approximate given that accuracy has been sacrificed to gain solution speed. The BEM predicted capacitance values are fairly close to theory which implies that on average the calculated field values at the contacts is accurate.

(1) $\epsilon_1 = \epsilon_2 = \epsilon_0$

	$\phi(x = 5)$ (V)	E_{1x} (V/m)	E_{2x} (V/m)	C (Farads)	Mem	CPU
Theory	25.00	-5.00	-5.00	2.214×10^{-11}		MM:SS
FVM	25.00	-5.00	-5.00	2.214×10^{-11}	3.5 M	00:02
BEM	24.88 to 25.17	-5.25 to -4.85	-5.25 to -4.72	2.183×10^{-11}	18.0 M	00:22

(2) $\epsilon_1 = \epsilon_0, \epsilon_2 = 4\epsilon_0$

	$\phi(x = 5)$ (V)	E_{1x} (V/m)	E_{2x} (V/m)	C (Farads)	Mem	CPU
Theory	40.00	-8.00	-2.00	3.542×10^{-11}		MM:SS
FVM	40.00	-8.00	-2.00	3.542×10^{-11}	3.6 M	00:05
BEM	40.51	-7.66 to -8.49	-1.92 to +2.12	3.332×10^{-11}	21.0 M	00:23

5.2.2 Concentric Spheres

Another benchmark case is two spheres with different radii a and b shown in Figure 5-5. Electric potentials of $\phi(r = a) = \phi_0$ V and $\phi(r = b) = 0$ V are applied to the spheres. The potential and electric field normal were calculated at the center of 25516 tetrahedra for FVM and 1128 triangle faces for BEM.

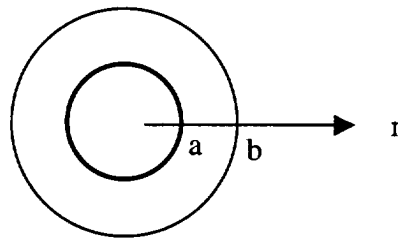


Figure 5-5. Concentric Sphere Geometry

The electric potential as a function of z is

$$\phi(z) = \frac{z}{c} \phi_0 \quad 0 \leq z \leq c \quad (5.5)$$

The uniform electric fields in the two regions are equal and are given by

$$\mathbf{E}_1 = \mathbf{E}_2 = \frac{-\phi_0}{c} \mathbf{z} \quad (5.6)$$

The capacitance of the geometry is given by

$$C = \frac{\epsilon_1 A_1 + \epsilon_2 A_2}{c} \quad (5.7)$$

DEC 500, $a = 1$, $b = 3$, $\phi_0 = 60$ V, $\epsilon = \epsilon_0$

	$\phi(x = 2)$ (V)	$E_r(r=1)$ V/m	$E_r(r=3)$ V/m	C (Farads)	Mem	CPU
Theory	15.00	90.00	10.00	1.669×10^{-10}		MM:SS
FVM	15.00	85.00	11.00	1.651×10^{-10}	16 M	00:15
BEM	n.a. [‡]	85.0 to 90.1	9.4 to 10.2	1.648×10^{-10}	51 M	00:30

[‡]BEM calculated values only for boundary faces at $r=1,3$; does not have any values at $r=2$

The values in the table are approximate due to the amount of value averaging. First there is averaging from volume center to nodes, than in CFD-VIEW where the point and line probe average from the node values. The capacitance calculation which is done internally with actual data is a good measure of how close the average electric field values are to the theory. The FVM field values are off because the cell center gradients are not being interpolated properly to the faces. The values reflect the value at cell centers near the boundary, not the value at the boundary.

5.2.3 Sphere of Space Charge

The third benchmark study of FVM and BEM is the electric potential and field due to a sphere of uniform space charge. The sphere has a uniform space charge of ρ and a radius R as shown in Figure 5.6. The total charge of the sphere is thus $Q = \rho(4/3)\pi R^3$. It is an unbounded problem with the potential at infinity assumed to be zero (i.e., $\phi(\infty) = 0.0$). For the FVM case a square with length 300 was generated around the sphere with a b.c. of $\phi = 0.0$ V at the six square sides as an artificial truncation point for the domain. In theory $\phi(r=300) = 9/300 = 0.03$ V. Applying b.c of 0.0 V at points that are actually 0.03 V introduces error. For the BEM case the unbounded problem needs no modification of the mesh. The mesh for FVM is 64996 tetrahedrals, for BEM the potential and electric field normal were calculated on 652 faces.

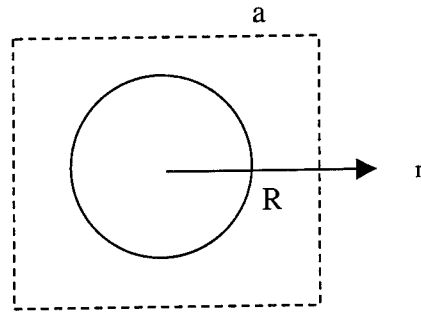


Figure 5-6. Sphere of Space Charge of Radius R in an Optional Box with Aides of Length $a > R$

The electric potential as a function of the radius r is

$$\phi(r) = \begin{cases} \frac{Q}{4\pi\epsilon_0 r} & r > R \\ \frac{Q}{8\pi\epsilon_0 R} \left(3 - \frac{r^2}{R^2} \right) & r < R \end{cases} \quad (5.8)$$

The electric fields in and out of the sphere as a function of r are given by

$$\mathbf{E}(r) = \begin{cases} \frac{Q}{4\pi\epsilon_0 r^2} \hat{r} & r > R \\ \frac{Qr}{4\pi\epsilon_0 R^3} \hat{r} & r < R \end{cases} \quad (5.9)$$

DEC 500, $R = 1$, ($a = 300$ for fvm case), $\rho = 27\epsilon_0$, $\epsilon = \epsilon_0$

	$\phi(r=3)$ (V)	$E_r(r=3)$ V/m	Mem	CPU
Theory	3.00	1.00		MM:SS
FVM	2.9	0.95 to 1.05	40 M	02:00
BEM	2.7 to 2.98	0.81 to 1.05	53 M	00:45

Neither method will be exact given that the sum of the volumes of all of the tetrahedrals making up the meshed sphere will not equal $(4/3)\pi R^3$. The FVM accuracy would increase if the bounding box were made larger. The BEM was faster than FVM and as accurate. The memory requirements are still comparable. The set-up time for the BEM was also much less than FVM.

5.3 Electrostatic Loading of Mechanical Structures

5.3.1 Doubly Clamped Beam

A typical canonical coupled electrostatics and stress problem is an elastic beam under an electrostatic load. The problem is shown in Figure 5-7. The upper $0.5 \times 10 \times 80 \mu\text{m}$ elastic beam is clamped at either end and is $0.7 \mu\text{m}$ above a rigid beam. The elastic beam has a Young's

Modulus of 1.69×10^9 Pa, Poisson's Ratio of 0.3, and no residual stress. A voltage of $\phi_0 = 10$ V or 20 V is applied to the upper beam and the lower beam is grounded (0 V). The electrostatic model calculates the electrostatic pressure force on the elastic beam. The structural model is used to calculate the stresses, strains, and displacements on the elastic beam. As seen in Figure 3-1 when 10 V is applied to the upper beam the deflection toward the rigid body is small, with a maximum displacement of $0.055 \mu\text{m}$ at beam center. With an applied voltage of 20 V the beam deforms onto the rigid body.

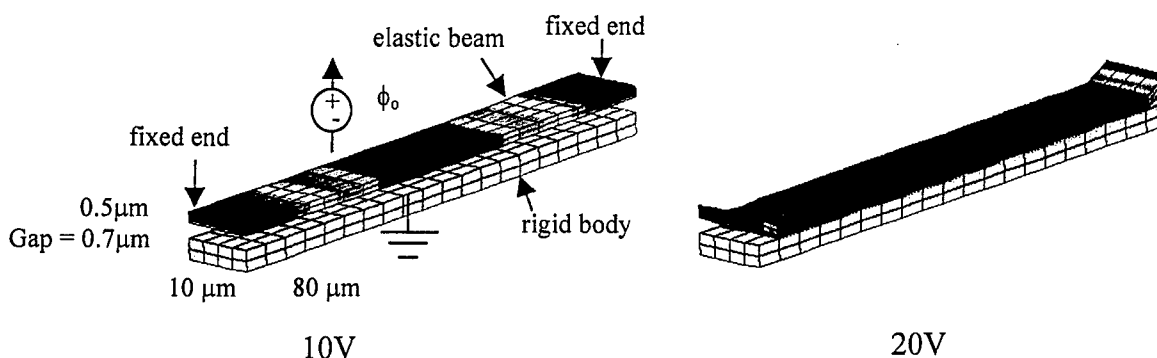


Figure 5-7. Doubly Clamped Beam Under an Electrostatic Load, with an Applied Voltage $\phi_0 = 10$ or 20 V.

5.3.2 Accelerometer

Another problem shown in Figure 5-8(a) is an electrostatically loaded plate. This is an example of an accelerometer. A large plate with an applied voltage of 20 V is clamped by four beams. The whole upper elastic structure has a Young's Modulus of 1.69×10^9 Pa, Poisson's Ratio of 0.3, and no residual stress. The upper plate is $2.0 \mu\text{m}$ above a ground plane. Figure 5-8(b) shows the calculated displacement contours on the upper plate due to the electrostatic load. With 20 V applied to the upper plate a maximum deflection in the center of the plate of $1.83 \mu\text{m}$ toward the ground plane is calculated.

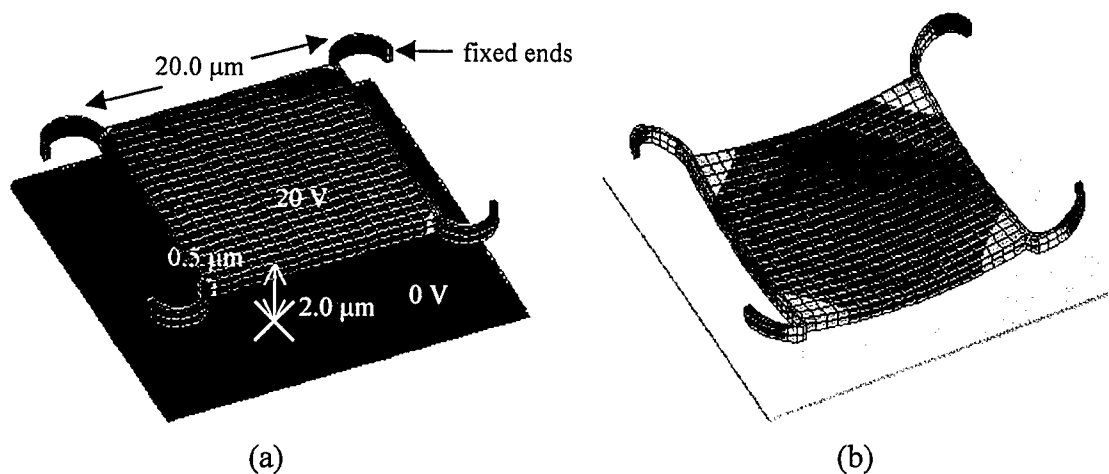


Figure 5-8. Accelerometer Under an Electrostatic Load. (a) The geometric dimensions and problem set-up. (b) The calculated displacement of the plate due to the electrostatic

load. The displacement of the plate toward the ground plane is maximum ($1.83\text{ }\mu\text{m}$) at the center of the upper plate.

5.3.3 High Frequency Resonator

Electrostatic (BEM)/structural mechanics coupling was demonstrated on a high frequency resonator shown below and used for applications such as high pass filters. A sinusoidal driving voltage is applied to a plate below a resonator beam. An electrostatic pressure force deforms the resonator beam as seen in Figure 5-9. The deformation is coupled through a "coupling beam" to an "output beam" where the change in capacitance between the beam and the ground is used to detect its deformation. The contours show the calculated vertical displacement for one instance in time.

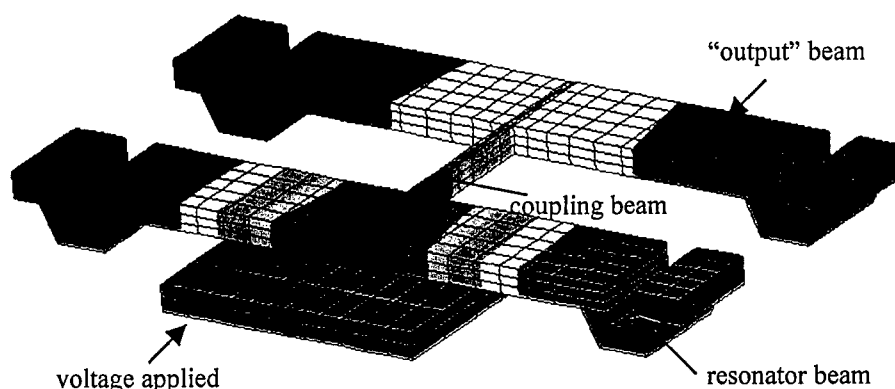
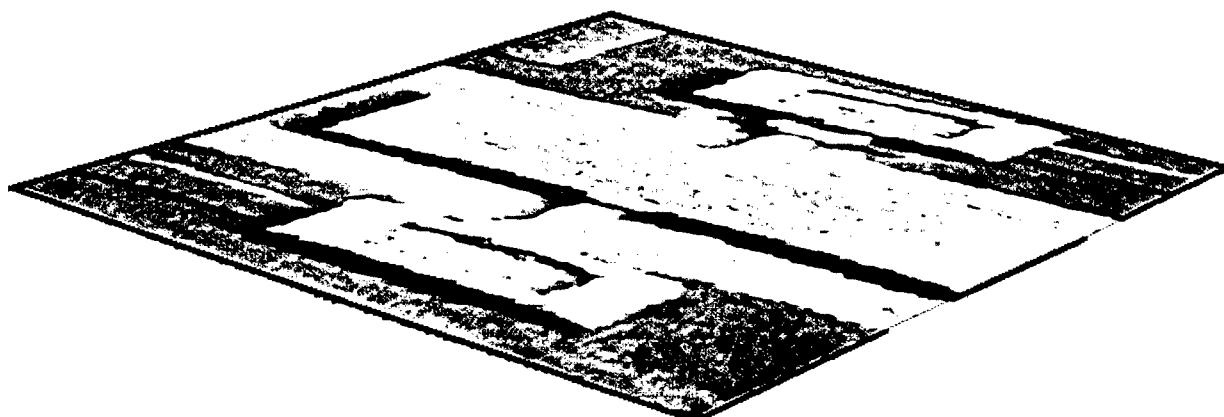


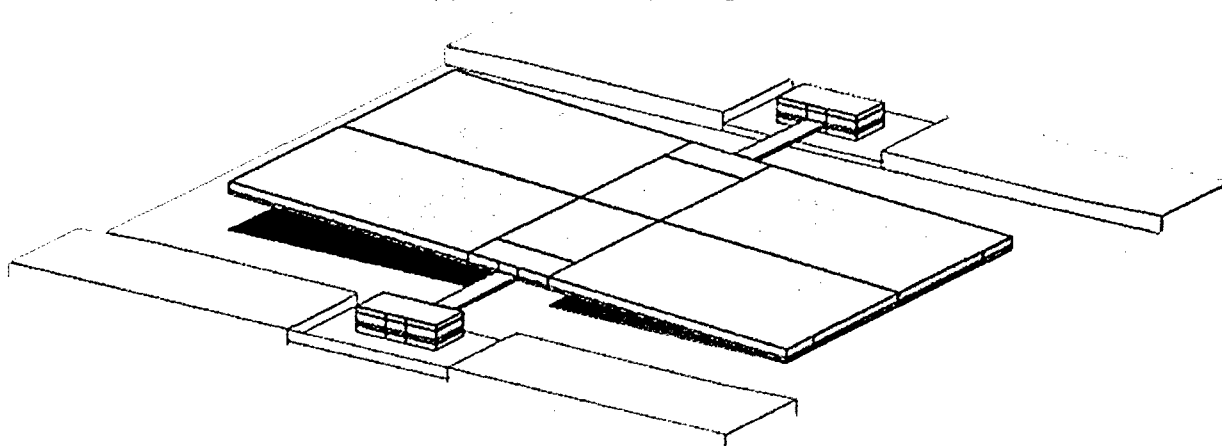
Figure 5-9. Displacement Field Contours on a High Frequency Resonator

5.3.4 Electrostatic Torsional Micromirror

Electrostatic torsional micro-mirrors are employed to serve as light modulators in devices such as printers, scanners etc. The commonly used configuration consists of a flat plate made of aluminum or polysilicon that is suspended above a ground plane by flexible hinges. Here, an aluminum mirror of dimensions $70 \times 40 \times 1.3\text{ }\mu\text{m}$ (length x width x thickness) was chosen for analysis. The torsion hinges are of dimensions $15 \times 2.5 \times 0.3\text{ }\mu\text{m}$. The plate is suspended $2\text{ }\mu\text{m}$ above a ground plane with embedded driver electrodes that are alternately made electrically active. A range of voltages from 0 to 10 V have been analyzed using the FVM/FEM coupled approach. The torsion hinge was modeled as a torsion bar with a specified spring constant designed to describe the mechanics of the mirror as that under a solid body rotation due to an applied moment. Only one half of the mirror was simulated exploiting the symmetry in the problem. In the analysis, the standard far-field and symmetry boundary conditions were specified at appropriate locations. The markedly disparate aspect ratios in the problem are an excellent test of the robustness of the employed approach. The coupled approach was able to handle this issue very well without any stability or convergence problems. Figure 5-10(a) shows a SEM picture of an aluminum micro-mirror based upon which the present geometry was roughly modeled. Figure 5-10(b) shows the mirror, which is grounded, in a deflected position due to one of the two address electrodes being made active at 10 V.



(a) micromirror (SEM picture)



(b) computed electrostatic deflection

Figure 5-10. Computational Results for an Electrostatic Micromirror

5.3.5 Micromotor Torque Curve Extraction

The geometry and boundary element grid of a micromotor device is shown in Figure 5-11. The radius of the rotor blades is 50 mm, and the gap between rotor and stator is 1.5 mm. The four blades of the stator have a potential of 9.5 V, the other components are grounded. All parts are conductors. In generating the grid, care was taken to ensure sufficient number of elements near the gaps. The BEM solver was used to compute the normal electric field on the surface, which is used in turn to compute the surface pressure. The pressure is then used to obtain the torque. The computations were performed for different rotor angles. The final torque-angle relationship is shown in Figure 5-12. The result is in close agreement with the Finite Element calculations of Barba et al., 1994.

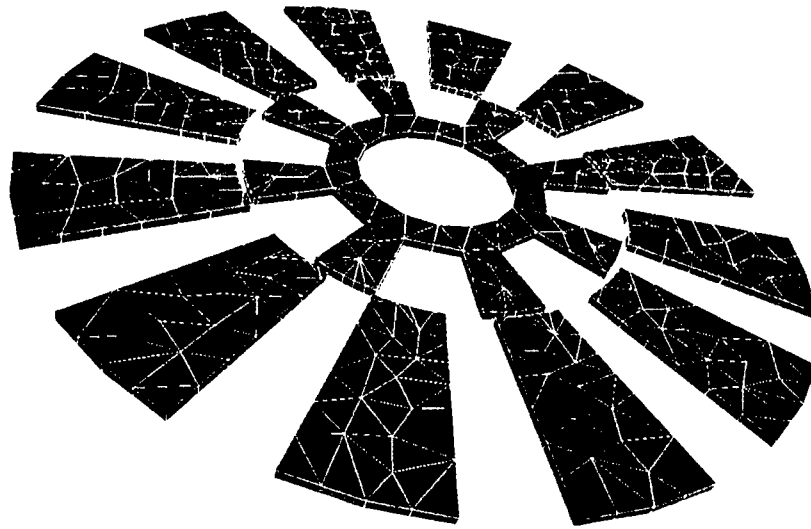


Figure 5-11. Geometry and Computational Grid for an Electric Micromotor

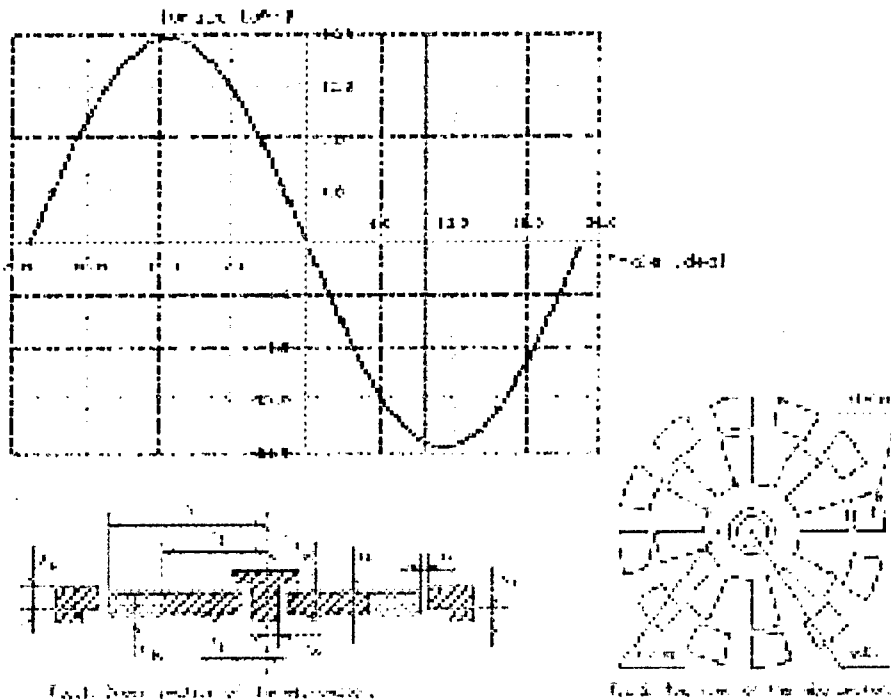


Figure 5-12. Computed Torque-Angle Relationship for the Micromotor

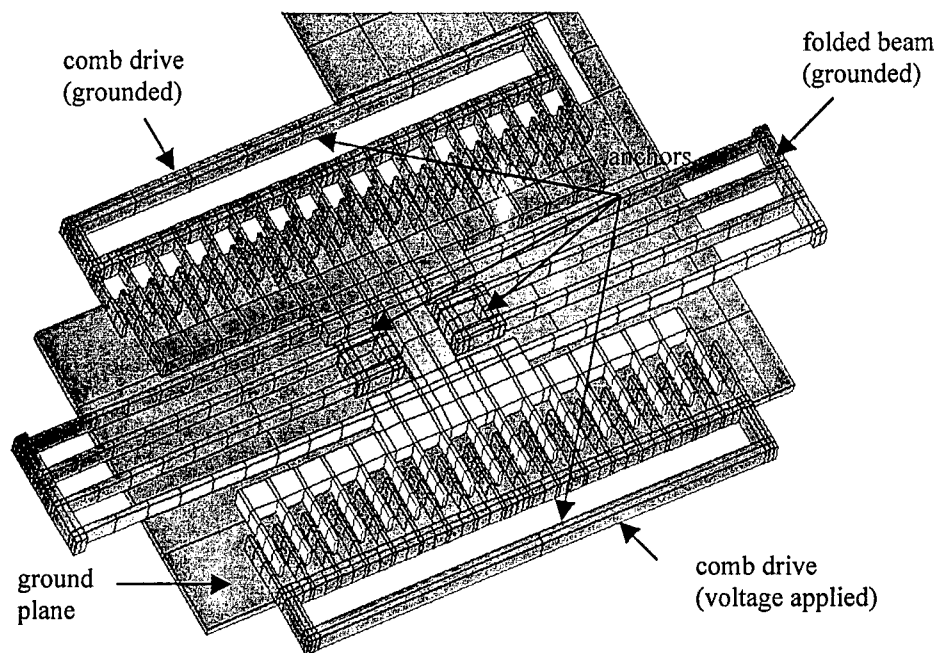
5.3.6 Linear Lateral Resonator Comb Drive

The electrostatic and structural models were tested on a linear lateral resonator comb drive (Tang et al., 1992) shown in Figure 5-13. The device has the potential for many uses such as an accelerometer or gyroscope. A folded beam with attached combs is placed between comb drives. The comb drives have applied ac or dc voltages to drive or sense the resonance of the moving

folded beam structure. The sensing circuitry takes advantage of the change in capacitance of the structure as it moves.

A calculation was performed on the linear lateral resonator comb drive shown in Figure 5-13. For this calculation, one of the comb drives is grounded and to the other a sinusoidal drive voltage is applied. The ground plane and the folded beam structure are also grounded. The folded beam is only fixed at two anchor points in the center of the structure. The beam's modulus of elasticity is 1.69×10^{11} Pa with a Poisson's Ratio of 0.3.

As the voltage increases at the driven comb drive an electrostatic pressure force pulls together the comb drive and the comb on the folded beam structure. The electrostatic pressure force also pulls the folded beam structure nearest it upwards away from the ground plane due to the electric field asymmetry introduced by the ground plane. This can be seen in Figure 5-13 which shows the structure at two instances in time. The plotted contours represent the vertical displacement (displacement normal to the ground plane). The contours show the resultant increase in tilt due to the electric field asymmetry in the vertical direction as the voltage is increased.



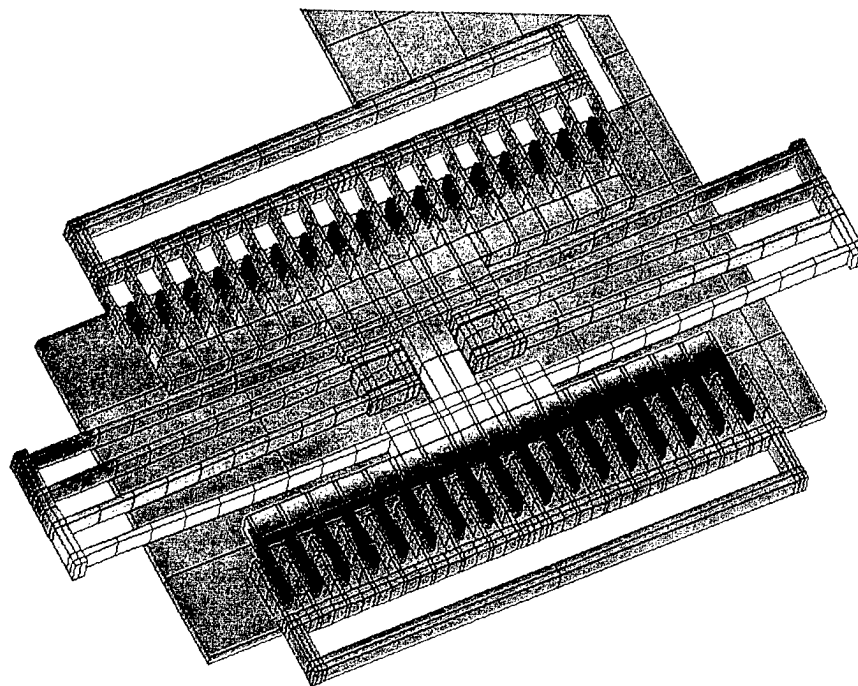


Figure 5-13. Linear Lateral Resonator Comb Drive with an Applied Sinusoidal Drive Voltage at Two Instances in Time

5.4 Fluid Damped Beam Under an Electrostatic Load

The coupled thermal-fluid-structural-electrostatic capability in CFD-ACE+MEMS was tested on a simple demonstration problem. The problem setup is shown in Figure 5-14. The geometry consists of a closed chamber, 5 mm high and 70 mm long, which contains a compressible gas of viscosity equal to 0.0171 Pa-s at an initial pressure $P_0 = 10$ Pa and temperature $T_0 = 300$ K. The chamber is bounded at the top by a flexible beam clamped at each edge, and by adiabatic walls on the other three sides. The beam is 1 mm thick, and has a modulus of elasticity of 4000 Pa. From symmetry considerations, half of the geometry is modeled, with symmetry conditions applied to the left edge.

A sinusoidal voltage is applied ($12000 \sin 5\pi t$ V) to the bottom wall, and the beam on top of the chamber is grounded. The sinusoidal varying electrostatic force deflects the beam downward compressing the gas. As the gas is compressed, the pressure increases, applying an upward force to the beam to counteract the electrostatic force. At each time step the resulting deformation is obtained from a balance of the electrostatic, pressure, and inertial forces.

The result of the analysis was to determine the transient response of the fluid pressure, temperature, electrostatic field, and the deflection and stresses of the beam. To accomplish this, the governing equations for the four models (flow, heat, electrostatic, and structural analysis) are coupled and solved implicitly at each time step. The time sequence of Figure 5-14 shows the deflection of the beam, the gas flow as vectors, and the normal axial stress as contours on the

beam. The snapshots were taken before, at, and after the voltage maximum. As the beam moves downward the gas is forced into the clamped corner pushing the elastic beam upward. The energy equation was also solved but the temperature increases were minimal (only 0.1 K) due to the small number of cycles simulated.

A parametric study was performed by varying the initial gas pressures. The graph of Figure 5-15 shows the center beam displacement for three different initial gas pressures and the lower wall voltage versus time. The beam displacement maximum is reduced with increasing initial gas pressure P_0 as the increasing gas pressure counteracts the electrostatic pressure applied to the beam. Also, the higher the initial pressure, the later the time the beam reaches its maximum displacement. This is indicative of the strong nonlinear coupling between the different models.

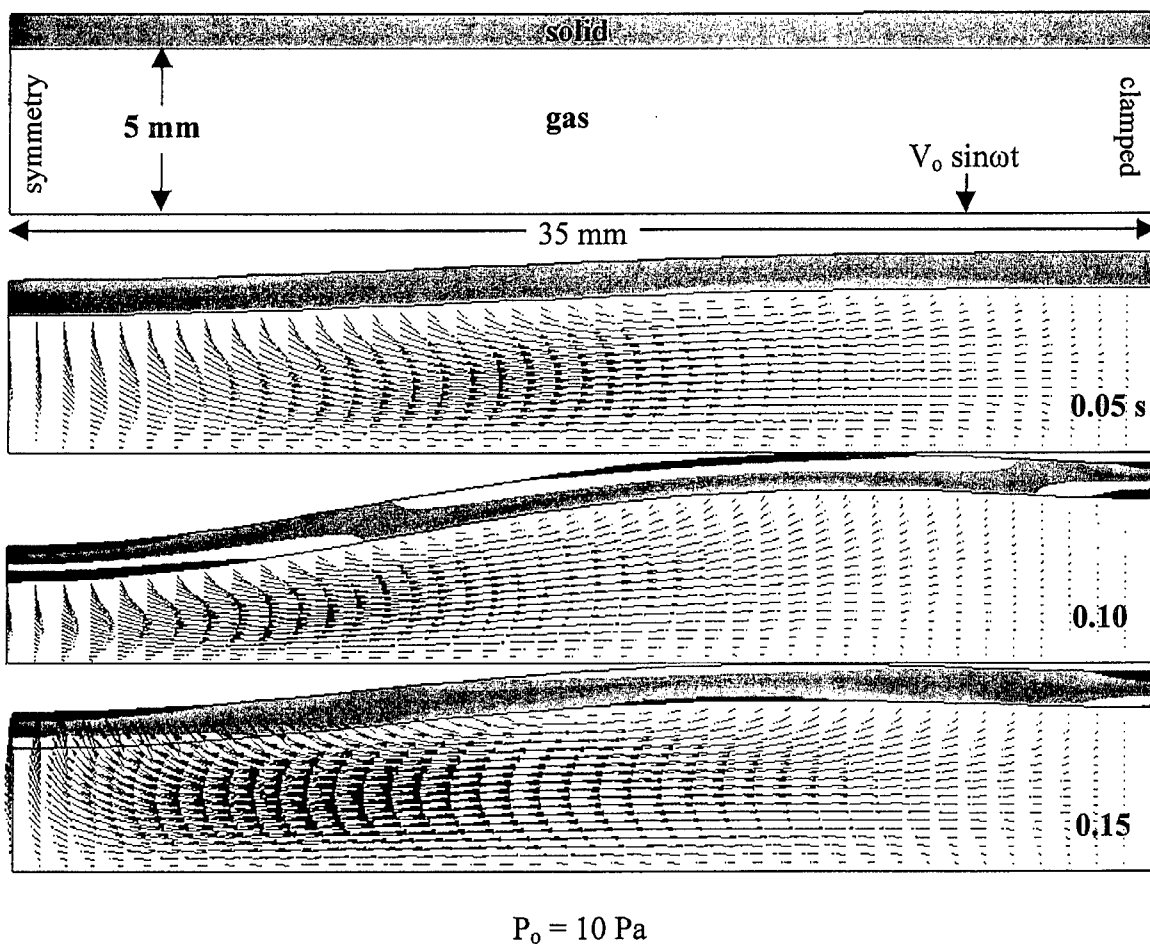


Figure 5-14. Doubly Clamped Fluid Damped Beam Under a Sinusoidal Electrostatic Load. Shown is a time sequence of the beam displacement, fluid velocity field (vectors), and normal axial stress (contours on beam) for the $P_0 = 10$ Pa case.

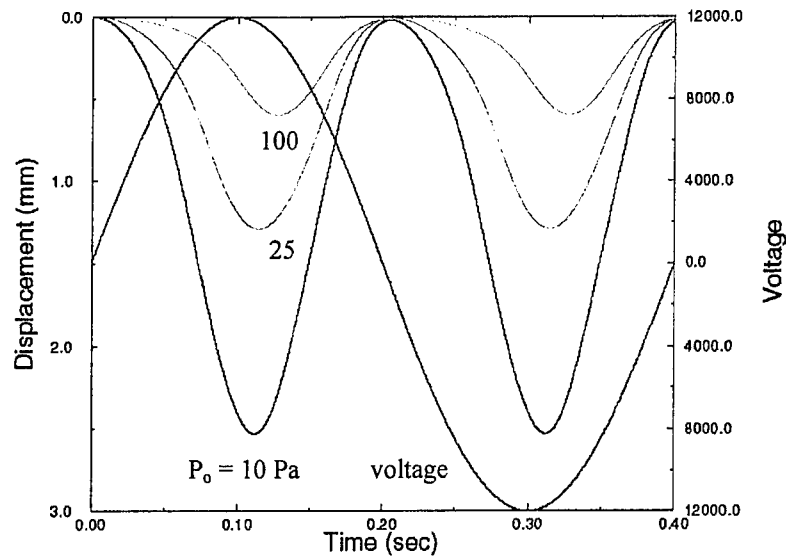


Figure 5-15. Displacement and Voltage Plots for a Doubly Clamped Fluid Damped Beam Under a Sinusoidal Electrostatic Load. Shown are the center beam displacement for different initial gas pressures (P_o) and the applied voltage on the lower chamber wall versus time.

5.5 Electrostatic/VOF Test: Electrostatic Extraction of Conductive Fluid from Bath

The geometry shown in Figure 5.16 was used to demonstrate the electrostatic extraction of a conductive fluid from a bath. The problem involves calculating gas flow, free surface flow, and electrostatics. A very large voltage is applied to the upper wall of the chamber. The lower wall and bath are grounded. The conductive fluid contained in the lower chamber contains charges on its surface due to the applied field. The pressure force on the surface of the conductive bath is resisted by the surface tension of the liquid.

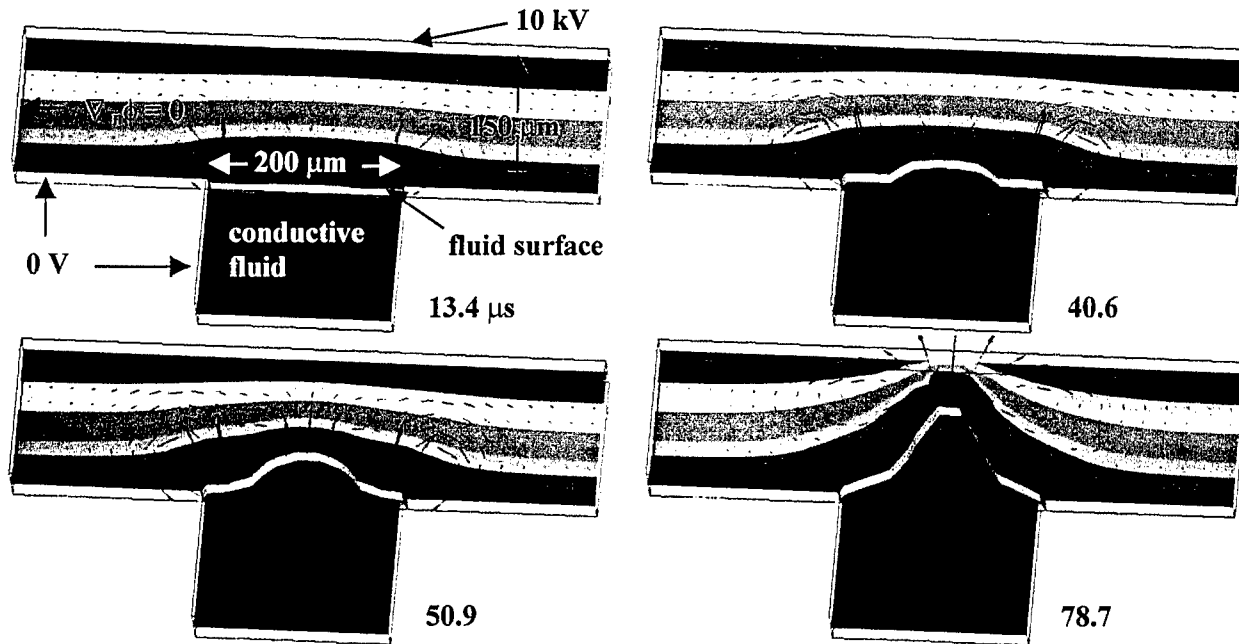


Figure 5-16. Time Evolution of the Electrostatic Extraction of a Conductive Fluid from a Bath

The free surface flows are calculated using the volume of fluid (VOF) method (Hirt et al., 1981). Briefly, the VOF method solves an additional scalar quantity F which is the volume fraction of a component in a cell. Distribution of F as a function of time and space is calculated and determines the location of the liquid cells. The main equation solved is

$$\frac{\partial F}{\partial t} + \mathbf{u} \cdot \nabla F = 0 \quad (5.10)$$

where \mathbf{u} is the flow velocity vector.

The VOF formulation includes surface tension and electrostatic pressure effects. To add the surface tension and electrostatic pressure effects, the free surface of the liquid needs to be located and then the forces applied. A conservative formulation for the surface tension forces calculation is used (Yang et al., 1998). It considers the equilibrium of a curved surface under a surface tension force. The net normal force acting on the surface is linked to the summation of all tangential forces due to surface tension. In the discrete form only the boundary lines along the surface are necessary to estimate the surface tension forces.

The results of the calculations are shown in Figure 5-16 for different time steps. The contours are the electric potential, the vectors are the fluid flow, and the surface of the liquid is represented by the grey surface. As time progresses the electrostatic pressure force on the surface of the conductive bath begins to draw the liquid from the bath toward the upper wall counteracting the surface tension forces.

5.6 Magnetic Test Cases

5.6.1 Magnetic Field Due to a Circular Current Carrying Wire

An infinitely long wire of finite radius was simulated using the magnetic model. A uniform current density in the z-direction (out of the page) of $J_z = 1/\mu_0$ A/m² was applied to the grey region (a cross-section of an infinite wire). The calculated magnetic field shown in Figure 5-17 is rotating in the counter clockwise direction as one would expect from the right-hand-rule. The calculated and analytical values for the z-component of the magnetic vector potential A_z are plotted in Figure 5-17 (one plot is for inside the wire, the other for outside the wire) and show very good agreement.

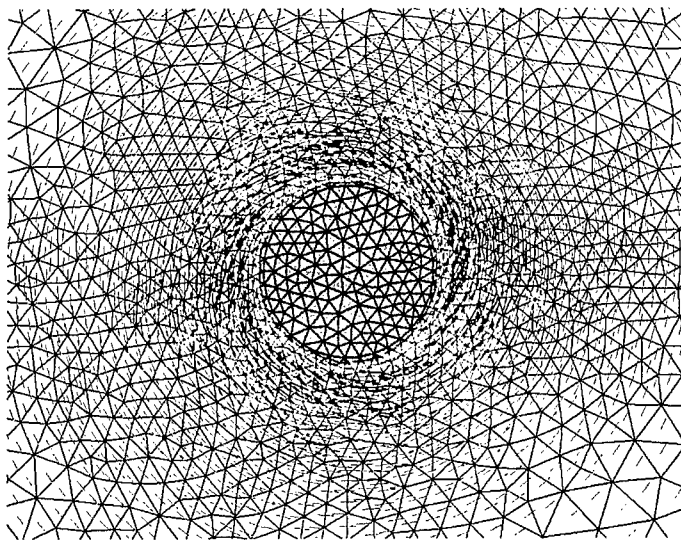


Figure 5-17. Magnetic Field Vectors Around Wire with Uniform Current

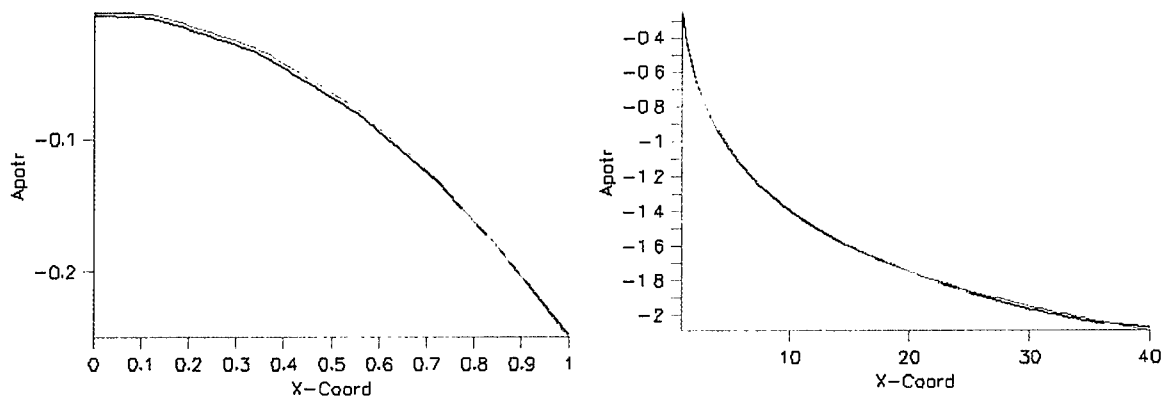


Figure 5-18. Comparison of Calculated (Red) and Analytical (Black) Solutions of Magnetic Field Due to an Infinitely Long Current Carrying Wire

5.6.2 Magnetic Field Due to Current Carrying Bus Bar at a High/Low Permeability Interface

As a validation test case of the magnetic model's multi-material capability based on the solution of the vector magnetic potential equation a benchmark numerical solution provided by Ida (1995) was simulated. This is a 2-D problem in which a current carrying conductor sets up a magnetic field that penetrates into a lower conducting material, the depth of penetration being a function of the relative permeability of the material. A very fine grid of resolution 300x100 cells was used to discretize the domain. The values used in the problem set-up are shown in Figure 5-19. The contour plot of the computed magnetic vector potential is shown in Figure 5-20. Comparison with the solution of Ida (1995), not shown here, shows excellent agreement.

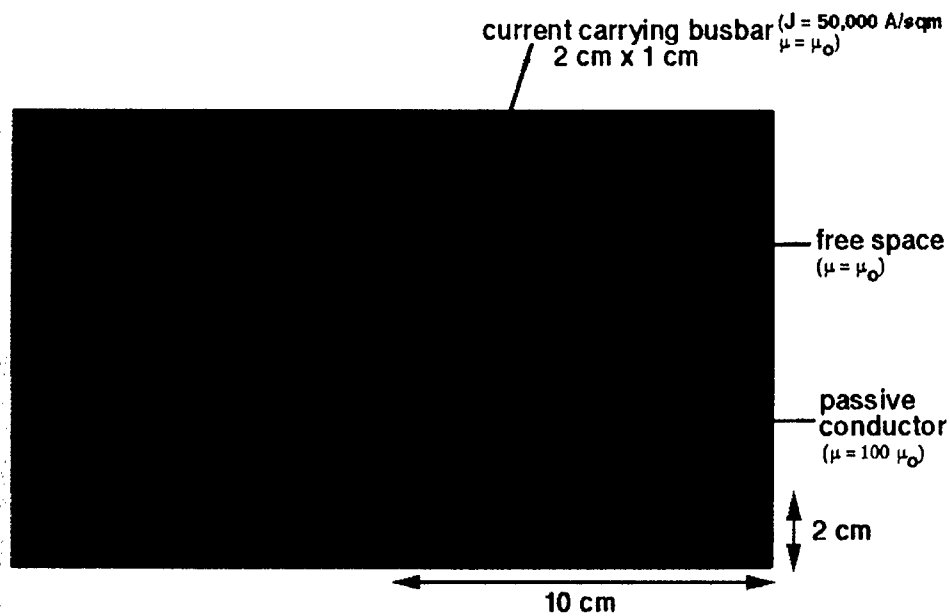


Figure 5-19. Bus Bar Test Case Specification

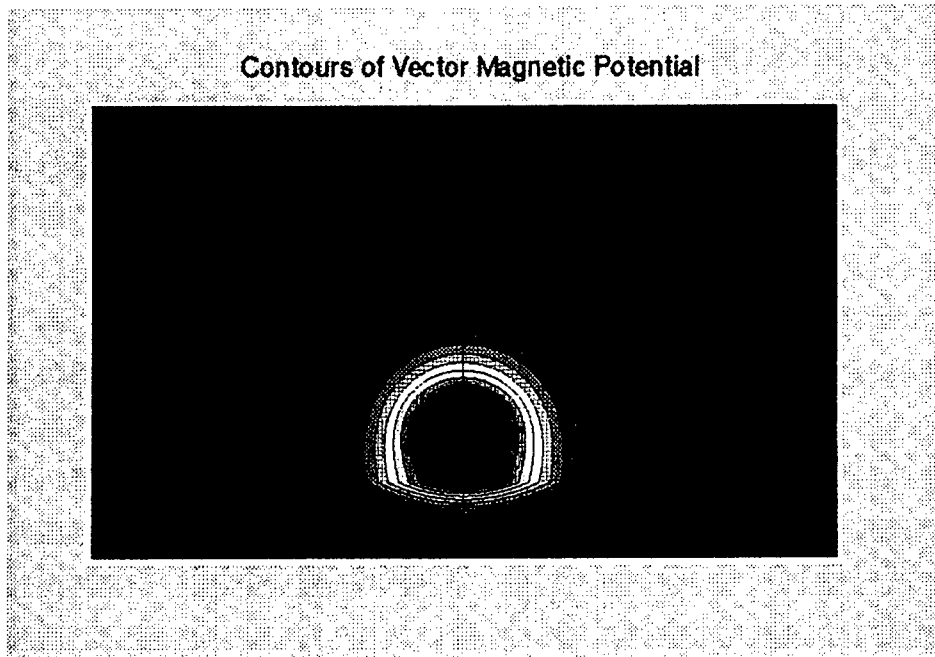


Figure 5-20. Calculated Vector Magnetic Potential Around a Bus Bar Between Materials of Different Permeability

5.7 Magnetic Field Using a Source Calculated from Electric Model

Some testing was done for the electric/magnetic link when the electric model solves the conduction equation to supply the magnetic model with a source current. This is an important link when current sources of arbitrary shape are introduced into a problem. It would be impossible for a user to specify the current source magnitude and direction in every grid cell of the source. The coupling of the two models automates the source current specification. Two different source current shapes were tested: a circular and square planar coil.

5.7.1 Magnetic Field for Spiral Conductor

The coupling between the electric and magnetic models is demonstrated by calculating the magnetic field around a spiral conductor. The terminals of the spiral are fixed at different voltages and the electric model calculates the current through the conducting material. The current is shown in Figure 5-21 as vectors colored with the value of the potential. The grid density in the conductor is too high to distinguish individual vectors in this plot. This current is used as a source in the magnetic calculation. The magnetic field vectors are shown in black in a plane perpendicular to the spiral.

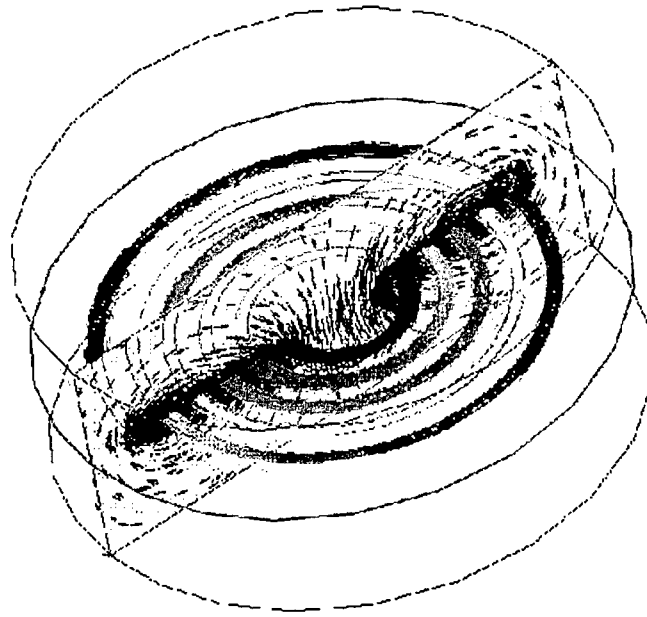


Figure 5-21. Magnetic Field Due to Current in Circular Coil

The spiral has a constant cross section, so the magnitude of the current density is a known constant value everywhere in the conductor. The direction of the current, however, depends on the path length along the spiral.

5.7.2 Magnetic Field Due to Planar Coil

The magnetic actuation of structures is of great interest due to the larger distances which a structure can be moved when compared with electrostatic actuation. The test problem, which will be used to test this capability, is the actuation of a plate due to a magnetic field generated from a planar coil.

A first step in this problem is to calculate the magnetic field generated by a planar coil. The conduction problem is solved on the coil to get a source current. The source current is then fed into the magnetic solver which calculates the magnetic field due to the current through the planar coil. Shown in Figure 5-22 is the magnetic field due to current flow in a two turn planar coil.

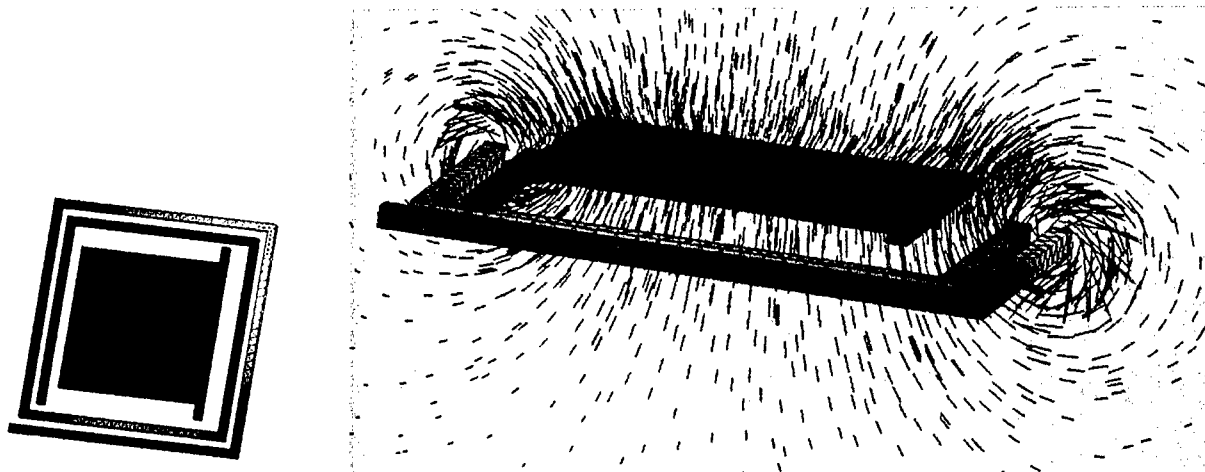


Figure 5-22. Problem of Plate Movement Due to a Magnetic Field. Shown is the (a) the electric potential in the coil and (b) the calculated magnetic field generated from the planar coil.

5.8 Magnetic Actuation of a Beam

The magnetic actuation of structures is of great interest due to the larger distances which a structure can be moved when compared with electrostatic actuation. In Figure 5-23 is a demonstration of the magnetic actuation of a beam in 2-D. The deformation of the 2-D beam was due to an induced magnetic moment of some attached magnetizable material to a beam. Initially a uniform magnetic field was applied to the structure. As the material magnetized, the magnetic field near the magnetized region underwent variation. With a non-zero magnetic moment and a non-uniform magnetic field in the region of the material a torque on the material is induced. The torque on the material actuates the beam to which the material is attached. The displacement of the beam, the magnetic field near the high permeability material, and the torque on the beam are shown in Figure 5-23.

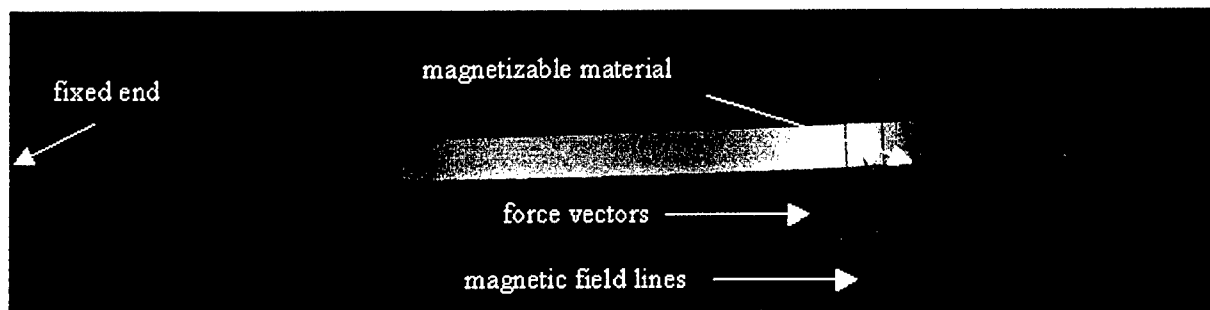


Figure 5-23. Displacement Field Contours, Magnetic Field Lines, and Force Vectors on a Magnetically Actuated Beam

5.9 Buoyancy-Driven Flow of a Conductive Fluid

The Lorentz force is demonstrated by the calculation of buoyancy driven flow of a conducting fluid in a uniform magnetic field. The bottom boundary rotates with a specified angular velocity and has a uniform temperature. The inner part of the top boundary rotates in the opposite direction of the lower boundary and has a uniform temperature lower than that of the bottom boundary. The outer part of the top boundary is a free surface. The temperature difference between the boundaries creates a buoyancy-driven flow pattern in addition to the rotation imposed by the walls. A uniform magnetic field in the opposite direction of gravity damps the flow through the Lorentz force. Figure 5-24 shows contours of the temperature and velocity in the vertical direction with and without the magnetic field. The velocity magnitude is much smaller when the magnetic field damps the flow.

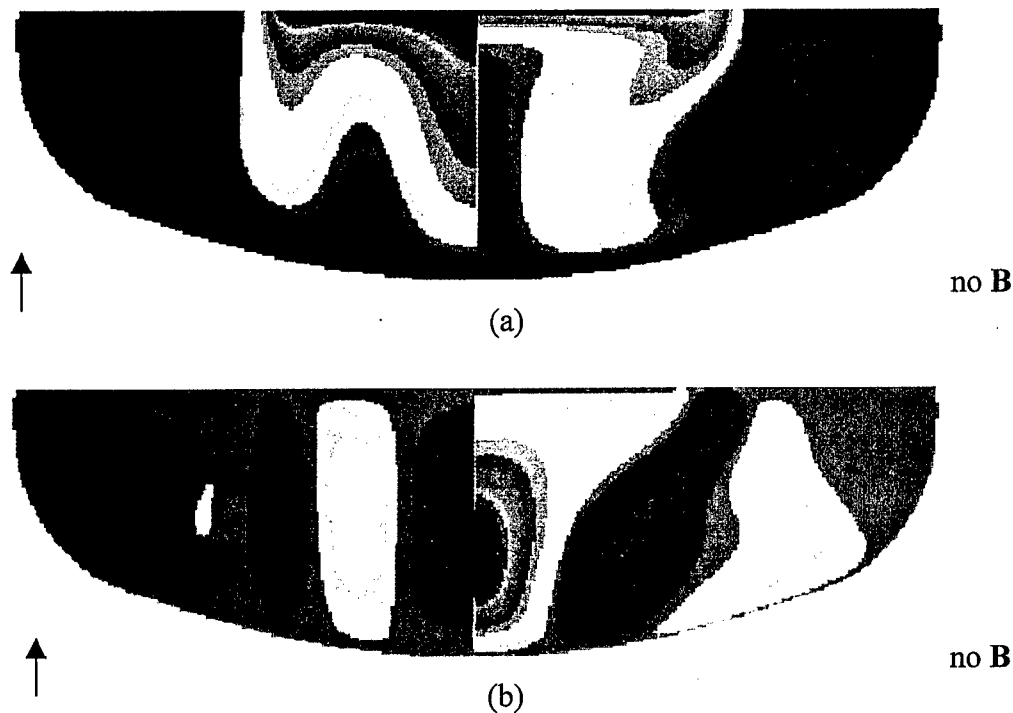


Figure 5-24. (a) Temperature and (b) Vertical Velocity Contours for Coupled Flow/Magnetics Solution. Right Half is without the Magnetic Field, Left Half is with the Magnetic Field

5.10 Electroosmosis

Electroosmosis techniques are widely used for transport of charged fluids in microfluidic systems. Shown in Fig. 5-53 is a cross channel device used for sample injection and separation. The flow of material in the device is controlled by static fields. Depending on the voltage V_s applied to the upper and lower reservoir of the cross channels, the flow of charged specie can be suppressed (0V), flowed into (37.5V), or flowed out of (135V) the cross channels.

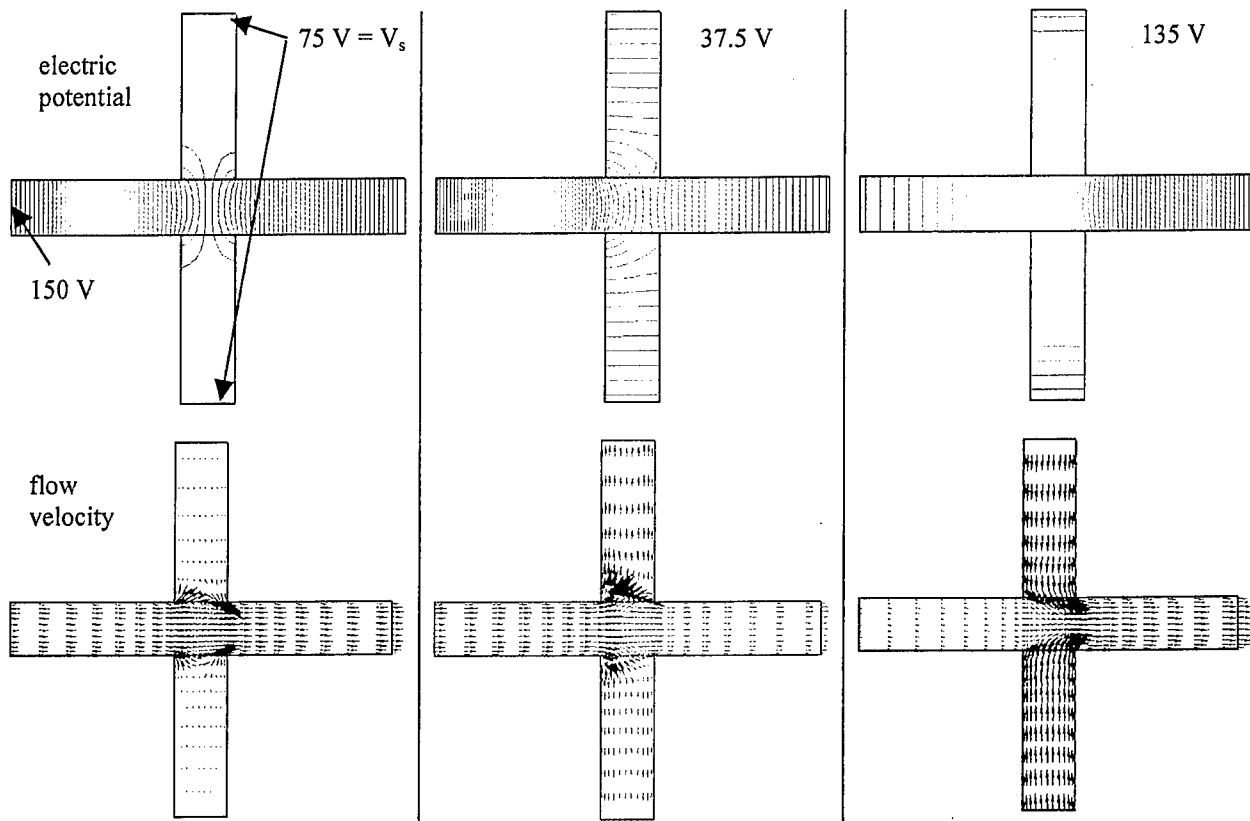


Figure 5-25. Electric Potential in Flow Velocities for a Cross Channel Device

6. ANALYSIS ON INDUSTRIAL DEVICES

The development of the MEMS CAD tool has enabled CFDRC to analyze various industrial problems and devices. The coupling of the electromagnetic model to the flow-heat-structure model has enabled the following simulations.

6.1 Xerox Flap Valve

Xerox was concerned with the voltage required to close the flap on a pressurized valve. The results are shown in Fig. 6-1 for four different applied voltages. The structural element is a flap over a flow inlet that is fixed at the left. With no flow or applied voltage, the flap lays over the inlet. At 0V with a flow, the flap is deformed, allowing flow through the system. An electric potential difference is applied between the flap and the lower right plate. A voltage which closes the flap, despite the flow, is determined.

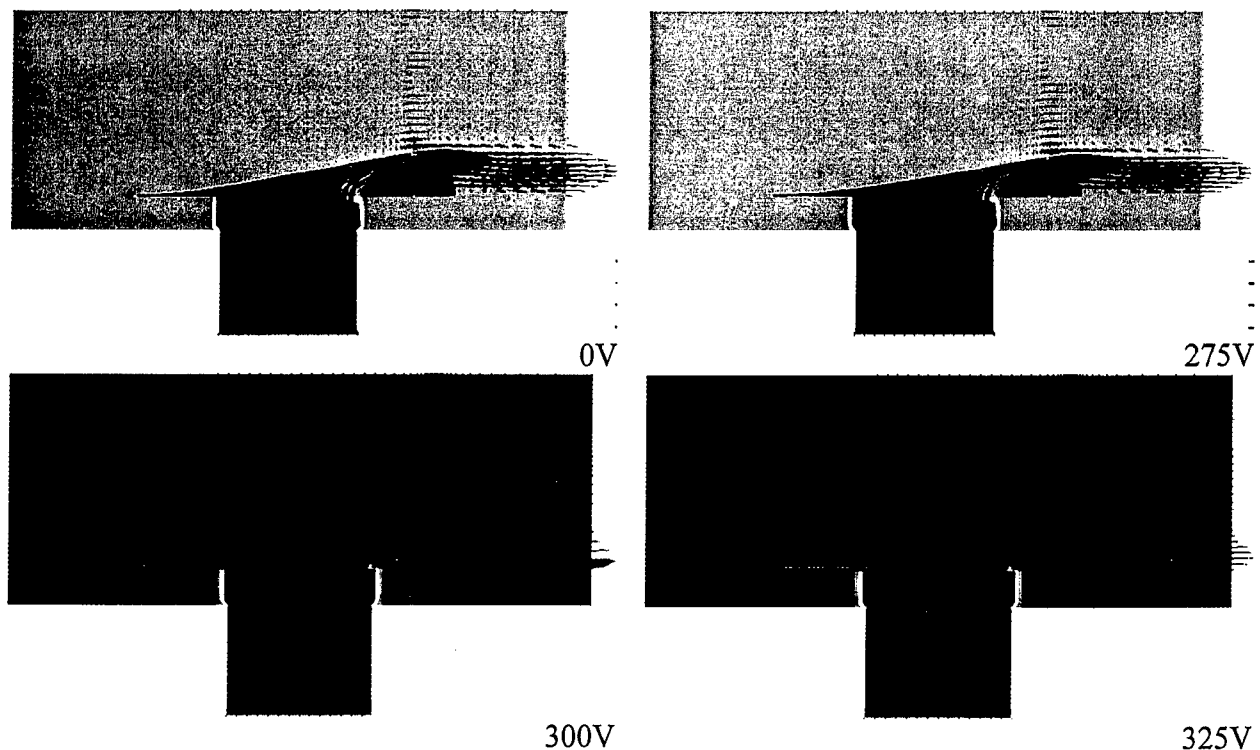


Figure 6-1. Flow Across a Flap with Different Applied Voltages

6.2 Honeywell Mesopump

Honeywell is developing a mesopump for microsystem applications (Fig. 6-2). Specific pump design parameters such as actuation voltages, actuation times, and volumetric efficiencies were of primary interest to Honeywell pump designers. The pump actuation is accomplished through electrostatic pressure forces. This was a flow/structural/electrostatic problem. Computational results such as valve closure times, membrane dynamics, and pumping rate agreed well with

experiments conducted at Honeywell (see Fig. 6-3). An example of calculated electric fields is shown in Fig. 6-4.

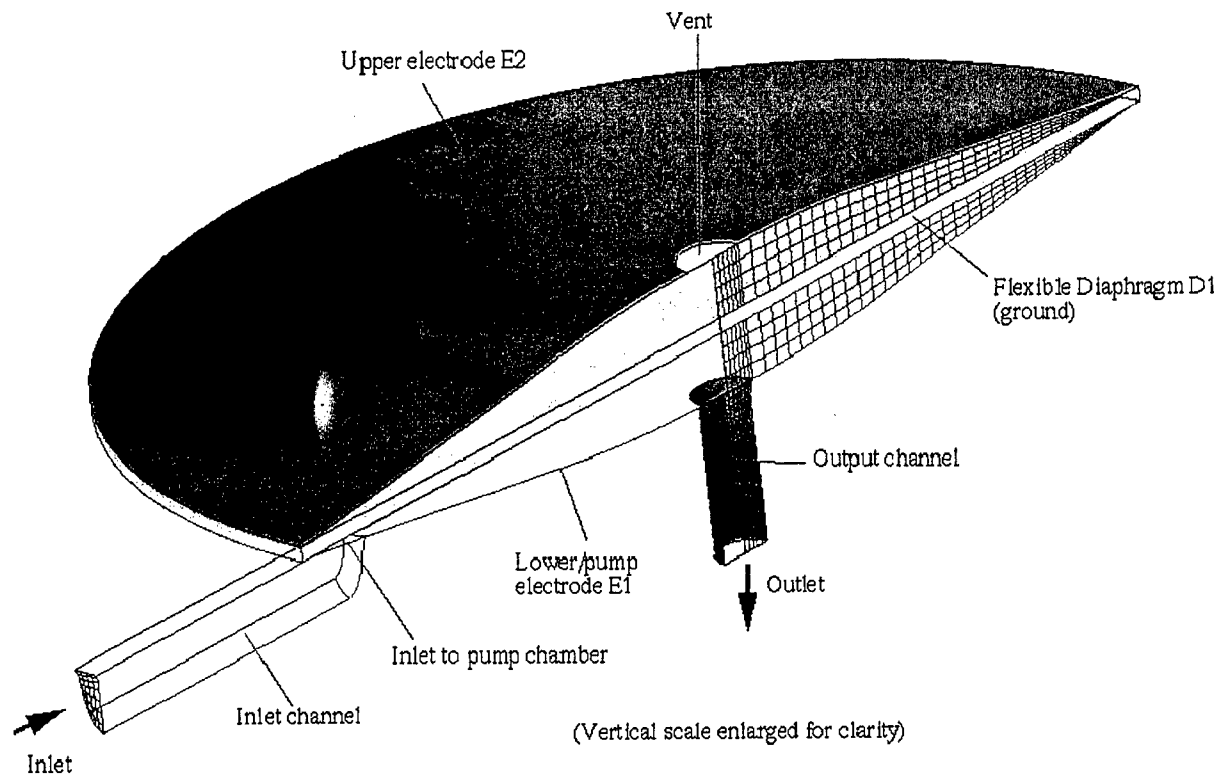


Figure 6-2. Solids Model of a Mesopump Cell with Boundary and Physical Conditions

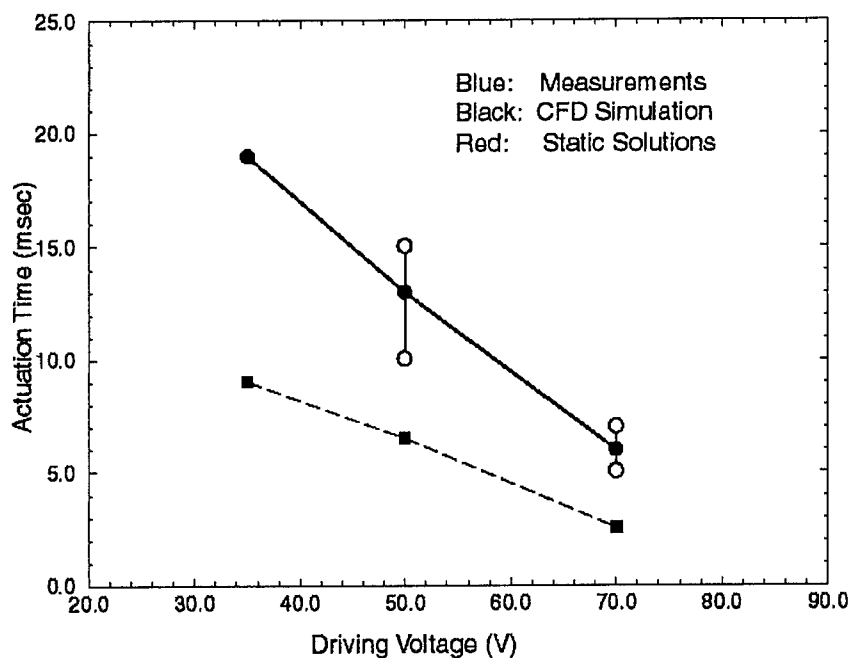


Figure 6-3. Comparison of Calculated and Measured Actuation Times of Pump for Different Driving Voltages

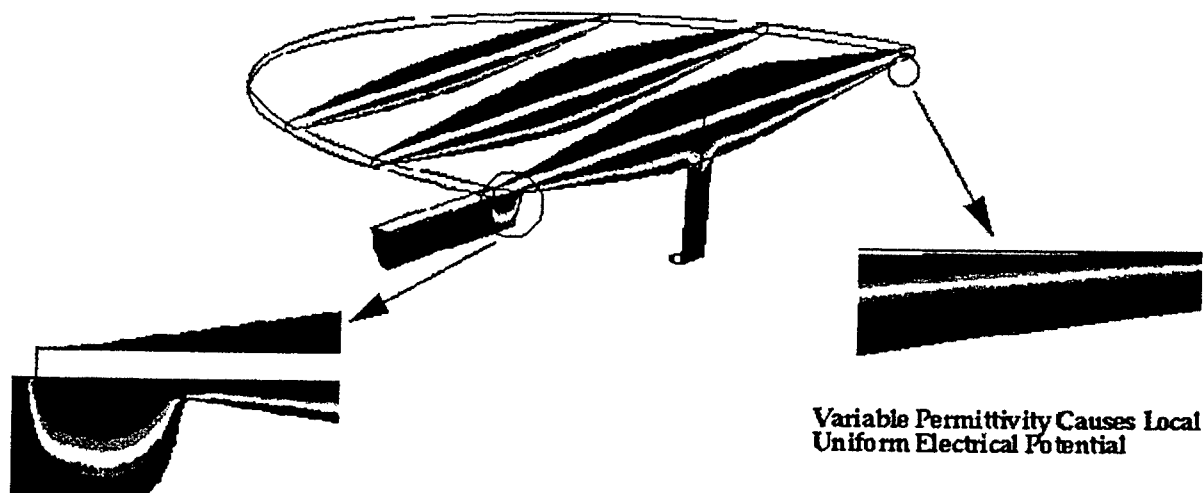


Figure 6-4. Electrostatic Field Distribution in Pump

6.3 Honeywell Cantilever Beam

This test case is an analysis of a polymer cantilever beam. The geometry for this device is shown in Figure 6-5. A kapton sheet with a thickness of 25 microns is electrostatically attracted toward a dielectric coated ground plane. The thickness of the dielectric is 0.2 micron. In an unstressed state, the kapton sheet lies flat on the dielectric substrate. An upward directed force is applied to the kapton sheet, over a length denoted as L in the figure, to raise it to a specified height h (typically 20 to 100 microns).

The kapton sheet is clamped on both the right and left edges, and thus nonlinear structural effects are important as stress-stiffening effects become non-negligible. In this analysis, the dielectric and ground planes were assumed rigid, and the rigid contact formulation was used to model the contact between the kapton sheet and the dielectric.

The purpose of the analysis is to determine the force required to raise the sheet for a specified voltage and gap height. This problem exhibits an interesting nonlinear effect. From a structural standpoint alone, more force is required to lift the sheet to a higher gap height, but a smaller gap height will require a larger force to overcome the electrostatic attraction. Consequently, depending on the structural properties and the applied voltages, there is a possibility of a local maxima in the required force for different gap heights, as opposed to a monotonically increasing force vs. gap height curve.

Figure 6-6 shows results for gap heights of 20 and 60 micron, with an applied voltage of 80 V in each case. Shown on each plot are stress contours in the kapton sheet and the electric field through the gap, dielectric, and ground plane. Figure 6-7 shows plots of the required force per unit area for the case of zero and 80 V. A local maxima is seen in the 80V curve between a gap height of 20 and 25 micron. After approximately 50 microns the electrostatic attraction becomes negligible and the two curves are nearly identical.

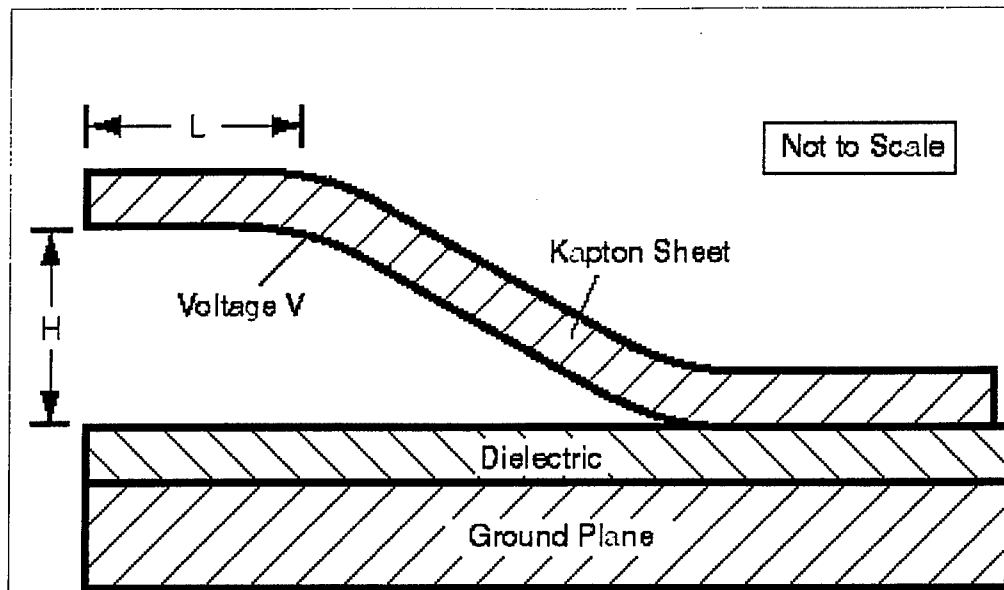


Figure 6-5. Schematic of Electrostatic Actuator

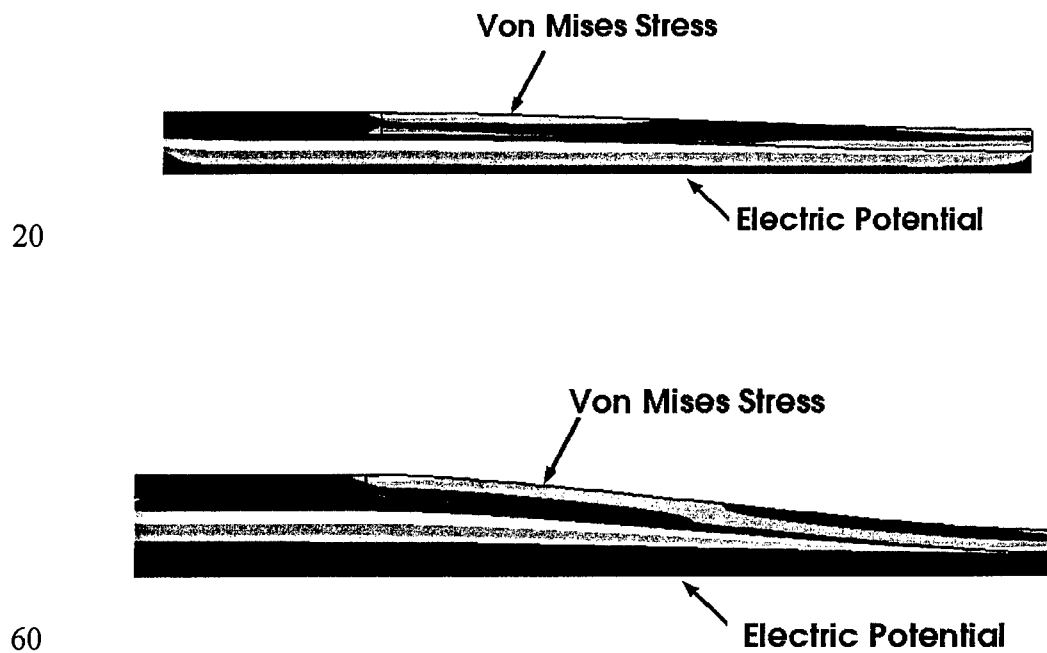


Figure 6-6. Computational Results for $h = 20\mu$ and $h = 60\mu$

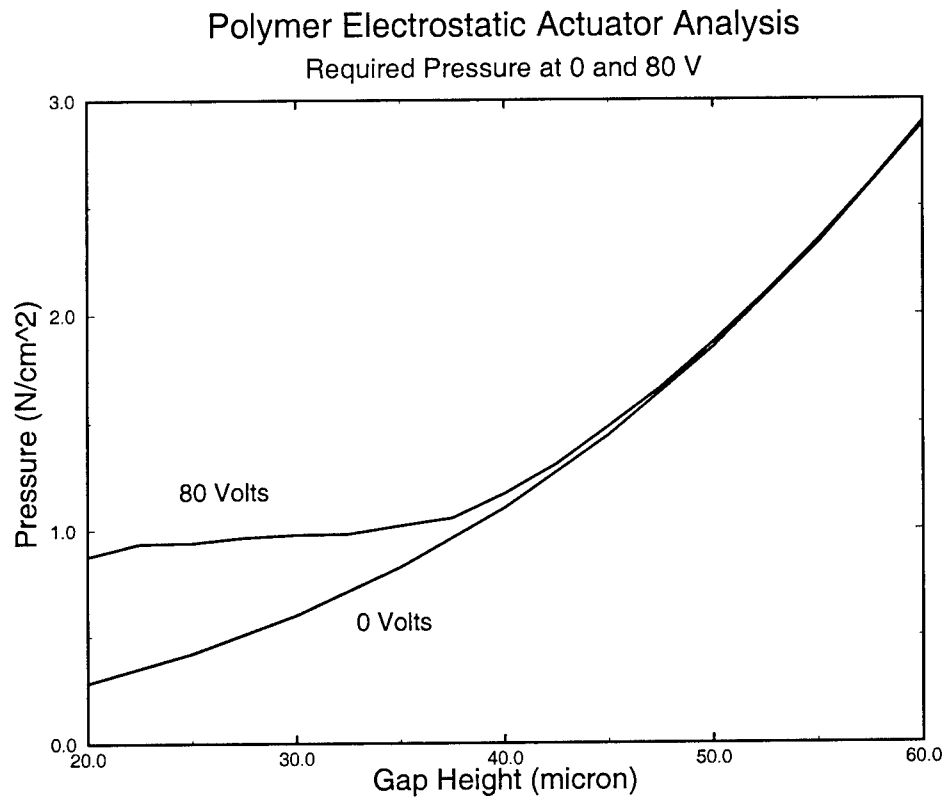


Figure 6-7. Pressure vs. Height Curves for 0 and 80 Volts

7. IMPLICIT COUPLING VIA MULTI-NEWTON METHOD

The linking between physical models such as the electric and the structural models is sequential. Each physical model is solved separately from the others using only boundary conditions and volume conditions the other models calculated during their previous solution. When passing the information between models, linear relaxation may be applied to the relevant parameters to improve convergence. While this linking is efficient for many systems, it will fail when the coupling becomes too stiff. This occurs quite often in solid/fluid systems with small clearances, i.e., elasto-hydrodynamics. Coupled electric/structural systems with small clearances will also demonstrate tight coupling. In these instances, a certain degree of implicit coupling between the models will become necessary to obtain a stable, converged solution. One advanced implicit coupling methodology the "multi-level Newton method" (Aluru and White, 1997) has been implemented to ensure stable and robust convergence. The multi-level Newton method has also been demonstrated for electric/structural coupled problems.

7.1 Multi-Newton Method

The implicit coupling method implemented is the "multi-level Newton method" being developed by Jacob White's research group at MIT (Aluru and White, 1997). The method appears general enough so that it is applicable to any physical model (structures, fluids, heat, electromagnetics) and any solution method (fvm, bem, fem). The technique is a black box approach in that the models to be linked need only have a clear set of input and output values upon which they mutually depend. So, no complicated links need be established between the models.

In the multi-level Newton technique, coupled equations are solved by employing a Newton-Raphson method. The outer Newton iteration solves a "Newton-update linear system" which is a residual equation expressing the difference of the inputs and outputs of the linked models. Each Newton iteration requires the solution of the Newton-update linear system, and this linear system can be solved with a Krylov-subspace algorithm such as GMRES. Each iteration of a Krylov-subspace algorithm requires a matrix vector product which can be approximated using the black box linear solver of each model. Since many of these black box solvers typically employ Newton's method, the approach is referred to as a multi-level Newton method.

For instance, in an electro-mechanical coupling one black box is the structural mechanical model $R_M()$ which inputs an electrostatic force \mathbf{f} and outputs a grid displacement $\mathbf{u} = R_M(\mathbf{f})$. The other black box is an electrostatic model $R_E()$ which inputs a displaced grid \mathbf{u} and outputs an electrostatic force $\mathbf{f} = R_E(\mathbf{u})$. The outer Newton iteration solves a residual equation, that is the "Newton-update linear system", of the form

$$\mathbf{R}(\mathbf{u}, \mathbf{f}) = \begin{Bmatrix} \mathbf{f} - R_E(\mathbf{u}) \\ \mathbf{u} - R_M(\mathbf{f}) \end{Bmatrix} \quad (7.1)$$

The standard Newton technique is applied to Eq. (7.1), in which the residuals are expressed as

$$R(\mathbf{u}, \mathbf{f}) = R(\mathbf{u}^o, \mathbf{f}^o) + \frac{\partial R}{\partial \mathbf{u}} \delta_{\mathbf{u}} + \frac{\partial R}{\partial \mathbf{f}} \delta_{\mathbf{f}} = 0 \quad (7.2)$$

where the 'o' represents the old iteration value.

The Jacobian corresponding to Eq. (7.1) is given by

$$\mathbf{J}(\mathbf{u}, \mathbf{f}) = \begin{Bmatrix} \mathbf{I} & -\frac{\partial R_E}{\partial \mathbf{u}} \\ -\frac{\partial R_M}{\partial \mathbf{f}} & \mathbf{I} \end{Bmatrix} \quad (7.3)$$

which gives the equation

$$\mathbf{J} \begin{Bmatrix} \delta_{\mathbf{f}} \\ \delta_{\mathbf{u}} \end{Bmatrix} = -\{R(\mathbf{u}^o, \mathbf{f}^o)\} \quad (7.4)$$

to be solved at each iteration.

This linear system can be solved using only black-box solvers if Krylov-subspace based iterative methods like GMRES are used. In these methods, the Jacobian is not explicitly needed. Rather, matrix-vector products such as $\mathbf{J} \begin{Bmatrix} \delta_{\mathbf{f}} \\ \delta_{\mathbf{u}} \end{Bmatrix}$ are needed. The approximate form based on the Taylor series is

$$\mathbf{J} \begin{Bmatrix} \delta_{\mathbf{f}} \\ \delta_{\mathbf{u}} \end{Bmatrix} \approx \begin{Bmatrix} \delta_{\mathbf{f}} - \frac{1}{\theta} [R_E(\mathbf{u} + \theta \delta_{\mathbf{u}}) - R_E(\mathbf{u})] \\ \delta_{\mathbf{u}} - \frac{1}{\theta} [R_M(\mathbf{f} + \theta \delta_{\mathbf{f}}) - R_M(\mathbf{f})] \end{Bmatrix} \quad (7.5)$$

where θ is a perturbation parameter.

The multi-level Newton method may be summarized as follows:

1. Start with initial guesses for \mathbf{u} , \mathbf{f} and calculate Residual $R(\mathbf{u}, \mathbf{f})$
2. Solve Eq. (7.4) using a Krylov-subspace iterative method, with the matrix-vector products approximated by Eq. (7.5)
3. Set $\mathbf{u} = \mathbf{u} + \delta_{\mathbf{u}}$; $\mathbf{f} = \mathbf{f} + \delta_{\mathbf{f}}$
4. If $\|\delta_{\mathbf{u}}\| < \epsilon_{\mathbf{u}}$ and $\|\delta_{\mathbf{f}}\| < \epsilon_{\mathbf{f}}$, exit
5. Recalculate new Residual $R(\mathbf{u}, \mathbf{f})$ and return to step 2

7.2 Demonstration of Multi-Newton Method on Electric/Structural Problems

The multi-Newton method was used to implicitly couple the electric and structural models. A comparison was made between the two coupling methods: sequential relaxation and the multi-Newton method. The problem used for comparison is a beam under an electrostatic load and fixed at one end. The beam is 500 μm long, 50 μm wide, and 14.35 μm thick with a Young's modulus of $4.0 \times 10^{10} \text{ N/m}^2$, a Poisson's ratio of 0.3, and no residual stress. A ground plate is placed 1 μm under the beam. The voltage applied to the beam is varied to determine the pull-in voltage. The pull-in voltage is the voltage needed for the beam to be pulled down and just begin to contact the ground plate. As voltages nearer the pull-in voltage are applied, the coupling between the electric and structural models increases.

Shown in Table 7-1 are results of the comparison. At different applied voltages, the iteration and simulation time are compared for the two methods. At an applied voltage of 7.8 V, the Newton algorithm begins to out perform the sequential relaxation algorithm (simulation time is less).

Table 7-1. Comparison of Sequential Relaxation and Multi-Newton Coupling Algorithms

Sequential Relaxation				Newton		
V	DZ	ITER	Time	DZ	ITER	Time
4.0	-6.0032E-08	6	96.85	-6.0135E-08	3	405.94
5.0	-9.9109E-08	8	128.73	-9.9507E-08	3	422.03
6.0	-1.5500E-07	8	126.87	-1.5533E-07	4	578.46
7.0	-2.4265E-07	12	193.16	-2.4299E-07	4	725.35
7.5	-3.1792E-07	20	319.99	-3.1907E-07	5	795.10
7.6	-3.4056E-07	23	367.57	-3.4189E-07	5	781.52
7.8	-4.2788E-07	95	1486.00	-4.3593E-0	8	1291.70

8. IMAGING, VISUALIZATION AND VALIDATION OF MICROSYSTEMS

Sarnoff, in collaboration with the Exxon Corporation, has established an X-ray microtomography/microradiography facility at the Brookhaven National Laboratories. This facility has the capability to characterize 3-D microstructure and 2-D motion inside materials and devices at micron scales. One focus of this project was to develop a communication protocol between Sarnoff's imaging technique and CFDRC's simulation tools. The developed protocol has enabled direct transfer of geometry, mechanical motion, and velocity fields (from measurements) to be read in directly to facilitate one-to-one comparisons between experiments and simulations.

8.1 Imaging and Visualization

Imaging and visualization of microsystems has been carried out at Sarnoff Corporation. The initial investigations focused on the direct examination of the 3-D internal microstructure and microdynamics in fluidic microdevices using x-ray microtomography, visualization methods and an image processing supercomputer (the Princeton Engine).

X-ray Micro-Imaging: For this project, Sarnoff Corporation used the x-ray microtomography facility (owned by Exxon) at the National Synchrotron Light Source (NSLS) at Brookhaven. This facility produces 3-dimensional images of the internal structure of millimeter sized microdevices with resolution approaching 1 micron. The measurement of the 3-D microstructure and visualization of the fluid transport phenomena in microdevices was performed.

Fluid transport through microdevices can be examined using digital subtraction microradiography. This technique produces 2-D projections of the 3-D fluid flow through the channels where the background structure of the specimen has been digitally removed from the image. Liquids such as water are injected into the channels by a syringe pump operating at a constant flow rate ranging from $\mu\text{l}/\text{min}$ to ml/min . A contrasting agent such as chlorine or iodine is added to one of the liquids since at 20keV there is little contrast between the hydrocarbons and water in micron sized paths. The experiment proceeds by taking "pictures" (radiographs) every few seconds (eventually at high speed) until enough frames are collected to visualize the displacement. Typically, over 1000 frames are accumulated. Several frames of the dry specimen are collected, integrated and then subtracted from the radiographs. The results are displayed on a monitor and eventually recorded on videotape.

These flow experiments are coupled with a measurement of the static 3-D microstructure of the microdevice using x-ray microtomography. This technique provides complementary, non-destructive, morphological characterization of the device and the fluids inside.

Supercomputing and Visualization: The large quantity and size of the data sets generated dictate the use of an image processing supercomputer for the automatic analysis and display of information. In particular, Sarnoff Corporation has developed the Princeton Engine (PE), a massively parallel computer. It is designed specifically for real-time image processing and applications requiring extremely high input bandwidth. The PE is used for real-time, interactive volume rendering of the microtomographic volume data sets. Flow characteristics can be better

understood when viewed in the context of the entire three-dimensional microstructure. Techniques for visualizing the structure volumetrically include real-time interactive rotation. For example, a 1283 volume data set can be interactively rotated at a rate of 30 frames/sec. It is only when these data sets are set in motion at sufficiently high frame rates, that the 3-D geometry of the microstructure becomes apparent. In addition, features of interest can be exposed within a volumetric data set by manipulating the opacity and color maps.

8.2 Three-dimensional Geometry Extraction

The 3-D microstructure data and the 2-D motion data are obtained using two types of experiments described above, both of them non-destructive. Microtomography experiments involve the determination of the actual structure of a fabricated MEMS device. Since the field of MEMS fabrication is relatively new, and the dimensions are so small, it is unclear how closely a manufactured device matches the original design specification. In this process, images of a sample are taken at fixed intervals, as the stage upon which the sample sits is rotated. These images are then used as input to a numerical technique called reconstruction, which produces a single 3-D image of the sample with resolution approaching 1 micron. This image can then be used as the input for a computational analysis program to ensure that the actual geometry, rather than an idealization, is used.

Three different methods of geometric extraction were compared. Each method is described briefly below.

Method 1. Isosurfacing via Marching Cubes

Isosurfacing involves the construction of a connected set of polygons at a specified threshold value of the image function. Essentially, we are choosing to connect neighboring voxels whose value equals the threshold value. The threshold value is chosen such that it isolates a single component in the data set. The basic algorithm steps from one end of the data set to the other, "marching" through each voxel. Only information local to the current voxel is used in the surface generation. As a result of this, isosurfacing tends to extract imaging noise and can suffer from the formation of false holes and spurious artifacts. Figure 8-1 illustrates this technique applied to a channel comprised of an asymmetric expansion. Note the apparent roughness of the surface and the presence of small outlier surfaces surrounding the main channel. The surface roughness is not "real", but rather stems from the fact that the marching cubes algorithm fits the surface to the noise in the underlying data

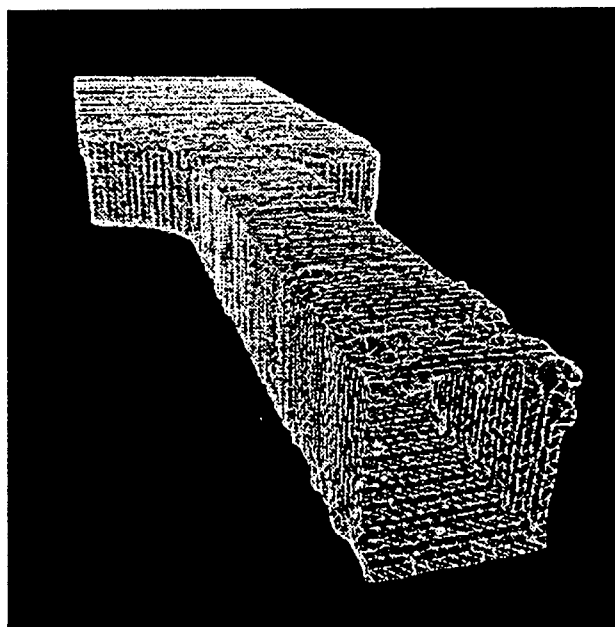
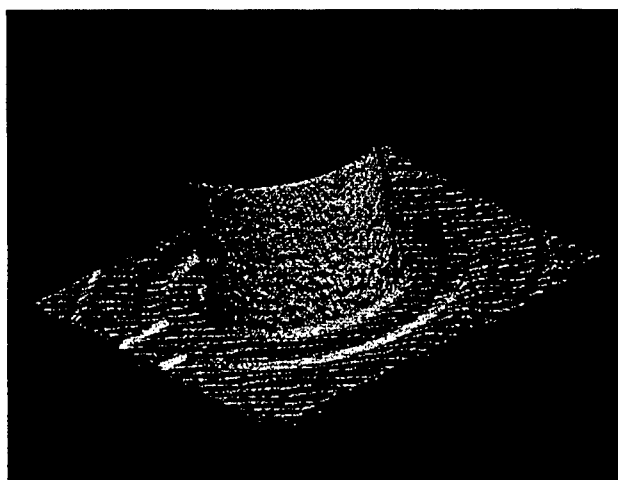
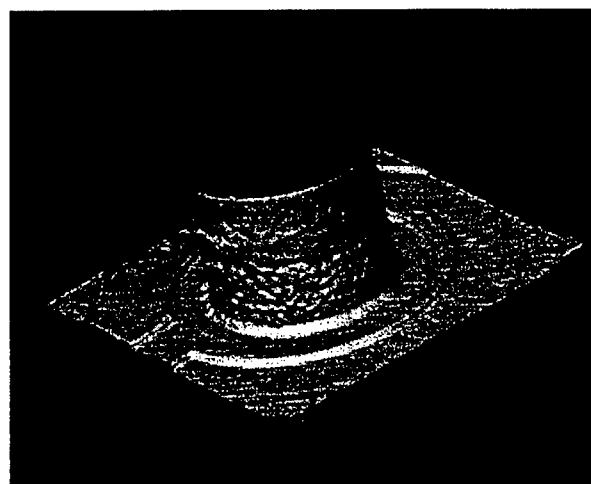


Figure 8-1. Extracted Geometry Algorithm: Isosurfacing via Marching Cubes

An order of magnitude increase in speed can be achieved by applying the Marching Cubes algorithm to only the segmented regions and ignoring all other points. The accuracy of the algorithm was enhanced during the project by modifying the Geometry Extraction algorithm to utilize correctly the original tomographic gray-scale information (rather than arbitrary gray scale values as was done previously) in the vicinity of the segmented object surface. This modification has resulted in reduced artifacts and smoother triangulated surfaces. Figure 8.2 compares the results from the old and new algorithms for the Redwood Microsystems Normally Open Microvalve.



(a)



(b)

Figure 8-2. Comparison of Old and New Marching Cubes Algorithm on the Redwood Systems Normally Open Microvalve

Method 2. Active Contours

In contrast to isosurfacing, active contour algorithms seek to fit piecewise low-order polynomials to feature boundaries (edges) in the image function. Two initial steps are performed: the user specifies initial estimates of the feature boundaries and the input image function is filtered with an edge-enhancing operation. Then, via an iterative process, the initial polynomial estimates are shifted such that the average proximity of the polynomial to the edge features is minimized. If the initial estimates are not separated from the desired features by any local artifacts, the fitted polynomials will appear to “cling” to feature boundaries. This process can be performed on each slice of the volume and the results meshed together. Figure 8-3 shows this technique applied to the channel data set. We have found the active contour approach to work very well for a certain class of imagery, generally characterized by sharply defined edges that form a closed surface. However, in cases where the geometry is complex or the definition between the desired feature and its background is not clear, this method breaks down. Additionally, there is not a great deal of sensitivity to the initial polynomial estimate, making this technique not easily amenable to automation.

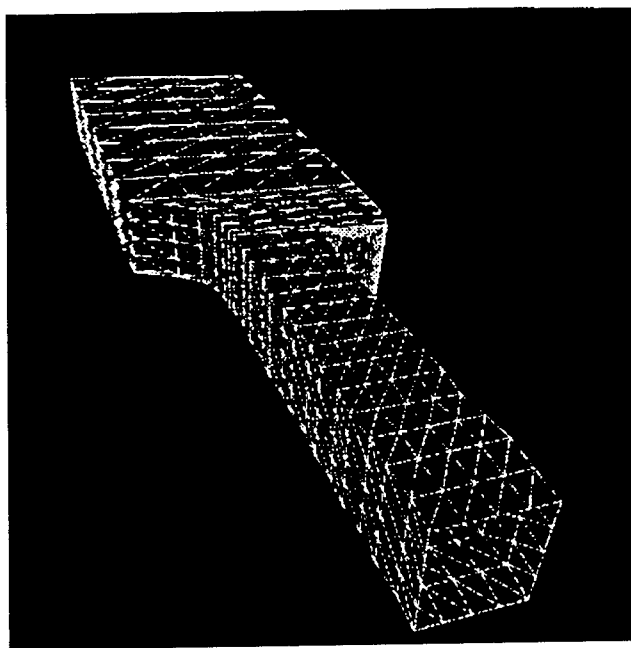


Figure 8-3. Extracted Geometry Using an Active Contours Algorithm

Method 3. Object Segmentation

Object segmentation involves the application of a series of filters to the input volume to produce an intermediate “binary” volume. This intermediate volume represents basic structures in the input in a form in which the effects of imaging noise have been reduced. The intermediate volume can then be fitted with geometrical primitives via isosurfacing. The initial output is well behaved in terms of its sensitivity to noise and requires no initial feature estimates. The filtering operations include an initial thresholding operation to convert the input image into a binary image, followed by a connected component analysis. Here, the idea is to isolate significant features and avoid the outlier problems noted above with pure isosurfacing. After determining the features of interest, several morphological operations are applied which have the effect of

filling holes created by digitization noise and removing thin isthmus' which falsely connect larger features. Finally, a smoothing operation is performed which ameliorates the effects of imaging noise on the overall surface. Figure 8-4 illustrates object segmentation applied to the channel data set. In terms of general usability, we have found the object segmentation technique to be superior to simple isosurfacing and active contours. However, no one single technique works well in all cases and it is useful to have a number of algorithms from which to choose based on the class of imagery to be analyzed.

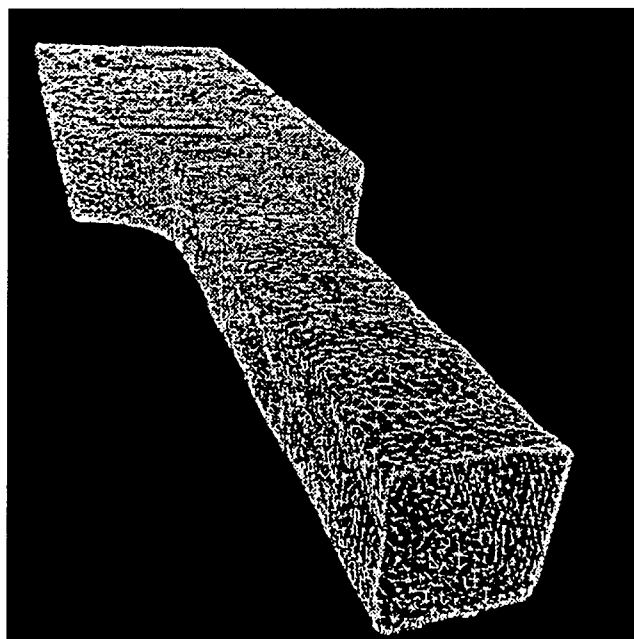


Figure 8-4. Extracted Geometry Using an Object Segmentation Algorithm

Additional Constraints

As explained above, extracting the flow channel surface from tomography data is basically a process of finding a set of polygons which best fit prominent features in the data. However, since this data will be used as the geometry input to a CFD solver, additional constraints must be added to this process. One constraint is that any degenerate triangles must be removed from the data. The other constraint is that the surface set should reflect the natural boundary conditions of the system, e.g. planar inlet and outlet regions. Quite a bit of the work during this project involved imposing these additional constraints on the tomography data so that they could be used by CFDRC's flow solvers. Sarnoff satisfied these constraints by employing a mesh decimator and other filters to the original triangulated surface, until the degenerate triangles were removed and the inlet and outlet surfaces were planar.

Geometric Accuracy

After the geometries were extracted, a method was developed to give a quantitative estimate of the accuracy of the process. The approach here was to create a "ground-truth" data set, for which the exact locations of spatial features are known. Since the physical process (i.e. transmission radiography) employed in the generation of the imagery is known, the effect can be modeled in software and an "ideal" radiograph of some geometry can be calculated. This synthetic data set

can then be employed as the input to the reconstruction algorithm, which converts the sequence of images into a 3-D volume data set. The geometry extraction algorithms are then applied to the synthetic volume and the resulting surface descriptions are compared with those from the initially specified geometry. From this comparison, conclusions can be drawn regarding the effectiveness of the reconstruction and geometry extraction processes. Figure 8-5 shows a channel data set of an original model and the resulting tomography.

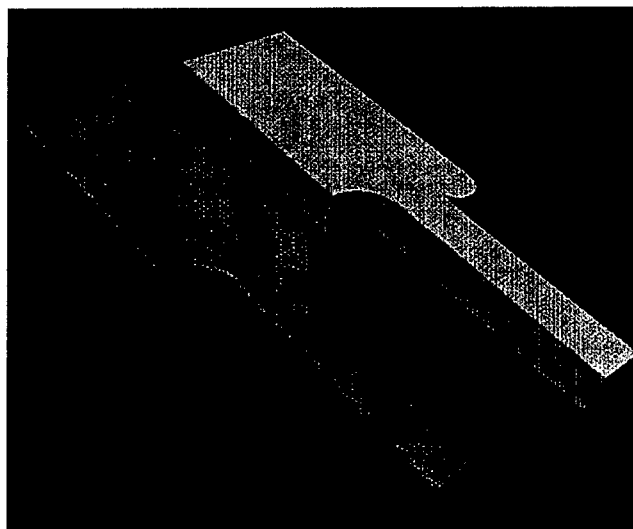


Figure 8-5. Comparison of the Geometry Extracted from the Synthetic Tomography (Blue) versus the Original CAD Model (Yellow). The agreement is very good with the exception of a slight rounding of the edges.

From analysis of these results, the following points are evident:

The corners of the channel walls, which are right angles in the model, are slightly rounded. This rounding is about 5% of the length scale, and is a result of a smoothing operation performed during geometry extraction.

The flat areas of the channel walls are represented as perfectly flat surfaces in the extracted geometry. This is in contrast to slight but consistent roughness seen in real data. We conclude that geometry extraction does not appear to contribute significantly to error in spatially uniform areas.

The areas of gentle curvature are recovered to first order, but not exactly. The deviation is of the same order as that noted for the corner areas, but appears to be more random in nature. This effect may be a result of the representation of smooth curves by discrete polygons in the CAD model. However, this uncertainty is still less than that attributable to imaging noise.

In summary, it appears that the uncertainty generated by the reconstruction and geometry extraction processes are small in relation to the experimental uncertainty of the image acquisition hardware.

8.3 Two-dimensional Flow Field Extraction

In microradiography experiments, the object in question is stationary and X-ray images are taken at fixed temporal intervals until enough frames are collected to visualize some dynamic process (e.g. actuation of a flap valve, fluid motion, etc.). In studying fluid flow, a neutrally buoyant emulsion is used to track fluid motion. The recovery of the flow field from these images is a non-trivial matter because of local ambiguities in the apparent displacement of image intensities and the effects of noise. Sarnoff constrains the flow recovery process by making use of physical and geometric constraints derived from fluid mechanics.

Currently, three constraints are imposed on the flow recovery process. The first constraint enforces local rigidity of the recovered flow (i.e. infinitesimal material particles only translate and rotate). The second constraint enforces local smoothness of the recovered flow (effectively constraining the velocity change from point to point). This constraint is particularly important in minimizing the effects of image noise. The third constraint is related to boundary conditions on the recovered flow. Specifically, the flow must stay in its channel and the velocity must go to zero at the channel surface.

Variational calculus is used, along with the three constraints mentioned above, to yield partial differential equations which relate image density to the flow field. Solution of the resulting equations results in a 2-D flow field, representing the averaged flow across the height of the device. These equations are solved numerically on a grid that can be composed of arbitrary collections of polygons to approximate complex device geometries.

8.4 Comparison of Measured and Calculated Flow Data

The image data from Sarnoff is provided as a triangulated surface in STL (StereoLithography) format. This data then provides the geometric input to the flow solver. The triangulated surface can either be used as the surface grid for the CFD mesh, or may be used to define the surface geometry onto which a separate grid is imposed. In the early stages of this project, the CFDRC geometry and grid generation software was not able to use STL files as a surface geometry definition, and thus we attempted to use the STL files as a triangulated surface mesh from which a volume mesh was derived. This process was successful, but the results obtained from the flow solver were not satisfactory. The surface grid obtained from Sarnoff used triangles which were all nearly the same size. This is a good approach for geometry specification, but it is a poor method for constructing a surface mesh, since there is not a finer grid in regions of the domain where large flow parameter gradients may occur. The result of this method was a grid which had a fairly large number of grid cells, but was not fine enough in certain regions to capture important flow details. Basically, we were asking more of the tomography reduction procedure than it was intended for. As a result, for the remainder of the cases we constructed the grid from the sketches provided by Sarnoff.

Figure 8-6 shows four flow channels for which image data was provided to CFDRC from Sarnoff. These flow channels each were 200 micron high, and were etched in a silicon substrate and covered with glass. The tomography images for these geometries are shown in Figure 8-7. The computational grids used in for the CFD runs are given in Figure 8-8. These grids were

created "from scratch" starting with the sketches shown in Figure 8-6, not from the STL files shown in Figure 8-7.

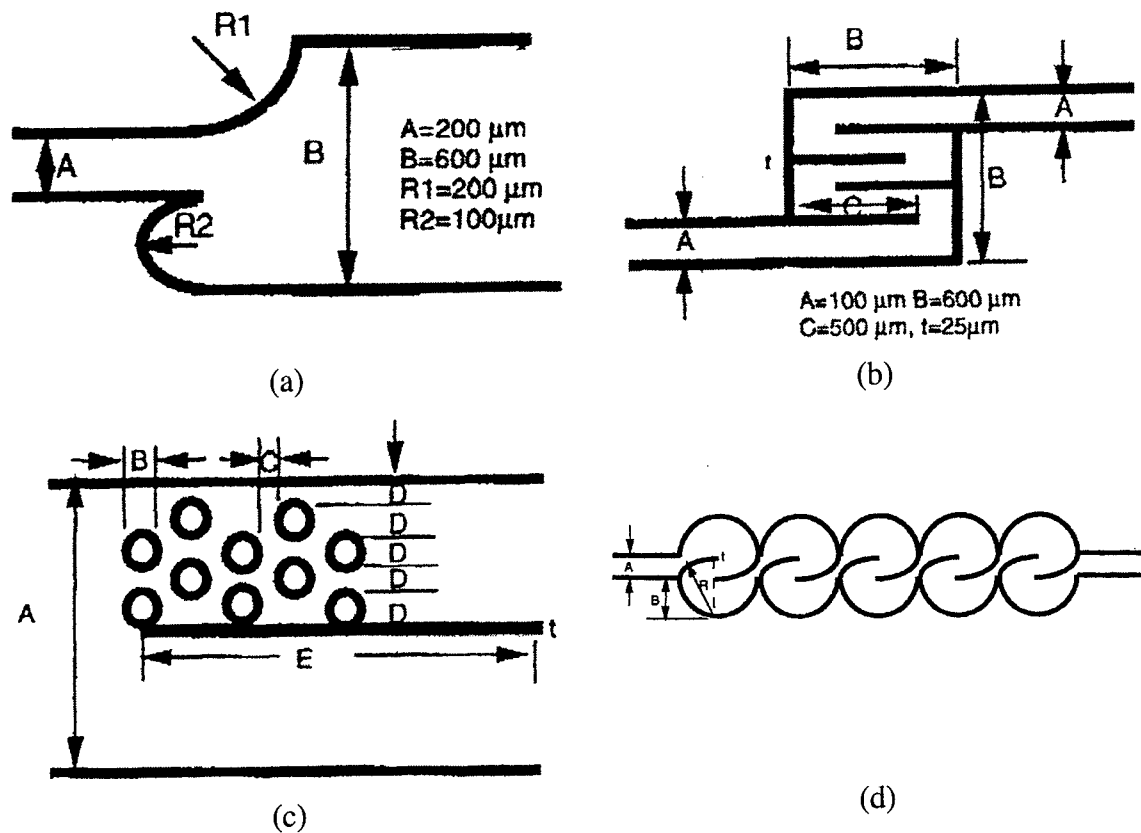
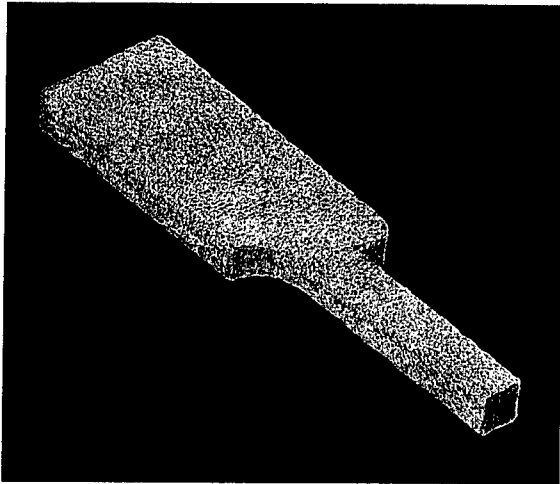


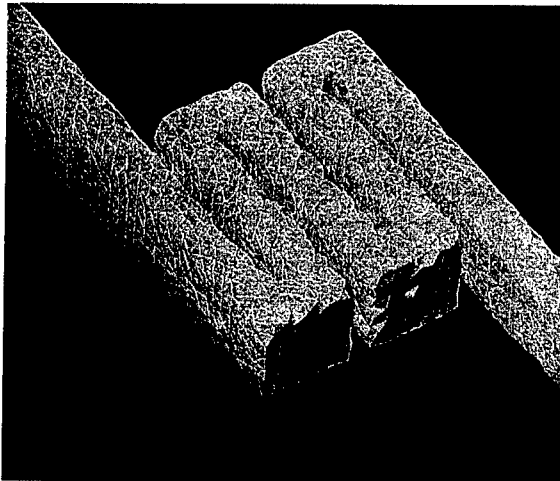
Figure 8-6. Schematics of the Flow Channels Received from Sarnoff



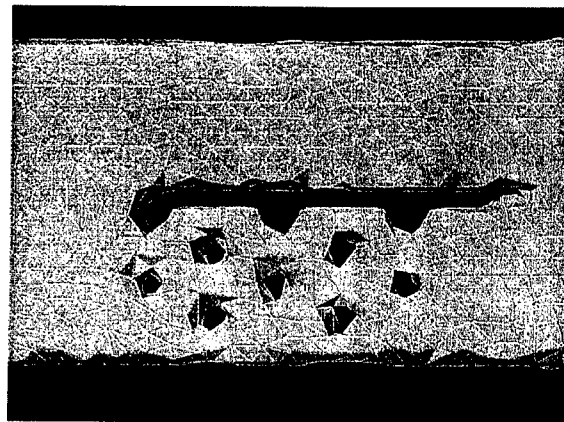
(a)



(b)



(c)



(d)

Figure 8-7. Visualization of the STL Files of the Flow Channels Received from Sarnoff

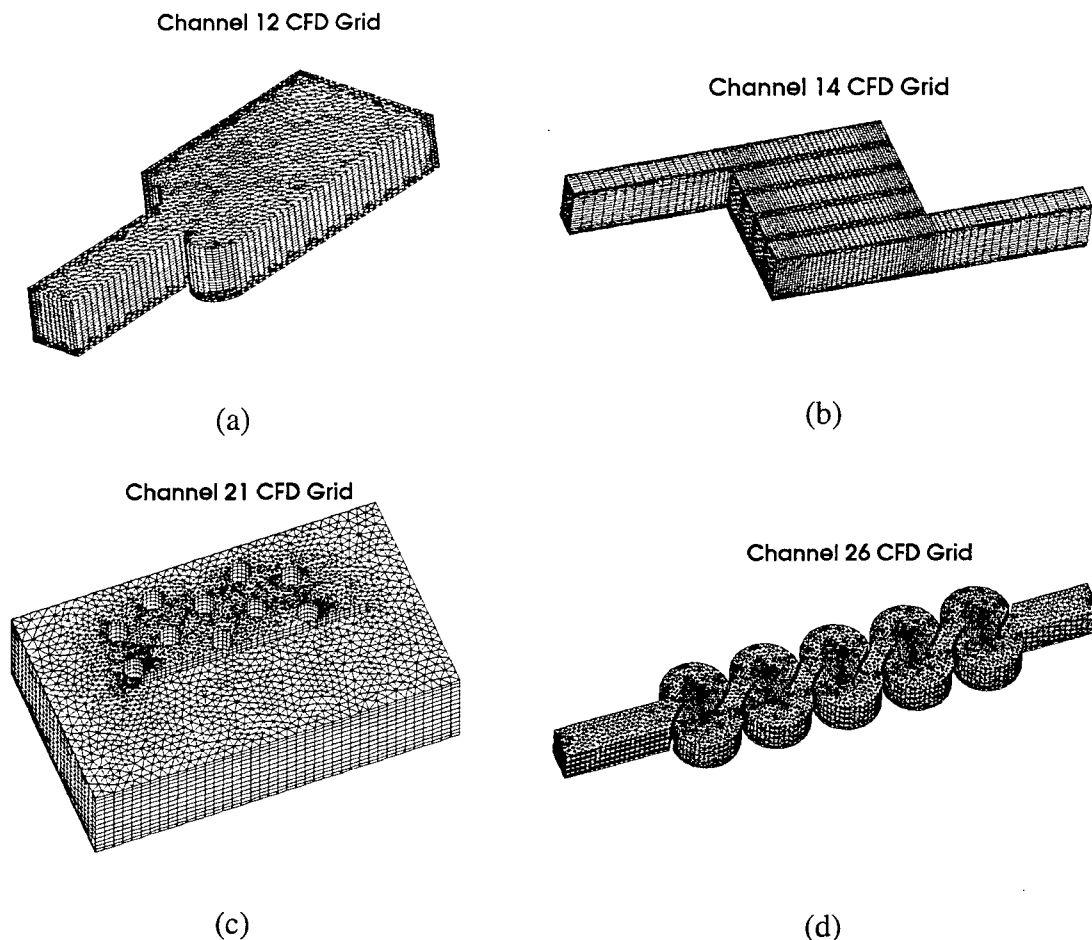


Figure 8-8. Computational Grids for the Channel Geometries

After the CFD solution, the 3-D flow fields must be averaged across the channel height for comparison with the Sarnoff experimental data. A special post-processing program was written to perform this task. In addition, another program was developed to convert the flow data provided by Sarnoff into a format which could be read by CFDRC's post-processing graphics program, CFD-VIEW. Figure 8-9 through Figure 8-11 shows the comparison of the averaged flow fields from the Sarnoff experiments and the CFDRC simulations for three of the channels. Flow data was not available for channel 26 so Figure 8-12 shows only the CFD predicted velocity and stresses. For each case, velocity vectors are shown colored with the magnitude of the predominant velocity component. As seen, the comparison is very good, both qualitatively and quantitatively.

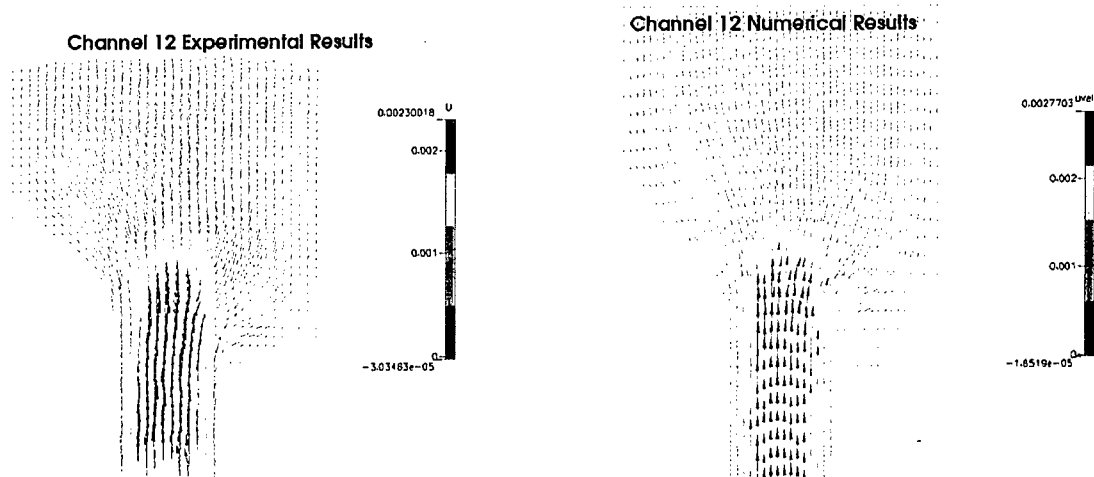


Figure 8-9. Numerical and Experimental Velocity Fields for Channel 12

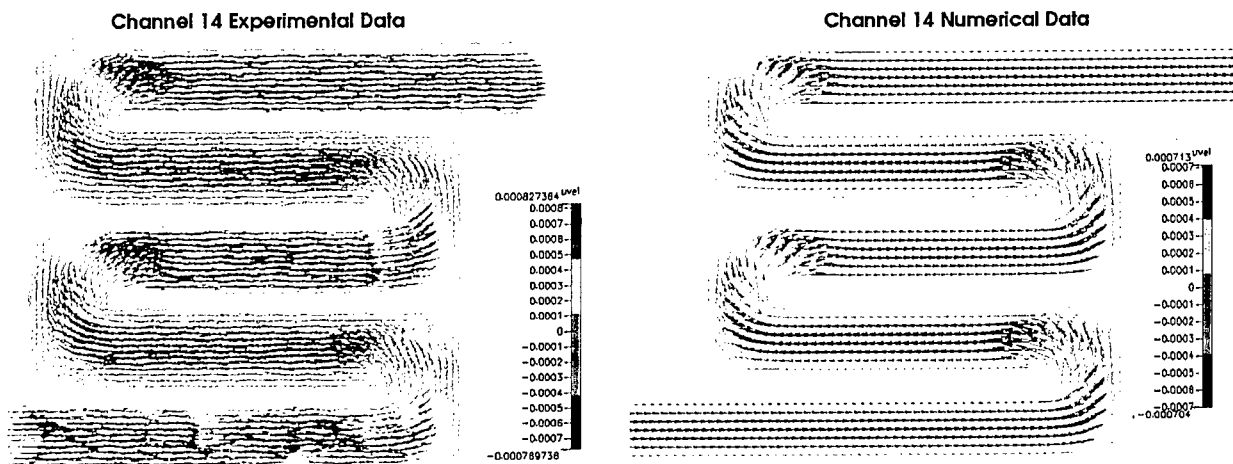


Figure 8-10. Numerical and Experimental Velocity Fields for Channel 14

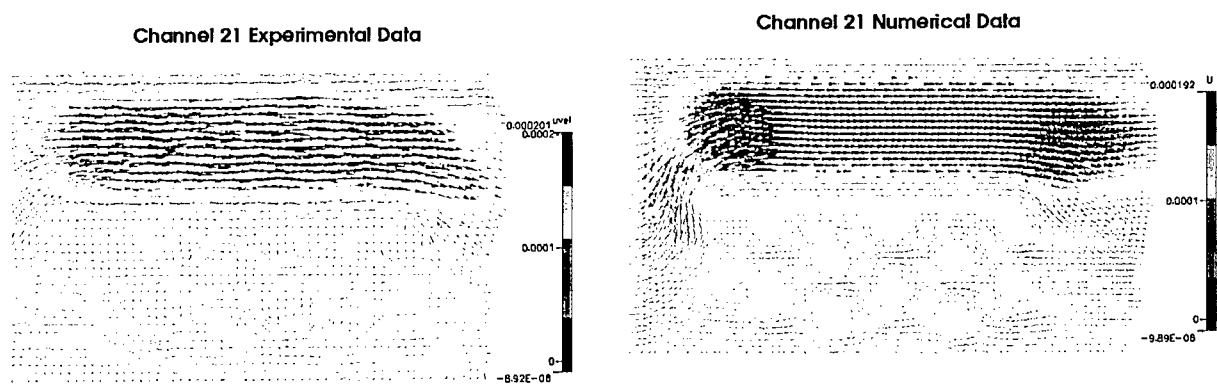


Figure 8-11. Numerical and Experimental Velocity Fields for Channel 21

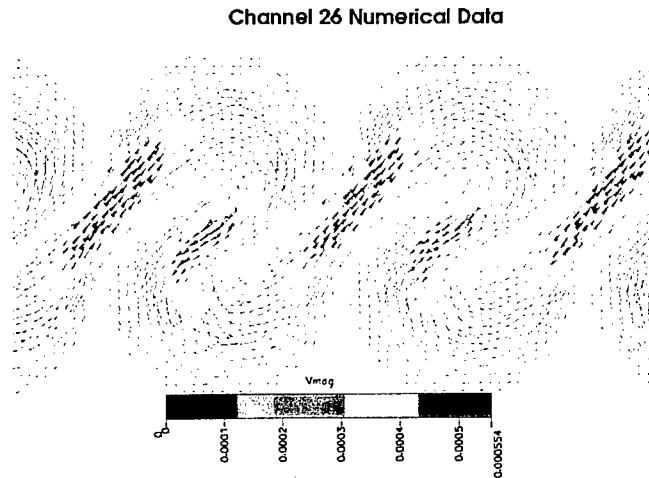


Figure 8-12. Predicted Velocity Field for Channel 26

During the course of this project, work was progressing on a different project within CFDRC for the development of an automatic grid generation program for external flow aerodynamics. After the initial development work, the program capabilities were extended to accommodate internal flows. The program developed from this work, CFD-CARTESIAN, can create adaptive Cartesian meshes from surface triangulations in various formats, including STL format. It uses an omni-tree data structure to support anisotropic grid adaptation, and also has the ability to create viscous sublayers for resolution of boundary layers.

To demonstrate the use of this program, Channels 12 and 14 were gridded with CFD-CARTESIAN. These grids are shown in Figure 8-13. For channel 14, the mesh was used in a flow simulation using CFD-ACE+. Figure 8-14 shows the flow results at the center plane (these results were not averaged across the thickness because the post processing program which does this does not accommodate adaptive Cartesian meshes). The predicted maximum velocity is 1.4 times the average velocity shown in Figure 8-10 (compared to the theoretical value of 1.5). These results compare favorably considering the difference in grid density between the two runs.

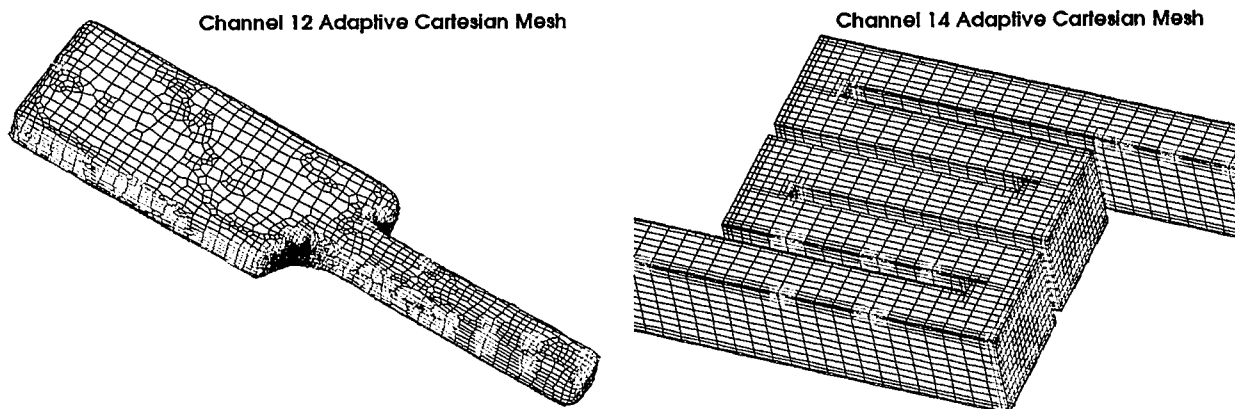


Figure 8-13. CFD-CARTESIAN Calculated Conversion of STL Format Files into Computational Grids for Channel 12 and 14

Channel 14 – Adaptive Cartesian Mesh

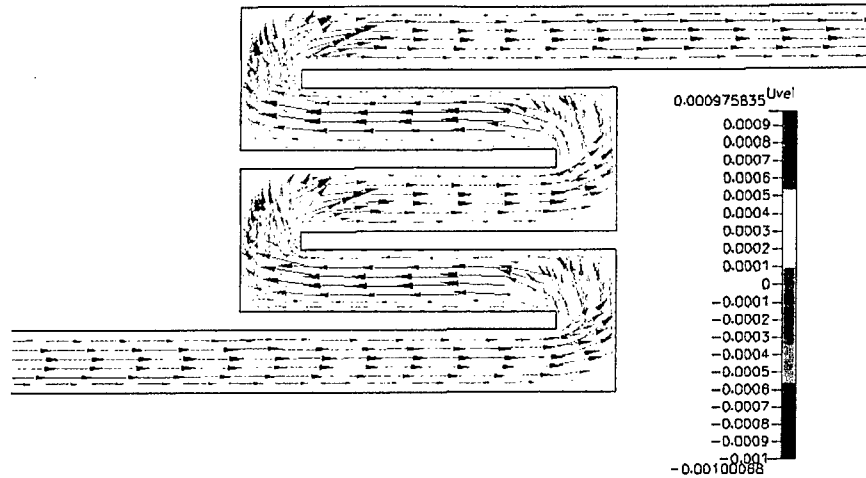


Figure 8-14. Resulting CFD Calculation on Channel 14 Using the Computational Grid Generated by CFD-CARTESIAN from the STL Formatted File

8.5 Comparison of Measured and Calculated Electrostatic Deformation

A search was made to find a sufficiently experimentally characterized electrostatically actuated device for which the developed CFD-ACE+MEMS software could be validated. Ideally, the experimental characterization would contain: (i) measurement of the fabricated device geometry; (ii) a specification of the idealized geometry of the device such as specified by a fabrication definition file such as the “CIF” format; (iii) the electronic drive and sensing circuitry the device was operated in during testing and visualization; and (iv) measurements of the motion of the device such as obtained by analysis of experimental imagery.

The data Sarnoff can supply includes: (i) images of devices in operation at eight intervals along the sinusoidal drive voltage for different drive frequencies; (ii) (x,y,t) motion data for the eight intervals as extracted from the 2-D images; (iii) CIF format files of the manufacturing specification of the device; (iv) input/output signal plot over a range of frequencies to determine Q; and (v) the z component of motion data (in addition to x,y) at resonance although guessed at by analyzing 2-D images.

Two such data sets of previously visualized devices were considered for this validation task. One was a linear lateral resonator comb drive with the imaged field of view of the device shown in Figure 8-15(a) and the other was an angular comb drive (manufactured by Exponent Failure Analysis Corporation) whose imaged field of view is shown in Figure 8-15(b).

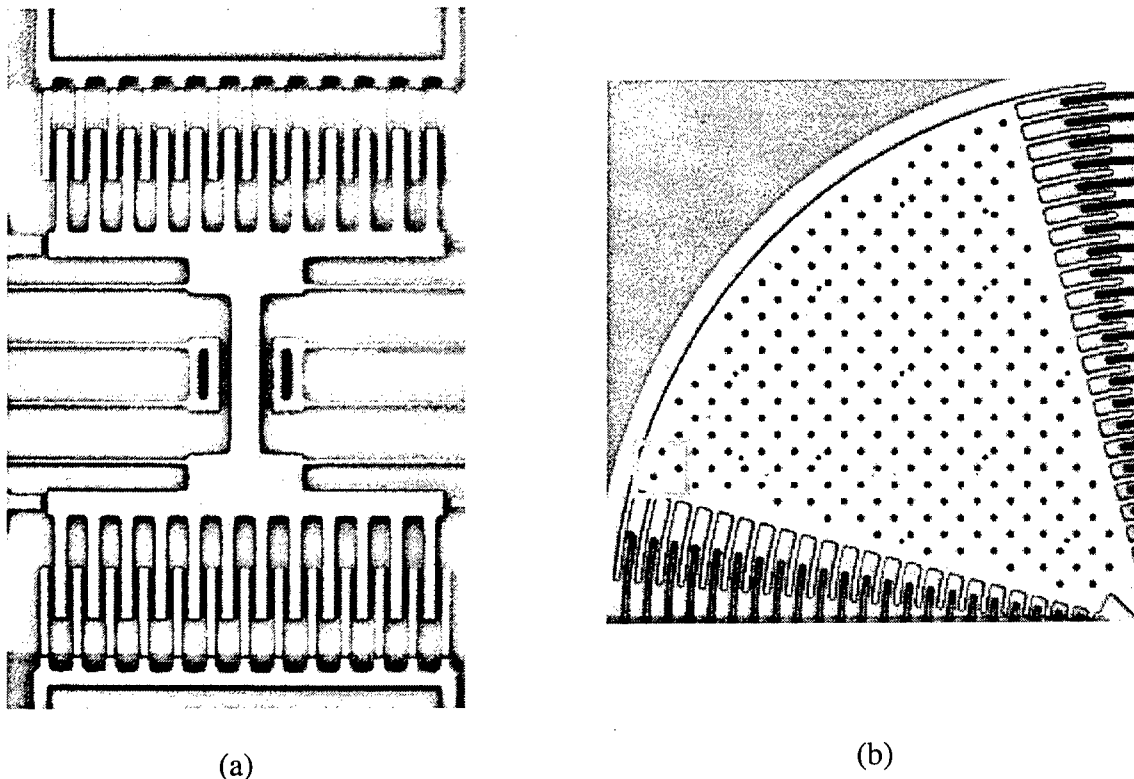


Figure 8-15. Representative Visualization Images of Two Electrostatically Actuated Comb Drives. (a) Linear Lateral Resonator Comb Drive and (b) Angular Comb Drive

There was not enough imaging information on the linear lateral resonator comb drive (Figure 8-15(a)) to simulate the device. The imaged region of the device has clipped off the folded beams on either side of the comb structures. The length of these folded beams is an essential parameter which controls the resonant states of the device. The “CIF” file, which establishes the processing specification used to manufacture the device, was unavailable so even an idealized geometry of this device was unattainable.

The other device under consideration is an angular comb drive (Figure 8-15(b)). Again the imaged data clips off some essential geometric features of the device. One is the length of the beam in the lower right-hand side of the image which is a deforming beam whose length will have a large impact on device operation. Another piece of geometry missing is the length of the fingers of the comb drive toward the rotational center of the device. The “CIF” file of this device is available however (Figure 8-16) so that an idealized geometry of the device can be generated for the numerical simulation.

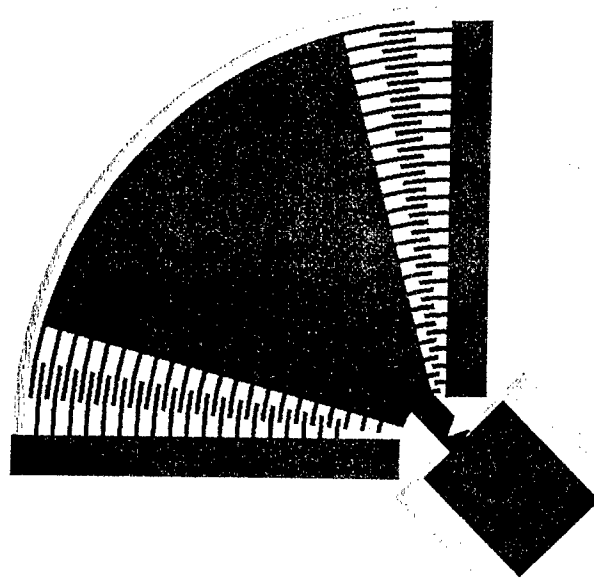


Figure 8-16. Visualization of CIF File Specifying MUMPS (Multi-User MEMS Processes) Manufacturing Process for Construction of Angular Resonator

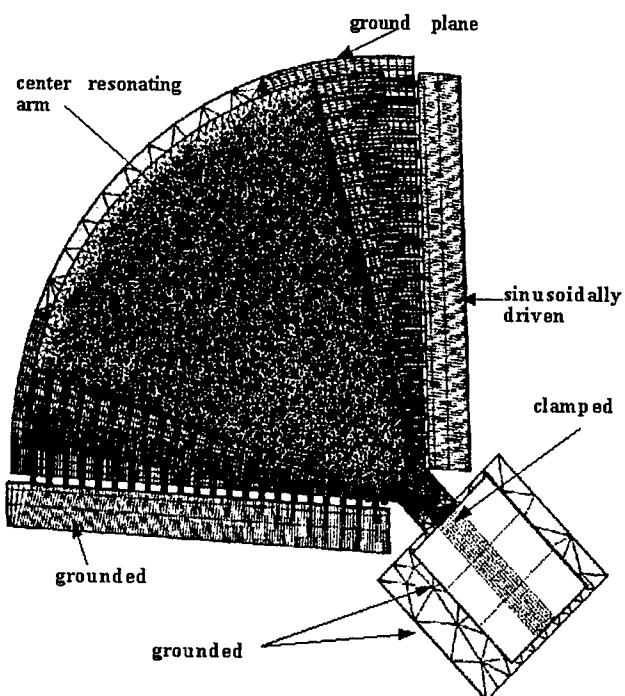


Figure 8-17. Angular Resonator Grid Used for Simulation

The grid for the angular resonator (Figure 8-17) was generated by reading in the CIF formatted file into CFD-GEOM. GEOM converted the file into lines and points. All grid specifications had to be done by hand. A structured grid was used near the interlaced comb fingers for which BEM is more accurate. An unstructured grid was used for the center resonating arm. Prisms were used for the unstructured volume mesh.

A sinusoidal voltage $V_m \sin(2\pi f t + \phi)$ with $V_m = 35.15$ V, $f = 20387.9$ Hz, and $\phi = 0$ was applied to the fixed comb on the right in Figure 8-17. All other structures were grounded. In the structural model the faces of the center resonating arm connected to the contact pad were given a fixed displacement. The structural mechanics model was solved only on the center resonating arm volume grid (13315 prisms). The electric BEM model was solved only for the structured portion of the ground plane under the right fixed comb and the fingers and connecting faces of the fixed comb (7941 square faces).

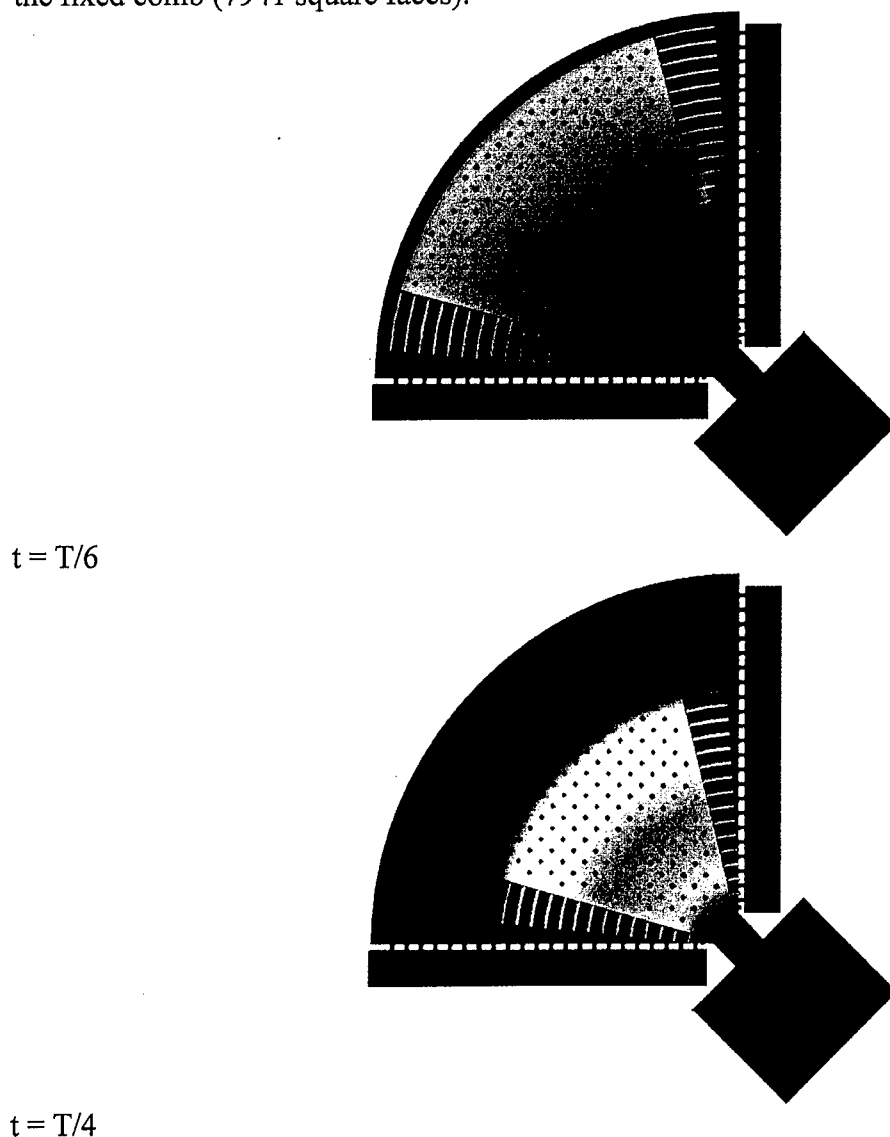


Figure 8-18. Calculated Deformation of the Angular Resonator at Two Different Times. Color Contours are Displacement Magnitudes.

Shown in Figure 8-18 is the calculated deformation of the angular resonator at two different times. The color contours are displacement magnitudes with a peak of $5.5\text{ }\mu\text{m}$ occurring at time $T/4$ where T is the period ($1/f$).

The calculated data cannot be reliably compared to the measured data from Sarnoff. The actual Young's Modulus of the fabricated device is not known. The actual geometry of the manufactured device was not gridded, only the idealized geometry from an electronic file was used. Also, if any detecting voltage was applied to the left comb, it would effect the displacement of the drive. The presence or absence of the detecting voltage on the left fixed comb is not known.

The experimentally measured displacement is calculated by interpolating changes in the imaged device. The experimental determined displacement of the point in the center of the red box in Figure 8-15(b) is in peak-to-peak values: $\Delta x = 666\text{ nm}$ peak-to-peak, $\Delta y = 2090\text{ nm}$ peak-to-peak, and $\Delta z = 55\text{ nm}$ peak-to-peak. The calculated values using the CAD tool are: $\Delta x = 1621\text{ nm}$, $\Delta y = 4955\text{ nm}$, and $\Delta z = 1\text{ nm}$. The agreement between these numbers is not very good but could be attributes to many things as noted above.

9. CONCLUSIONS AND PLANS FOR FUTURE WORK

This chapter presents the conclusions from the current project and the plans for future extensions and applications of the models.

9.1 Summary of Accomplishments

The completion of this project has resulted in the first-ever integration of fluidic, thermal, chemical, electromagnetic and mechanical models within a single software environment, CFD-ACE+MEMS. In addition to the physical models, CFD-ACE+MEMS has geometry/grid generation modules, scientific data visualization module and a fluid/material properties database. Depending on the problem being solved, the user has the option to either have a loose coupling between the physical models or a tight, implicit coupling (necessary for highly stiff systems). All of the software modules have been developed by CFDRC and will be marketed and supported by CFDRC.

In addition to development, the models and the coupling between the modules were tested and verified on several simple as well as complex device systems. The FVM and BEM models for electrostatics were benchmarked for different applications. This project has also produced a communication protocol between Sarnoff's unique microtomography technology (for visualizing device microstructure, motion and velocity fields) and CFDRC's simulation software. This protocol enables the generation of geometry and computational grid directly from the imaged data and facilitates one-to-one comparison between measured and computed device behavior. The agreement between model and measurements was evaluated for several microfluidic devices as well as an electrostatic rotary comb drive.

The papers published resulting from this effort are Stout et al., 1999; Athavale et al, 1999; and Krishnan A., 1999.

Finally, CFDRC established working relationships with several MEMS device manufacturers (during this project) to demonstrate the simulation tools for design of industrial devices. These collaborations are summarized below.

9.2 Industrial Collaborations and Software License

This project has enabled CFDRC to perform several recent modeling studies for MEMS companies using the coupled electrostatic capability. These are summarized below:

- **Micropump for Honeywell:** CFDRC performed 3-D simulations of coupled fluid-structural-electrostatic phenomena in a micropump currently being prototyped by Honeywell. These simulations were successful in highlighting some of the complexities of the interaction between the above phenomena and enabled Honeywell designers to improve the performance of the micropump.
- **Electrostatically Activated Beam for Honeywell:** Simulations were performed for Honeywell to analyze the deflection of a cantilever beam for different actuation voltages.

Non-linear effects were also simulated. Mechanical forces (as a function of gap height) for different voltages were computed.

- **Microvalve for Xerox:** CFDRC performed simulations of coupled fluid-structural-electrostatic interactions in Xerox's microvalve. The simulations clearly showed the highly non-linear nature of the valve operation and also gave insights as to the extent of voltage drop necessary for optimal performance of the valve.
- **Electrophoresis Applications:** CFDRC is currently working with Oak Ridge National Lab., Caliper Technologies, Aclara Biosciences, etc. to demonstrate CFDRC's electrophoresis model that accounts for interactions between charged species transport and the applied electrostatic field.

Several organizations such as Redwood Microsystems, Lucas Novasensor, YSI, Motorola, Oak Ridge National Laboratory, BioDOT, Stanford University, University of California (Berkeley), University of Washington, etc. are currently using CFD-ACE+MEMS for microsystem applications. Additionally, several microelectronics companies such as Wacker-Siltronic, Aixtron, Motorola, Applied Materials and Novellus have purchased software licenses from CFDRC for coupled fluid-thermal-structural-electromagnetic simulations. Their applications include electromagnetic induction heating, Lorentz force stabilization of melt flow in crystal growth, low-pressure plasma transport and electroplating. CFDRC expects a large market for this coupled simulation capability. CFDRC's software is one-of-a-kind in its ability to closely integrate these models.

9.3 Future Work

This project has laid the foundation for CFDRC to extend its capabilities to (i) the development of reduced/parametric models, and (ii) simulation of systems of microdevices using the reduced models. Two key projects (currently ongoing at CFDRC) that will build upon this foundation are as follows :

- DARPA BAA 97-17: "Generation of Reduced Parametric Models of Microdevices from High Fidelity Tools for System Level Composite CAD" focuses on building a high-fidelity simulation environment for generating reduced models for MEMS devices and systems. This tool will perform mixed-dimensionality simulations (i.e., simultaneously simulate a system of a micro-channel and a micro-mixer using a 0-D model for the channel and a 2-D model for the mixer). Mixed-dimensionality simulations will be performed to determine dynamic responses of devices which will then be used to derive reduced order 'lumped-parameter' models.
- DARPA BAA 97-39: "Mixed-Dimensionality VLSI-Type Configurable Simulation Tools for Virtual Prototyping of Biomicrofluidic Devices and Integrated Systems" focuses on the development of a SPICE-like environment to link primitive MEMS elements to form a system-level model for coupled fluid-thermal-chemical-electrical-magnetic-structural phenomena in microsystems. This project will validate these models on microfluidic systems for complex chemical and biological applications.

CFDRC will continue to actively commercialize the CFD-ACE+MEMS software to the MEMS community. This software will be demonstrated at all leading MEMS conferences, workshops

and trade-shows. CFDRC will provide academic licenses (at a highly discounted price) to universities, research laboratories and non-profit organizations to facilitate widespread use of the software. Additionally, CFDRC will also provide hands-on training, documentation, technical support and upgrades for the effective use of the software (by the industry) as a design tool.

10. REFERENCES

- Aluru, N. and White, J., "A Multi-level Newton Method for Static and Fundamental Frequency Analysis of Electromechanical Systems," Intl. Conf. On Simulation of Semiconductor Processes and Devices (SISPAD), Boston, MA, pp. 125-128 (1997).
- Athavale, M., Li, H.Y., Yang, H.Q., Przekwas, A.J., Cabuz, C., Herb, W., and Arch, D., "Coupled Electrostatics-Structures-Fluidic Simulations of a Bead Mesopump", International Mechanical Engineering Congress and Exposition (IMECE), Nashville, TN, November (1999).
- Arkilic, E. B., Breuer, K. S. and Schmidt, M. A., "Gaseous Flow in Microchannels," ASME FED vol. 197, pp. 57-66, Nov. 1994.
- Barba, P. D., Savini, A., and Wiak, S., "3-D Computer-Aided Analysis of an Electrostatic Micromotor," Int.Conf. Electrical Machines, Proc. vol. 2 pp. 111-115 (1994).
- Bird, R. B., Stewart, W. E., and Lightfoot, E. N., *Transport Phenomena*, J. Wiley & Sons, New York (1960).
- Buser, R. A. and de Rooij, N. F., "CAD for Silicon Anisotropic Etching," in Proc. IEEE Microelectromechanical Systems, pp. 111-112, Napa Valley, CA, Feb. 1990.
- Cefai, J. J., Barrow, D. A., Woias, P., and Muller, E., "Integrated Chemical Analysis of Microsystems in Space Life Sciences Research," J. Micromech. Microeng., pp. 172, 1994.
- Fiveland, W.A., "Discrete-Ordinates Solutions of the Radiative Transport Equation for Rectangular Enclosures," J. of Heat Transfer **106**, pp. 699-706 (1984).
- Fuhr, G., and Shirley, S. G., "Cell Handling and Characterization Using Micron and Submicron Electrode Arrays: State-of-the-Art and Perspectives of Semiconductor Microtools," J. Micromech. Microeng., pp. 77, 1995.
- Gebhard, U., Hein, H. and Schmidt, U., "Numerical Investigation of Fluidic Micro-oscillators," J. Micromech. and Microeng., pp. 115-117, 1996.
- Gravesen, P., Branebjerg, J. and Jensen, O.S., "Microfluidics - A Review," J. Micromech. Microeng., pp. 168, 1993.
- Hirt, C. and Nichols, B., "Volume of Fluid (VOF) method for the dynamics of free boundaries", J. Comp. Phys. **39**, pp. 201-225 (1981).
- Judy, J. W. and Muller, R. S., "Magnetically actuated, addressable microstructures", J. Microelectromechanical Systems **6**(3) pp. 249-256 (1997).
- Koppelman, G. M., "OYSTER, a Three-dimensional Structural Simulator for Microelectromechanical Design," Sensors and Actuators, vol. 20, pp. 179-185, Nov. 1989.
- Krishnan, A., "Development of Multi-Disciplinary Simulation Tools for Electrochemical Systems", invited paper to Meeting of the Electrochemical Society, Seattle, WA (1999).
- Lai, J., Shi, Z., Perazzo, T., and Majumdar A., "Optimization and Performance of High-Resolution Micro-optomechanical Thermal Sensors," Sensors and Actuators **58**, pp. 113-119 (1997).

- Lee, K. W. and Wise, K. D., "SENSIM: A Simulation Program for Solid-State Pressure Sensors," IEEE Trans. Electron Devices, ED-29, pp. 34-41, 1982.
- Mehregany, M., "Micromechanical Systems," IEEE Circuits and Devices, July, 1993.
- Patankar, S. V., *Numerical Heat Transfer and Fluid Flow*, Hemisphere Publishing Corporation, New York (1980).
- Pfahler, J., Harley, J. and Bau, H., "Liquid Transport in Micron and Submicron Channels," Sensors and Actuators, A21-A23, pp. 431-434, 1990.
- Pilkey, W. D. and Wunderlich, W., *Mechanics of Structures: Variational and Computational Methods*, CRC Press, Ann Arbor (1994).
- Poppe, A., Rencz, M., Szekely, V., Karam, J. M., Courtois, B., Hofmann, K. and Glesner, M., "CAD Framework Concept for the Design of Integrated Microsystems," SPIE, vol. 2642, pp. 215-224, 1995.
- Przekwas, A. J., "A Visual Computing Environment (VCE) for Multi-Disciplinary Multi-Scale Distributed Simulations of Microelectromechanical Systems," Invited presentation at 12th UACEM Symposium, Worcester, July 1995.
- Puers, B., Petersen, E. and Sansen, W., "CAD Tools in Mechanical Sensor Design (CAPSIM)," Sensors and Actuators, 17, 1989.
- Rapoport, S. D., Reed, M. L., and Weiss, L. F., "Fabrication and Testing of a Microdynamic Rotor for Blood Flow Measurements," J. Micromech. Microeng., pp. 60, 1991.
- Rohsenow, W. M. and Choi H., *Heat Mass and Momentum Transfer*, Prentice-Hall, Englewood Cliffs, N.J. (1961).
- Sandmaier, H., Offereins, H. L. and Folkmer, B., "CAD Tools for Micromechanics," J. Micromech and Microeng., pp. 103-106, 1993.
- Senturia, S. D., Harris, R. M., Johnson, B. P., Kim, S., Nabors, K., Shulman, M. A., and White, J. K., "A Computer-Aided Design System for Microelectromechanical Systems (MEMCAD)," J. Microelectromechanical Systems, Vol. 1, No. 1, pp. 3-13, March 1992.
- Stewart, J. T., "Finite Element Modeling of Microelectromechanical Structures for Sensing Applications," SPIE, vol. 2642, pp. 194-205, 1995.
- Stout, P. J., Yang, H. Q., Dionne, P., Leonard, A., Tan, Z., Przekwas, A., Krishnan, A., "CFD-ACE+MEMS: A CAD system for simulation and modeling of MEMS"; Design, Test, and Micofabrication of MEMS/MOEMS; Paris, France; SPIE Vol. 3680 (1999).
- Tang, W. C., Lim, M. G., and Howe, R. T., "Electrostatic comb drive levitation and control method", J. Microelectromechanical Systems 1(4) pp. 170-178 (1992).
- Urbanek, W., Zemel, J. N. and Bau, H. H., "An Investigation of the Temperature Dependence of Poiseuille Numbers in Microchannel Flow," J. Micromech. and Microeng., pp. 206-209, 1993.
- Vollmer, J., Hein, H., Menz, W. and Walter, F., "Bistable Fluidic Elements in LIGA Techniques for Flow Control in Fluidic Microactuators," Sensors and Actuators A (43) pp 330-334, 1994.
- Yang, H. Q. and Przekwas, A. J., "Computational modeling of microfluidic devices with free surface liquid handling", International conference on Modeling and Simulation of Microsystems, semiconductors, sensors, and actuators, MSM-98, Santa Clara, CA pp. 498-505 (1998).
- Zengerle, R. and Richter, M., "Simulation of Microfluid Systems," J. Micromech. Microeng., pp. 192, 1994.

Zhang, Y., Crary, S. B. and Wise, K. D., "Pressure Sensor Design and Simulation Using the CAEMEMS-D Module," in Tech. Dig. IEEE Solid-State Sensor and Actuator Workshop, pp. 32-35, Hilton Head, SC, June 1990.

CLARE D. THIEM
AFRL/IFTC
26 ELECTRONIC PKWY
ROME NY 13441-4514

15

ATTENTION: DR PHILLIP STOUT
CFD RESEARCH CORP
215 WYNN DR 5TH FLOOR
HUNTSVILLE AL 35805

2

AFRL/IFOIL
TECHNICAL LIBRARY
26 ELECTRONIC PKY
ROME NY 13441-4514

1

2

ATTENTION: DTIC-OCC
DEFENSE TECHNICAL INFO CENTER
8725 JOHN J. KINGMAN ROAD, STE 0944
FT. BELVOIR, VA 22060-6218

1

4

ATTENTION: DR ANANTHA KRISHMAN
DARPA/MTO
3701 N FAIRFAX DRIVE
ARLINGTON VA 22203

5

125

*Total Number of Copies is:

25

I have verified that this address list is correct and complete.
also checked the mailing labels to see that they are correct and
for use.

Clare D. Thiem

Signature

***MISSION
OF
AFRL/INFORMATION DIRECTORATE (IF)***

The advancement and application of information systems science and technology for aerospace command and control and its transition to air, space, and ground systems to meet customer needs in the areas of Global Awareness, Dynamic Planning and Execution, and Global Information Exchange is the focus of this AFRL organization. The directorate's areas of investigation include a broad spectrum of information and fusion, communication, collaborative environment and modeling and simulation, defensive information warfare, and intelligent information systems technologies.